Design, Construction and Biophysical Applications of Optical Tweezers

Eirini Theofanidou

Doctor of Philosophy

The University of Edinburgh

2004

To my late father

Acknowledgments

This thesis would have not been possible without the help, guidance and support of many people. I would like to sincerely thank:

My supervisors Dr. Will J. Hossack and Prof. Wilson C.K. Poon, not only for their expert guidance, but also for their unceasing help and encouragement.

Dr. Jason Crain for his continuous advice and support.

Dr. Jochen Arlt for his assistance and advice. Dr. T.J. Su for establishing the DNA preparation technique, for her guidance in the biochemistry lab, Mr Natsuhiko Yoshinaga for useful talks on the DNA condensation and Dr. David Dryden for allowing me to work in his lab.

Dr. Gareth Valentine and Dr. David Burns from the Institute of Photonics, University of Strathclyde for supplying the DMM high voltage interface, for useful discussions and their help with adapting the software to the experimental system. Dr. Kevin Heggarty for creating and adapting the software used in the holographic tweezers setup.

Andy Garrie for valuable technical assistance. Steven Duffield for his computing support. Dr. Andy Schofield for help in the chemistry lab.

Laurence Wilson, Trevor Whittley, Steven Magennis, Andrew Lafong and all people in physics and in the chemistry lab for providing a pleasant working environment.

My husband Vasileios, my mother Anastasia, my sister Giota for their love and patience. My two best friends Eleni and Stefania for invaluable support. Many thanks also to Eudokia, Ioannis, Maria, Gery, Nikos, Stella, Spyros, Melina, Lampis, Donika and Petros.

The Greek football national team for providing unforgettable moments during Euro2004.

This thesis is dedicated to my late dad who has provided care, love and inspiration throughout my life.

Ιθάκη

ITHACA

Σα βγεις στον πηγαιμό για την Ιθάκη,
να εύχεσαι νάναι μακρύς ο δρόμος,
γεμάτος περιπέτειες, γεμάτος γνώσεις.
Τους Λαιστρυγόνας και τους Κύκλωπας,
τον θυμωμένο Ποσειδώνα μη φοβάσαι,
τέτοια στον δρόμο σου ποτέ σου δεν θα βρεις,
αν μεν' η σκέψις σου υψηλή, αν εκλεκτή συγκίνησις
το πνεύμα και το σώμα σου αγγίζει.
Τους Λαιστρυγόνας και τους Κύκλωπας,
τον άγριο Ποσειδώνα δεν θα συναντήσεις,
αν δεν τους κουβανείς μες στην ψυχή σου,
αν η ψυχή σου δεν τους στήνει εμπρός σου.

Να εύχεσαι νάναι μακρύς ο δρόμος.
Πολλά τα καλοκαιρινά πρωϊνά να είναι
που με τι ευχαρίστησι, με τι χαρά
θα μπαίνεις σε λιμένας πρωτοειδωμένους
να σταματήσεις σ' εμπορεία Φοινικικά,
και τες καλές πραγμάτειες ν' αποκτήσεις,
σεντέφια και κοράλλια, κεχριμπάρια κ' έβενους,
και ηδονικά μυρωδικά κάθε λογής,
όσο μπορείς πιο άφθονα ηδονικά μυρωδικά.

Κ.ΚΑΒΑΦΗΣ

K. Kavafis

Abstract

Today there is great interest in micro/nanomanipulation tools for both physical and biomedical applications. Since the first demonstration of optical trapping in 1986, optical tweezers have proven to be one of the leading manipulation techniques for microscopic colloidal particles. Furthermore, the combination of optical tweezers with single molecule fluorescent imaging provides the necessary combination for the study of single biopolymers such as DNA. In optical tweezers radiation pressure from a laser beam is used to trap, control and manipulate dielectric objects, in a size range from nm to μm.

The first part of the work focuses on biophysical applications. A commercial microscope combined with fluorescence imaging was used to analyse the stretching and unwinding of DNA, as well as DNA condensation. Deformation of polymers under flow is important for understanding the rheological properties of dilute polymer solutions. I studied the DNA shape at different velocities using optical trapping of single DNA molecules tethered on polystyrene beads. The results showed clearly the two theoretically predicted regimes of "trumpet" and "stem and flower". Furthermore, they suggest that the hydrodynamic interactions depend on the flow velocity. In addition, the kinetics of hydrodynamically-stretched DNA condensation induced by spermidine was investigated. DNA collapse is essential to the functioning of viruses, bacteria and eukaryotic cells. An unexpected period of latency during which the DNA remained stretched in the presence of the condensing agent was observed. This latency time extended from a few seconds to over 20 seconds. The results indicate that the spermidine binding is strongly affected by the flow induced straightening of the DNA.

The second part of this work is dedicated to technical issues and system developments. An optical tweezers set-up based on a home-built microscope was used in combination with two photon fluorescence to investigate the deterioration of the quality of the trap due to optical aberrations. It was shown that using adaptive optics (i.e. a deformable membrane), the aberrations were partially corrected. Furthermore, it was demonstrated that using the deformable membrane one can achieve the axial-position control of the trapped particle over a limited range. A home-built optical microscope was also used in combination with a ferroelectric liquid crystal spatial light modulator to construct multiple trap tweezers. The fast switching speed of the ferroelectric device, compared to

a conventional nematic system, enabled very rapid reconfiguration of trap geometries, controlled, high speed particle movement, and the first tweezers array multiplexing.

Contents

Chapter 1

Introduction

This thesis is concerned with the use of optical traps, or laser tweezers, in the manipulation of single molecules, and in the further development of the trapping technique itself. In this chapter, a brief introduction of the history of optical tweezers, their applications in current research and an outline of this thesis are presented.

Optical tweezers is an instrument using a tightly focused laser beam to capture and manipulate microscopic objects in three dimensions. The trapping is achieved without any mechanical contact and without causing any overt damage. The size of trapped species ranges from a few nanometres up to a few micrometers.

The physics of optical traps is based on radiation pressure, that is the forces exerted due to the change of light momentum when the light interacts with matter. Arthur Ashkin was the first to demonstrate in 1970 the ability of an unfocused laser beam to attract micron-sized particles with high refractive index into the beam axis and accelerate them in the direction of the beam propagation. At the same time he used two counter-propagating beams to create an "optical bottle"; thus dielectric particles were trapped in three dimensions [1]. In a later experiment, radiation pressure was used to levitate small particles and liquid droplets [2].

Optical tweezers were developed for first time in 1986 by Ashkin in his publication "Observation of a single beam gradient force optical trap for dielectric particles" [3]. A microscope objective with high numerical aperture was used to focus a beam of intense radiation from a laser in order to create a stable trapping zone.

The optical trapping forces generated are in the region of few piconewtons when milliwatts of laser power are used. These forces are tiny for the macroscopic world but strong enough to trap and manipulate microscopic particles. Two colloidal particles attracting each other with a potential whose contact value is $\sim 10\ k_{\mathrm{B}}T$ and which decays over $\sim$ 10 nm can be separated by a force of a few pN. A force equal to 10 pN is enough to stretch or bend biomolecules like DNA or RNA, while 20 pN can break most protein-protein interactions. Thus, a variety of physical and biological applications are possible, and the technique is rapidly becoming common-place in many laboratories. The only caveat, particularly relevant for biological application, is laser damage: laser power can cause damage to the live organisms, a phenomenon called opticution. In order to avoid that effect the trapping laser has to be carefully selected. For biological samples the appropriate choice has proven to be lasers with wavelengths in the near IR region (1064 nm) were light absorption is low. Thus, the absorption of light and the associated damage are minimised.

The first experiment, done by Ashkin and Driedzic in 1987, was the trapping of bacteria and tobacco mosaic virus [4]. The same year they trapped and manipulated cells [5] and in a later development they trapped cell organelles and measured the force of their movement inside living cells [6]. Other groups used tweezers for single molecule studies: Block *et al.* have explored the movement of single kinesin molecules inside microtubules [7]; while Kuo *et al.* stretched kinesin [8] and measured the associated forces [9]. The mechanics of myosin was also studied [10, 11]. Optical trapping was applied to stretch DNA and study its dynamic properties [12], to unzip DNA [13] or to investigate DNA interactions with different enzymes and proteins [14]. Furthermore, the forces exerted by single molecular motors were measured [15, 16].

Numerous more applications on polymer physics [17], mechanical properties of membranes [18], cell manipulation [19], colloids science [20, 21, 22] and pharmacology [23] have used the advantages of the technique.

While the basic technique of optical tweezers must be considered well developed, numerous technical innovations continue to add to their versatility. One important area of development concerns how optical trapping is combined with imaging. In the "standard" set-up, imaging is performed simply in the bright-field mode. But it is now possible to perform optical trapping also with fluorescence imaging, phase contrast [24, 25], confocal scanning microscopy [26] and other optical techniques, for example interferometry [27], Raman spectroscopy [28], single molecule fluorescence spectroscopy in order to obtain high resolution information on position or conformation [29]. Optical tweezers have also been used as optical scissors [30] when combined with another laser, and as optical spanners for rotation of particles [31]. Trapping ability was also expanded to capture metallic particles [32, 33] and other objects with higher refractive index than the surrounding medium [34]. Many parametric studies for calculating the trapping efficiency have been done both on theoretical and experimental level [35, 36, 37].

In this thesis, I report the use of optical tweezers for the study of single molecules of DNA in flow fields (Part 1, Chapters 3, 4 and 5), and the development of the trapping technique itself (Part 2, Chapters 6 and 7). The rest of this work is organised as follows:

In **Chapter 2** we introduce the basic concepts of optical microscopy and the physical principles of optical trapping; the design of a basic optical tweezer set-up is then described.

In **Chapter 3** we explain the importance of combining single molecule fluorescence imaging with optical tweezers in order to perform single DNA molecule studies. A brief description of DNA and the sample preparation procedures is given.

In **Chapter 4** a systematic experimental study of DNA deformation under uniform

flow is presented; the effect of flow on DNA shape is discussed within the framework of scaling theory.

In **Chapter 5** the nucleation kinetics of DNA condensation under uniform flow is investigated, including its dependence on flow speed, the condensing agent binding, the introduction of salt and the DNA length.

In **Chapter 6** the effect of spherical aberrations on the stability and strength of the optical trap is described and an attempt to reduce aberrations by using a deformable membrane mirror is presented.

In **Chapter 7** a ferroelectric liquid crystal display is used to create an array of 4×4 optical traps, to achieve high translation speeds of 1 μm polystyrene beads and to perform multiplex trapping.

Chapter 2

The Physics of Microscopy and Optical Tweezers

2.1 Introduction

A typical optical tweezers setup consists of a microscope combined with a series of external lenses and mirrors, and a laser source. In this chapter, the basic concepts of microscopy are examined with more details on the parts of the microscope which play a key-role for the creation of an optical trap. Subsequently, the background theory of optical tweezers is explained and a description of how to built a setup is given.

2.2 Microscopy

2.2.1 The Compound Microscope

In everyday life the most common single lens met is the human eye. When an observer wants to see the details of an object, he can bring it closer to his eye in order to

achieve higher magnification [38]. The magnification ability of the human eye though, is limited; when the object comes closer than the eye's *near point* the image becomes blurred. In that case, a *simple magnifying glass* or *a simple microscope* can be used to increase the magnification [38, 39]. Figure 2.1 shows the image formed by a single lens with focal length f.

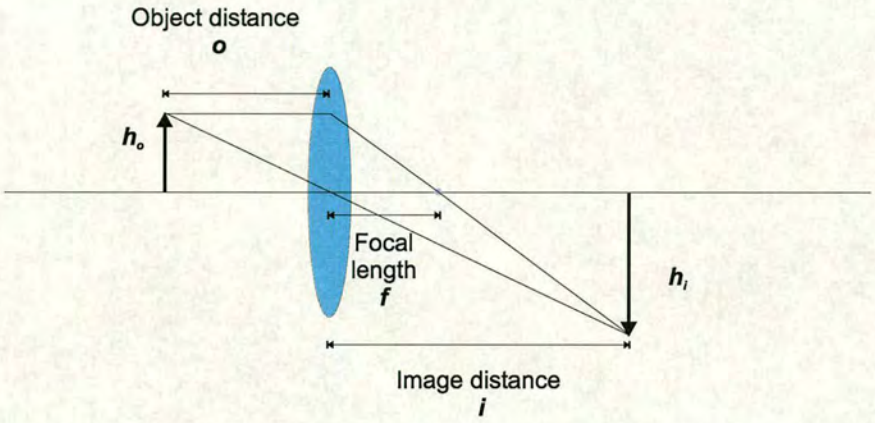

Figure 2.1: Image magnification from a single lens with focal length f.

The lateral magnification is defined as [39, 40]

$$M = \frac{h_i}{h_o}, \tag{2.1}$$

where h_o, h_i are the size of the object and the image, respectively.

However, when objects in the micron scale are examined in order to be able to provide high magnification and visualise their fine details without compromising the image quality a *compound microscope* is needed [41]. The first compound microscope dates back hundreds of years; it is an instrument where more than one lens is used. The basic optical components used in a microscope are:

- the illuminator, which consists of the light source and the collector lens,
- the condenser lens,

- the microscope objective lens and
- the ocular or eyepiece.

Figure 2.2a gives the schematic diagram of a single microscope. Initially the specimen is magnified by an objective lens forming a real image at the intermediate image plane which is further magnified by the eyepiece giving a final magnified virtual image [39, 42]. This image is perceived either by the observer's eye or a camera. All the above have to be on the same axis; the whole configuration is called the *optical train* of a microscope. Furthermore, additional components, for example apertures which control the illumination, filters which modify the contrast, or extra components for applications other that brightfield microscopy are usually inserted in the optical train of todays microscopes.

Each of the optical components mentioned above consists of one or more lenses and plays a different role in the illumination or image formation of the specimen. A description of these operations follows with additional details for those components which determine also the performance of a tweezers system.

The illuminator consists of the light source which is usually a tungsten-halogen lamp of 50 or 100 W and the collector lens which collects the light rays emerging from the lamp filament and images them onto the condenser aperture placed at the front focal plane of the condenser. The field diaphragm acts as a virtual source of light: it controls only the width of the light rays reaching the condenser and it does not affect the angle or the numerical aperture (NA) of the illumination.

The condenser condenses, i.e. refocuses, the light onto the specimen and controls the aperture of the illumination through its aperture. Its adjustment is the most critical step in achieving uniform illumination of the specimen.

The microscope objective is the most important lens in a microscope; it is this one that images the specimen by collecting the light emerging from it and forms an intermediate

image inside the microscope tube. The distance between the back focal plane of the objective and the intermediate image plane is called optical tube length and may be different from the mechanical tube length, which is defined as the distance between the mount of the objective and the eye's lens point (see Figure 2.2) [42]. The mechanical tube length used to be fixed (but different for different manufacturers) until recently, when the infinity corrected microscopes were introduced [42, 43].

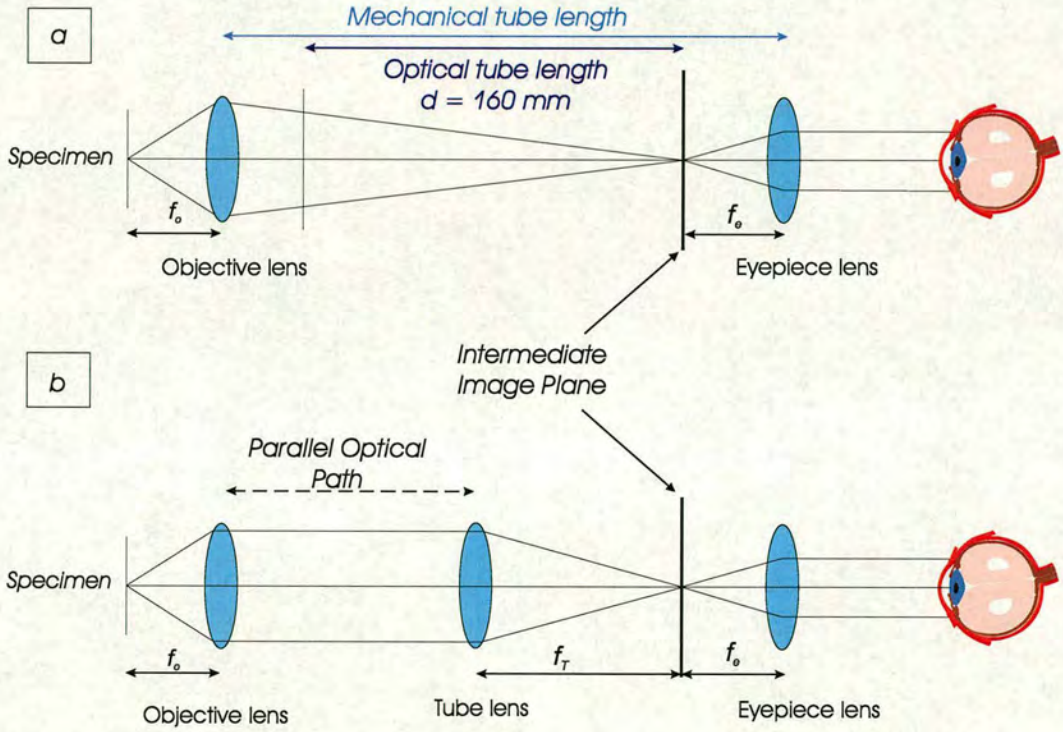

Figure 2.2: Basic components of a microscope; a) the optical path of the image formation rays with a microscope objective and b) the optical path with an infinity corrected microscope objective. The focal length of the objective is f_o, the eyepiece f_e and the tube lens f_T.

Infinity corrected objectives are designed in such a way that they form the intermediate image plane at infinity, with the rays emerging from the exit pupil of the lens being parallel rather than converging; thus a lens has to be inserted to allow the formation of the image in the tube. This lens is called the *tube lens* and its focal length varies for dif-

ferent manufacturers. Infinity corrected microscopy enables extra optical components, for example beam-splitters or filters, to be added in the optical tube without increasing the degree of aberrations. For a finite tube length microscope these components would shift the intermediate image introducing aberrations, in particular spherical aberration and field curvature. Moreover, the microscope has become more flexible since now the objective can move independently from the eyepiece. Figure 2.2 gives the optical path for the two different types of microscopes.

It is the properties of the objective being used which mainly determine the quality of the final image, its magnification and its resolution. The different specifications for a microscope objective are: the magnification, the degree of corrections for optical aberrations and the curvature of the field of view, the working distance, the medium used between the objective and the cover glass of the specimen and finally the numerical aperture (NA).

The working distance (WD), is defined as the distance between the coverslip and the front lens of the objective, while the parfocal distance (PFD), is the one between the object plane and the mount of the objective. Objectives with different power have obviously different WD but they can have the same PFD which make them exchangeable without causing any damage to the specimen and without any change of focus.

The numerical aperture of the objective is defined as:

$$NA = n \sin \theta \ , \tag{2.2}$$

where n is the refractive index of the medium used and θ is half the angle of the angular aperture A of the light cone, Figure 2.3.

The eyepiece examines the real inverted magnified image formed by the objective at the intermediate image plane which is at the position of the fixed diaphragm of the eyepiece. The same can be done by a camera with capturing images or even movies of the specimen.

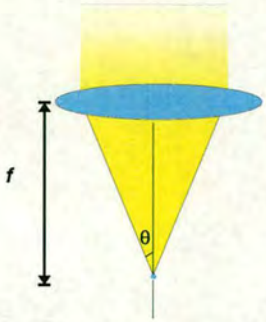

Figure 2.3: Numerical Aperture of a lens: the control of the light cone emerging.

2.2.2 Image Quality

The parameters characterising an image are:

- The total magnification of the compound microscope is given as the product of the magnifications achieved by the objective and the eyepiece, or the camera. Although more powerful objectives provide higher magnification it has to be mentioned that sometimes extremely high magnification is meaningless if it is not accompanied by good resolution; such magnification which gives no more details of an object is called *empty magnification* [39]. The useful range of magnifying power depends on the NA of the objective and it is between 500× and 1000× NA when observed by the eye.

- The resolution of the microscope - and any imaging system - is defined as the minimum distance between two points at which they are distinctly separate. The aperture of an imaging system governs the brightness of the image formed but it also introduces diffraction effects. Even for a aberration-free system the rays converge with each other around the focus and they yield in a three dimensional diffraction pattern symmetrically located about the microscope axis [40]. Thus any well corrected system is said to be diffraction-limited. This 3-D pattern is called the Point-Spread-Function (PSF) and when projected on the focal-image

plane it gives a 2-D pattern called the Airy disk [38, 43] as seen in Figure 2.4.

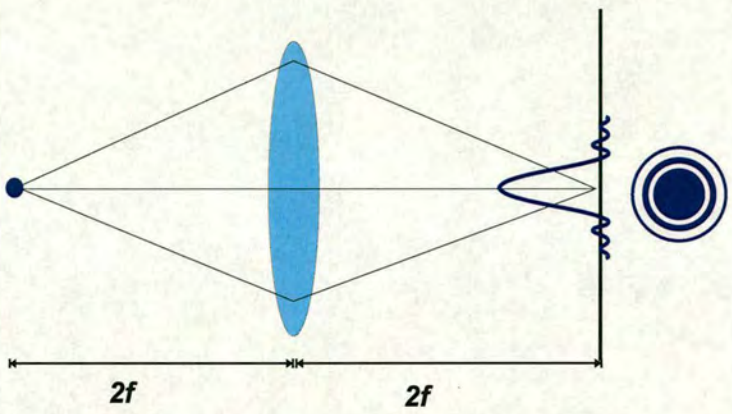

Figure 2.4: The intensity distribution in the diffraction pattern and the Airy disk by a single lens.

Thus, when an objective lens focuses on a specimen, each point of it is represented by an airy-disk rather than a single point. If the airy disks from two adjacent points come too close then the amount of overlapping becomes too much and it is not possible to distinguish between the two points, Figure 2.5.

There is quite an arbitrary check to determine whether two points are individually discernible and that is the *Rayleigh criterion*: two points are just resolvable when the centre of the Airy disk of one falls on the first minimum of the second. This means that the angular separation (ϕ) between the two points from the objective lens of the system has to be [41]:

$$\phi = \frac{1.22\lambda}{\alpha}\,, \tag{2.3}$$

where λ is the wavelength of the illumination light and α is the diameter of the lens. This corresponds to

$$R = \frac{0.61\lambda}{NA}\,, \tag{2.4}$$

where R is the minimum distance between two points and NA the numerical aperture of the objective.

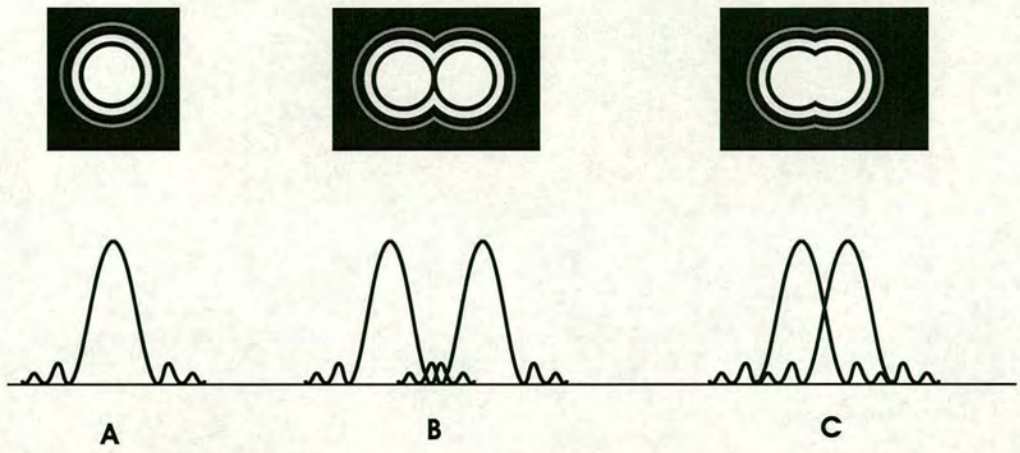

Figure 2.5: The resolution criterion: A) Schematic diagram of the diffraction pattern and Airy disk for a point source of light. B) and C) The diffraction patterns and Airy disks from two neighboring light sources separated by different distances: in B the centre to centre distance between the Airy disks is larger than their radii and the two disks can be distinguishable where as in C the distance is less than the radius and the two peaks are not resolved.

- The contrast and the brightness of the image are also important. The contrast of the image depends on the grey level difference that is provided in an image. Usually it exists in the sample itself, otherwise there are different techniques in microscopy or in sample preparation which create or enhance it. The brightness of the image depends on the light gathering performance of the objective

$$\text{Brightness} \propto \frac{(NA)^2}{M^2} \,. \tag{2.5}$$

- Another important parameter is the depth of field; the vertical distance above and below the focus throughout which the image remains at a good quality. This also depends on the NA of the objective [42, 44]

$$\text{DoF} \propto \frac{1}{(NA)^2} \,. \tag{2.6}$$

The above result is deduced when the Strehl Limit is introduced to the equation of the defocus. System that obey that rule maintain good imaging properties.

- Optical aberrations such as spherical aberration, field curvature, coma, astigmatism distort the final image. Usually the amount of these aberrations depends on the characteristics of the lens used and may be corrected with appropriate design for the objective. However, for most of them the correction is limited at the designated image plane and not for the entire field of view. Moreover aberrations are more difficult to correct for higher NA used in optical tweezers.

2.2.3 Köhler Illumination

High quality images require uniform and glare-free illumination of the specimen. A compound microscope is designed in a way that a magnified image of the lamp filament has to come into focus on the diaphragm plane of the condenser, called the aperture diaphragm. Any change in the aperture of this diaphragm alters the angle and the amount of light emerging from the condenser and directed to the specimen; thus it determines the size and the NA of the light cone. The aperture diaphragm has to be chosen appropriately in order to achieve the correct illumination, the best contrast and depth of field; opening it too wide it yields a low-contrast, glared image while setting it too small gives a low resolution image distorted due to light refraction and diffraction from the specimen. Although it is usually overlooked, the condenser aperture has to be correctly chosen, in particular the NA of the condenser to be as close as possible to that of the objective. The minimum acceptable ratio between the two is 70 %, however all manufacturers advise of values around 80-90 %. Parallel rays when they pass through the specimen are focused at the back aperture of the microscope objective. The next plane at which the filament is at focus is the eyepiece diaphragm.

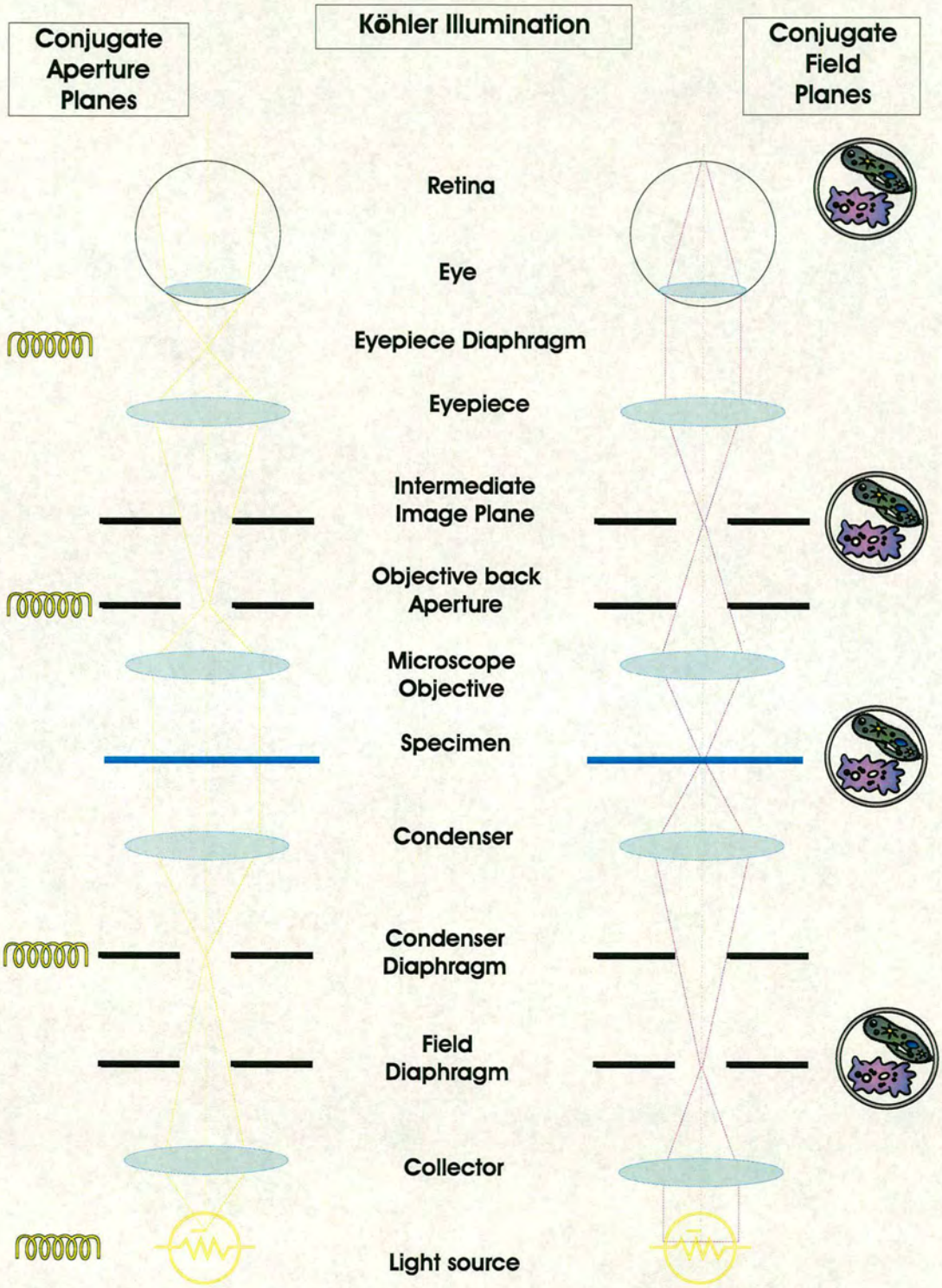

Figure 2.6: Köhler Illumination; the conjugate planes: the image of the lamp filament represents the conjugate aperture planes while the image of the specimen represents the conjugate field planes.

As can be also seen from Figure 2.6 there are four planes with common focus for the illumination pathway; these are the conjugate aperture planes signifying that when there is a restriction in any of these planes the aperture of the illumination will be altered[1]. These planes are:

- The lamp filament
- The condenser aperture diaphragm
- The back focal plane of the microscope objective
- The eyepoint or exit pupil of the eyepiece .

Likewise there is also another set of conjugate planes corresponding to the image formation rays. In each of these planes a focused image of the specimen should appear had the illumination been set correctly. These planes are:

- The field diaphragm
- The specimen in focus
- the intermediate image plane
- The retina of the eye, or the film plane, or the chip of the CCD camera .

A typical procedure of setting up Köhler illumination is as follows [45]:

1. Initially, make sure that all the optics is clean and in place.

[1]When a lens is focusing an object lying in plane S_1 onto a plane S_2, if we place the object in S_2 it will get focused onto S_1. These two planes are called conjugate planes.

2. Switch on the illumination source. Choose the voltage in such a way that the brightness is in the mid-range. Check the image of the lamp filament at the aperture diapragm. In case it is not focused arrange the tilt of the mirror at the back of the lamp.

3. Open fully both the field and the aperture diaphragms. Place a specimen on the microscope stage and check whether there is light going through it.

4. Move the condenser lens as close as possible to the specimen. Using a low power objective bring the specimen into focus. At this stage maybe the fine details of the sample are not yet resolved. Check the brightness of the image and adjust it if necessary.

5. Narrow down the field aperture diaphragm until its edges can be seen in the field of view; it is usually a polygon. By moving the condenser, focus the image of the field diaphragm on the object plane. Center the image of the field aperture diaphragm by laterally shifting the condenser lens. It would be better to close the diaphragm in order to center it more accurately. Every time a different objective is used the condenser has to be centered again. Then open the field diaphragm until its edges is just at the edge of the field of view.

6. Adjust the condenser aperture so that its NA is around 80% of the NA of the objective; this means that the image of the aperture has to be slightly smaller than the objective exit pupil.

Correct adjustment of the microscope, following the Köhler illumination rules yields a homogeneously illuminated field the size of which can be decided independently of the NA of the condenser. The resolution of the resulting image is the maximum that can be achieved both in lateral and axial directions. Furthermore, the contrast which is crucial for the fine details of the specimen is enhanced when the front focal plane of the condenser and the back focal plane of the objective are conjugate [40].

2.2.4 Oil Immersion Technique

As can be seen from equation 2.3, the NA of a microscope objective is limited when a dry objective is used; i.e. when there is air between the objective and the coverslip. Theoretically the maximum value of the NA in this case should be 1 but in practice it is 0.95 since the half angle of the angular aperture has a practical upper limit of $\theta \approx 72\,°$. In order to increase the NA and thus enhance the resolution and the brightness of the image an immersion medium is used: glycerin, oil or water which have refractive indices higher than 1.

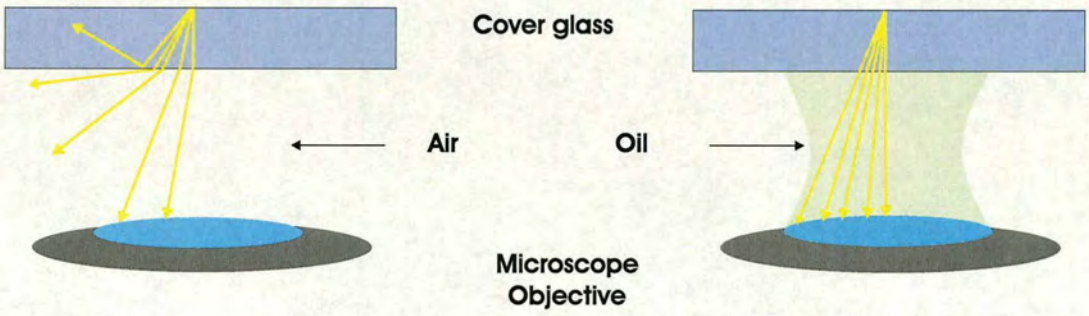

Figure 2.7: Influence of the immersion medium on the NA of the objective. The oil in the right figure, enhances the ability of the microscope objective to collect light rays coming from the specimen.

The most common one used is oil with a refractive index $n_{\text{oil}} = 1.515$ the same value as the refractive index of glass coverslips. The advantage is that now there is no refraction at the coverslip-oil interface as there was in the coverslip-air one, therefore the number of light rays missing the objective is reduced dramatically, even eliminated. This results in a reduction in the depth of field and increase the susceptibility of the system to optical aberrations.

2.2.5 Building a Microscope

In the initial implementation of the tweezers system it was chosen to use a component built microscope for flexibility and cost-efficiency. In this first stage the task was to assemble this instrument for white light and check its resolution. Figures 2.8 and 2.9 give a schematic diagram and a photograph of the microscope built.

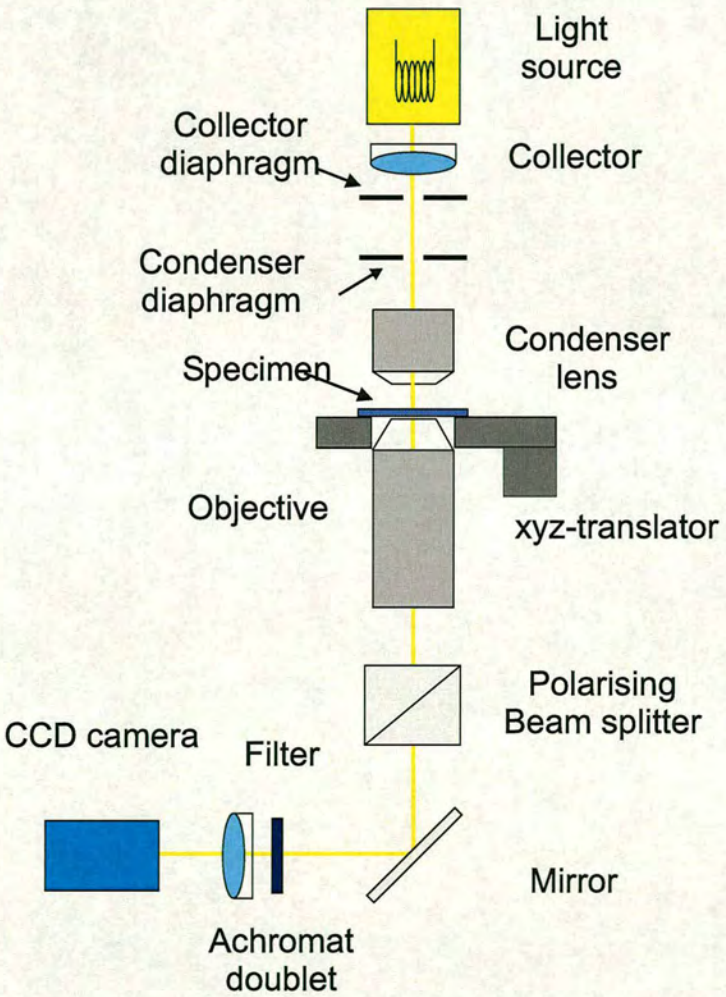

Figure 2.8: Schematic diagram of the home-built microscope.

The initial design was a conventional upright microscope but the next version was an

inverted one; a microscope where the illumination and the condenser are above the stage, and the microscope objective lies just below the sample. The advantage of such a design is that the condenser lower lens is further away from the specimen than the front lens of the objective in the upright version, giving more access to the specimen and the ability to use extra equipment needed for some applications. It provides also extra advantage in an optical tweezers setup for reasons explained in that section.

The main component to choose was obviously the microscope objective. The choice was a NIKON 100×, oil immersion objective with NA = 1.4 Plan Apo, infinity corrected. The tube lens used was 200 mm corresponding to the design of the objective. The rest of the components were common optical components from different companies and the choice of the dimensions and optical properties were made based on the specific design; for example the condenser focal length was chosen in order to match the NA of the objective as much as possible, while the collector focal length had to match the dimensions of the filament. The magnification of the microscope depended on the camera or eyepiece used while the resolution which is mainly due to objective was measured to be 0.3 μm, see Figure 2.10. Figure 2.11 gives a snapshot from a sample consisted of distilled water and 3 μm polystyrene beads.

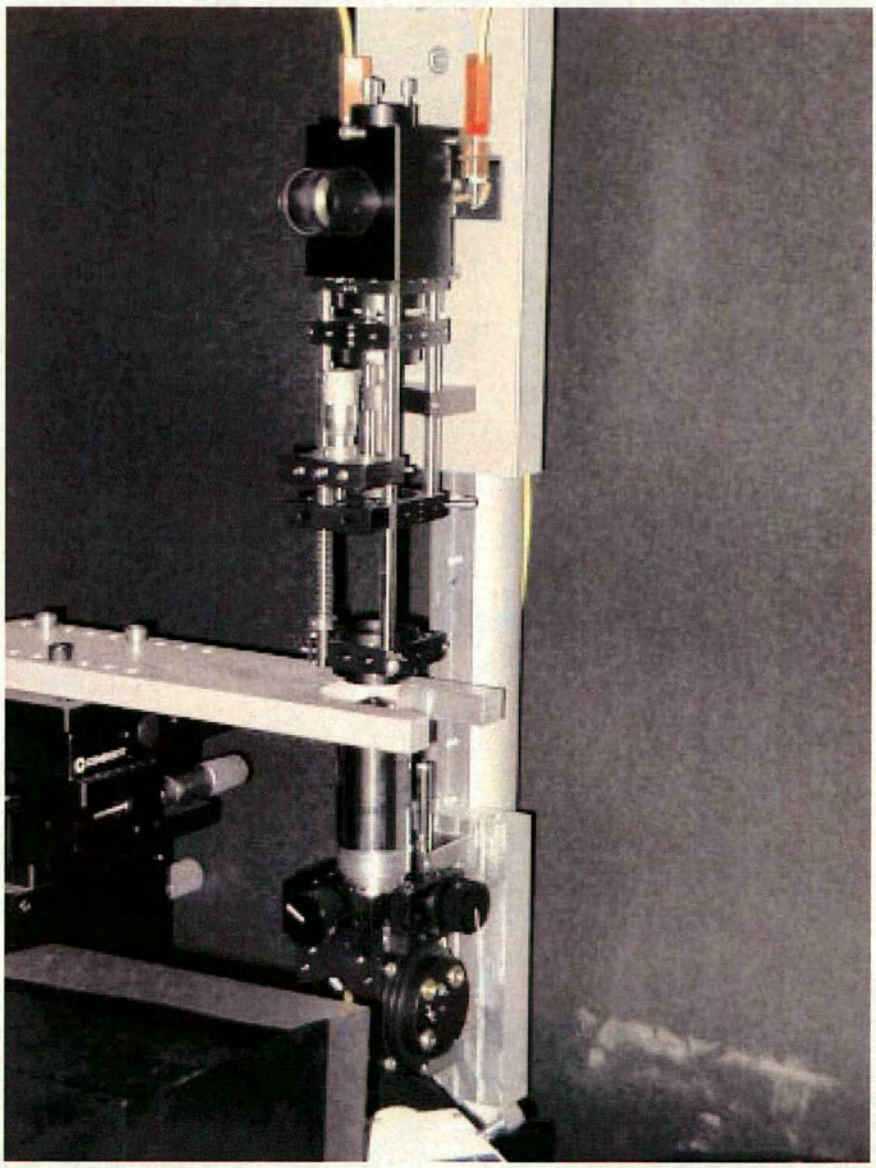

Figure 2.9: Photograph of the home-built microscope.

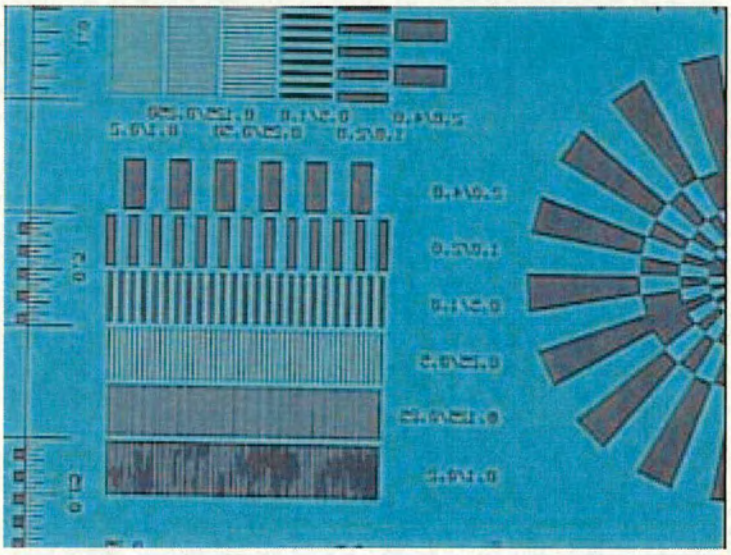

Figure 2.10: Image of the test slide.

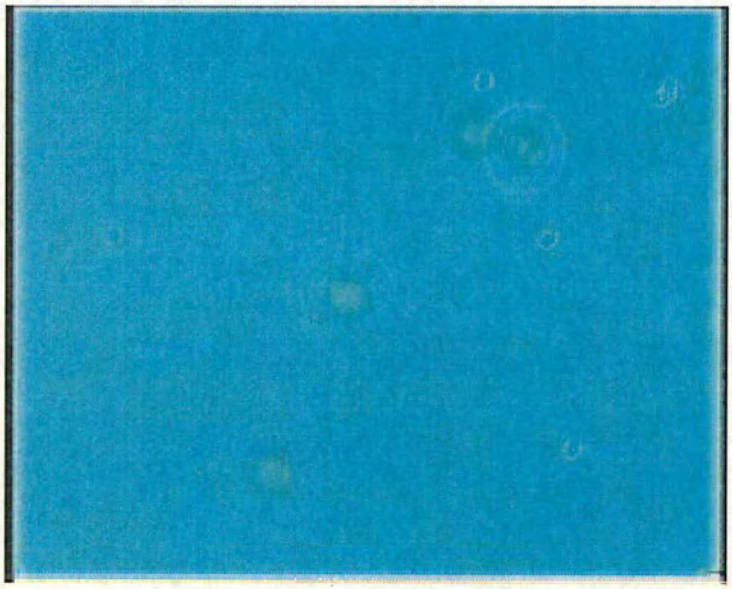

Figure 2.11: Image of the sample; 3 μm polystyrene beads in water.

2.3 Optical Tweezers

2.3.1 Optical Forces

The physics of optical traps is based on the radiation pressure, that is the forces exerted to particles due to the change of light momentum when the light interacts with matter.

Light comprises of photons, each one having energy and carrying momentum equal to

$$E = h\nu \quad \text{thus} \quad p = \frac{E}{c} = \frac{h}{\lambda}\,, \tag{2.7}$$

where h is Planck's constant and c is the velocity of light. When light rays are impinged on a nearly-transparent dielectric particle with refractive index higher than the surrounding medium, each of these rays undergoes refraction, reflection and absorption. Assuming that the amount of absortion is small, since light carries momentum its deflection leads to a change of momentum. Initially light has only longitudinal momentum but finally it has also a tranverse component of momentum [46]; therefore a force equal to that change but in the opposite direction is going to apply on the particle as can be seen from Figure 2.12.

The total optical force can be analysed into two components: the scattering force being parallel to the light propagation and arising from the scattered photons, and the gradient force being proportional to the gradient of light intensity and pointing in the same direction as the gradient [4]. To achieve a three-dimensional stable trap there are certain requirements which have to be met and will be examined in the following section. In order to explain how tweezers work, two different approaches are used depending on the relationship between the wavelength of the laser beam used for trapping and the size of particles. When the particle is much larger than the wavelength the particle is in the Mie regime (when ray optics applies) otherwise it is in the Rayleigh regime [47].

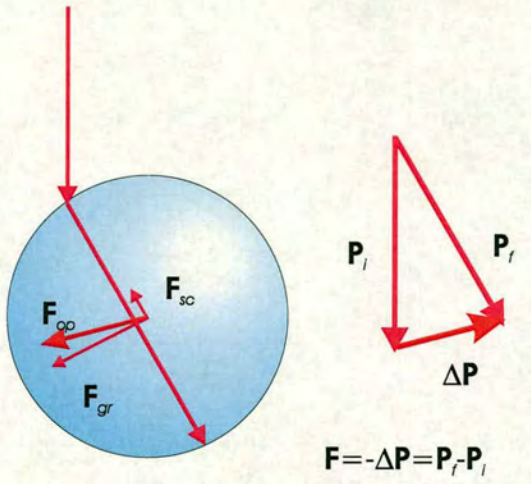

Figure 2.12: Optical forces: basic principle. The light entering an object with a higher refractive index changes momentum. The total optical force can be decomposed into two components: the scattering and the gradient force.

2.3.2 Ray Optics Regime

If particle size is $\gg \lambda$ the ray optics model is applied. In this region the diffraction effects arising from the wave nature of light are neglected and since the size of the volume of the focus is in the order of the wavelength and we can assume that it is a point. In this regime, laser light can be represented by parallel rays propagating in the same direction as the energy flow; after passing through the objective lens the rays are converging to the focus [48]. By encoutering the particle's surface the rays are both reflected and refracted as can be seen in Figure 2.13.

The forces due to any single ray are given by [49]:

$$F_{\text{scat}} = \frac{n_m P}{c}\left\{1 + R\cos 2\theta - \frac{T^2[\sin(2\theta - 2\epsilon) + R\cos 2\theta]}{1 + R^2 + 2R\cos 2\epsilon}\right\} \tag{2.8}$$

and

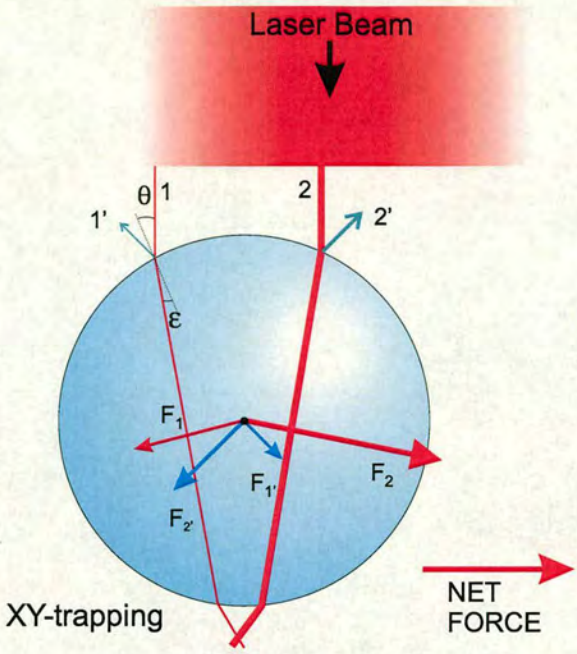

Figure 2.13: A ray optics picture of the scattering and gradient forces for lateral trapping. The red arrows give the gradient force while the blue give the scattering force. The light intensity from the laser has a Gaussian profile and it is depicted here by the darker colour region in the middle of the light beam. Also the difference in thickness of the arrows reflects the different magnitude of the forces, i.e. F_2 is larger than F_1. As can be concluded from the above diagram the gradient force plays the key role for lateral trapping, since the scattering force acts in the direction of light propagation, in z-axis.

$$F_{\text{grad}} = \frac{n_m P}{c}\left\{R\sin 2\theta - \frac{T^2[\sin(2\theta - 2\epsilon) + R\sin 2\theta]}{1 + R^2 + 2R\cos 2\epsilon}\right\}, \tag{2.9}$$

where n_m is the refractive index of the surrounding medium, θ is the angle of incidence, ϵ is the angle of refraction and R and T are the Fresnel reflection and refraction coefficients. The overall force exerted on the particle is going to be the vectorial sum of each of these forces arising from the different rays.

From the explanation of the optical forces one can conclude the essential requirements for three dimensional trapping: If the intensity of the light is the same throughout the cross section then the resulting gradient force will equal zero as can be easily visualised

from the above Figure. By using a source with a Gaussian profile, rays emerging from different regions of the laser are going to have different intensity and carry different momentum and energy. Therefore, the forces imparted on the particle from different rays are going to have different magnitudes as shown in Figure 2.13 F_2 is larger than F_1. Obviously in that case the total force acting on the object is directed towards the region of higher light intensity and it is trapped in the $x - y$ plane.

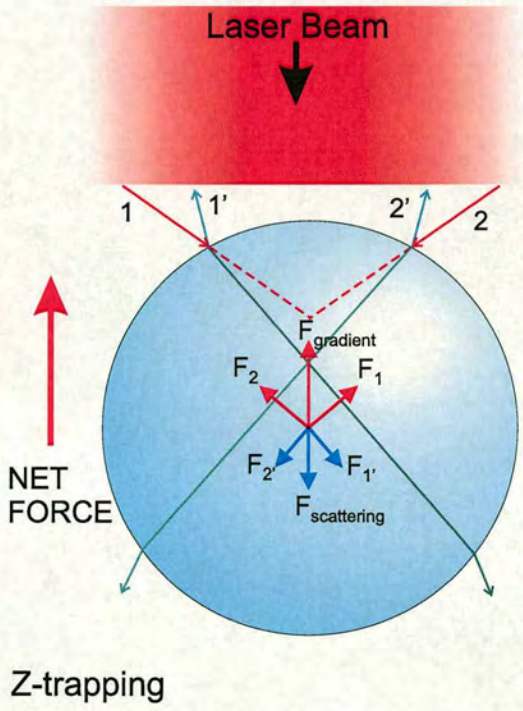

Figure 2.14: A ray optics picture of the scattering and gradient forces for axial trapping. The red arrows give the gradient force while the blue give the scattering force. The light intensity from the laser has a Gaussian profile and it is depicted here by the darker colour region in the middle of the light beam. In this case a stable trap is created if the total gradient force overcomes the total scattering force. Thus, the object is driven towards the focus.

For trapping in the axial direction the total gradient force has to overcome the total scattering force as can be seen in Figure 2.14. In order to maximize the gradient force the beam has to slightly overfill and be focused by a high NA microscope objective;

thus the outer rays are highly convergent and they contribute significantly to the trapping force. From Figures 2.13 and 2.14 it is obvious that for lateral trapping is the gradient force that plays the key role, while for axial trapping the stable trapping position is below the focus where the forces have different signs (above the focus both forces have the same sign). Another interesting note is that if the rays are reversed the direction of the gradient force remains the same, but this does not apply for the scattering force. Furthermore, if the refractive index of the particle becomes lower than the one of the immersion medium it is now the gradient force which changes sign and the trap becomes unstable.

2.3.3 Rayleigh Regime

In this regime the description of the trapping forces is based on the wave nature of light; light is a time-varying electromagnetic field so when it passes through a dielectric object (and by accepting that, in this limit the electromagnetic field is uniform across the particle) it induces point dipoles. The total force decomposes again into the same two components: the scattering force is given by the equation [49]

$$F_{\text{scat}} = n_m \frac{\sigma \langle S \rangle}{c} , \tag{2.10}$$

where σ is the scattering cross section of a Rayleigh particle with radius r

$$\sigma = \frac{8}{3}\pi k^4 r^6 \left(\frac{m^2 - 1}{m^2 + 1} \right)^2 , \tag{2.11}$$

$\langle S \rangle$ is the time-averaged Poynting vector, c and k are the velocity and the wave number of the light respectively, n_m is the refractive index of the surrounding medium, n is the refractive index of the particle and m is the relative refractive index $m = n/n_m$.

The gradient force is [49]

$$F_{\text{grad}} = \frac{\alpha}{2} \nabla \sigma \langle E^2 \rangle \,, \tag{2.12}$$

where α is the polarizability of the particle

$$\alpha = n_m^2 r^3 \left(\frac{m^2 - 1}{m^2 + 1} \right) \,. \tag{2.13}$$

2.3.4 Setup Configuration

The construction of an optical tweezers setup is built around a light microscope; there are several rules which one must follow in order to achieve a stable three dimensional trap. The laser beam has to enter the back aperture of the microscope objective without obstructing the operation of the microscope. The beam must converge to a tight diffraction-limited focus, i.e. the smallest spot, through a microscope objective with high NA in order to reach the maximum convergence of the rays and light gradient. Thus, the gradient force and the trapping efficiency are maximised. The beam has to be configurated (usually expanded) in order to slightly overfill the back aperture of the objective which yields the minimum spot size for the wavelength used. The trap position has to be parfocal with the specimen plane, since the optics of the microscope is designed to minimise aberrations at that plane.

Although tweezers can be built around a traditional microscope where the image is formed at 160 mm away from the back focal plane of the objective, the new infinity corrected microscopes have proved to give more flexibility. In the latter the rays emerging from the objective are parallel and be brought to focus by a tube lens; the tube length has no physical constraints, therefore a number of additional components such as filters, mirrors etc. can be implemented without altering the optics. Furthermore, a collimated laser beam is focused easily at the specimen plane, while at the tranditional microscopes one should arrange the beam so the light entering the objec-

tive should diverge from a point at 160 mm away, in order to be focused at the correct plane.

It is usually required that the trap moves with respect to the specimen without loosing its efficiency. This can be accomplished either by moving the microscope stage or the laser beam itself. While the first way is quite straightforward, the second one is more elaborate: lateral displacement of the trap is realised by changing the angle at which the beam hits the back aperture of the objective while maintaining the beam centered at the back aperture. There are different ways to scan the beam: rotating galvanometer mirrors, deflecting the beam with acousto-optic modulators, moving the end of an optical fiber or use of one of the lenses of a relay-pair. For vertical movement one can use either a lens to make the beam slightly convergent or divergent or move the stage and take advantage of the parfocality of the specimen and trapping planes.

In our lab we initially built an optical tweezers setup based on a home built microscope. An He-Ne laser at λ = 633 nm running at 35 mW power was expanded in order to match the back aperture of the microscope objective and then directed to the microscope with a set of mirrors. Figure 2.15 is a photograph of the setup where 1 μm and 3 μm polystyrene spheres suspended in water were trapped successfully. A second development was to move the trap in a commercial microscope (NIKON TE2000) shown in Figure 2.16. Figures 2.17 and 2.18 show two still images of 1 μm and 3 μm trapped beads, respectively.

2.3.5 Conclusions

A home built microscope offering flexibility and good optical resolution was built. Optical tweezers setups were built around both home made and commercial microscopes demonstrating for the first time trapping within the University.

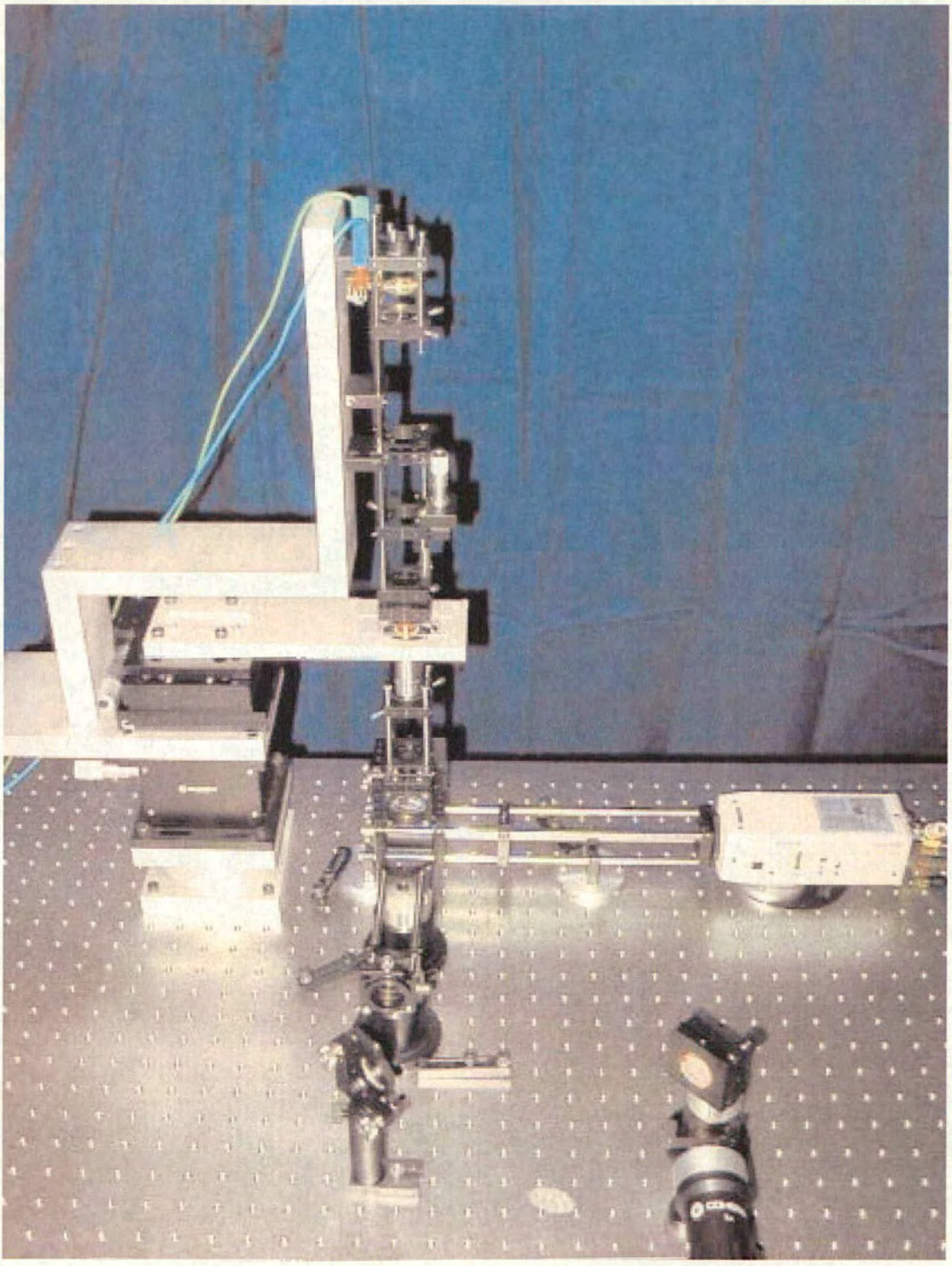

Figure 2.15: Optical tweezers incorporated in a home build microscope.

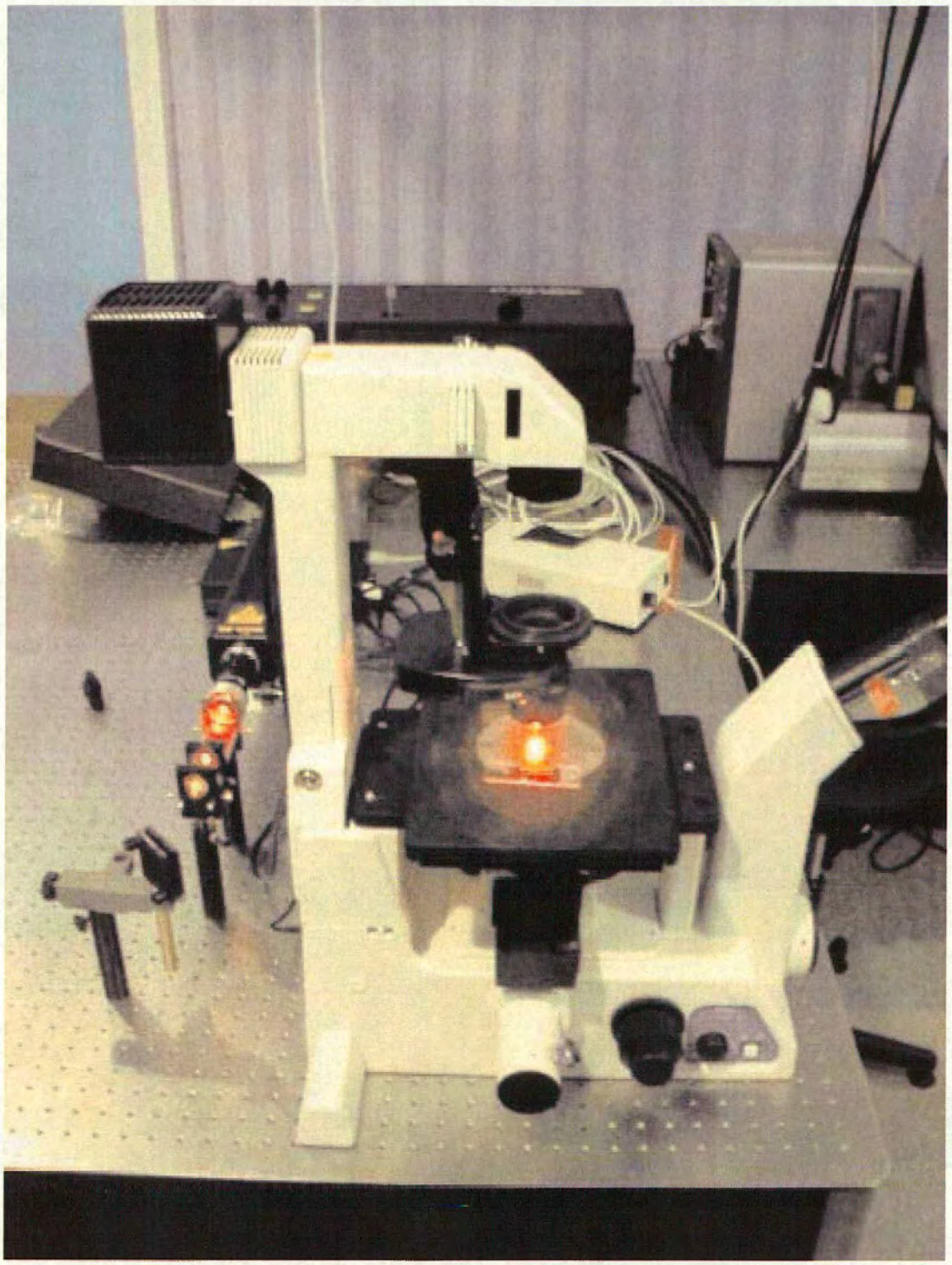

Figure 2.16: Optical tweezers built around a Nikon commercial microscope.

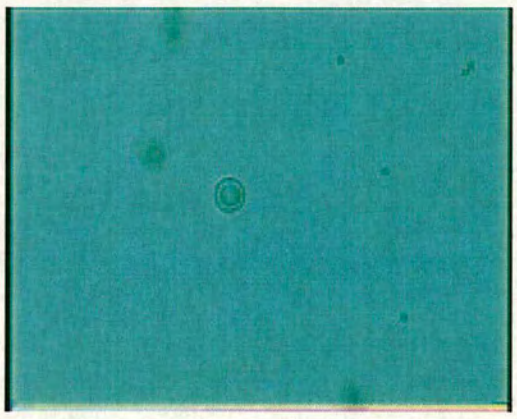

Figure 2.17: 3 μm polystyrene bead in water trapped by He-Ne laser beam (field of view 60×40 μm).

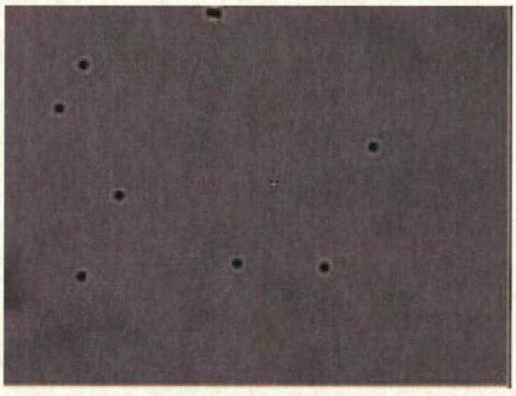

Figure 2.18: 1 μm polystyrene bead in water trapped by He-Ne laser beam (field of view 90×68 μm).

Part I

DNA Studies using Optical Tweezers

Chapter 3

Techniques and Materials for Single Molecule DNA Studies

3.1 Introduction

Single molecule detection has lately become an indispensible tool in the biophysical and biochemical research [50, 51]. Direct observation of single molecules with conventional microscopes is not possible, since their spatial resolution is inadequate for imaging molecules with size smaller than the diffraction limit of the wavelength of the light used. Moreover electron microscopy provides higher resolution but it has limited dynamic information [52].

Single molecule detection combines two very power techniques: single molecule fluorescence imaging and optical tweezers. The first is realised by tagging molecules with fluophores; thus, individual molecules can be observed under a fluorescence microscope. The advantage is that the obtained data is not the average behaviour of a selection of molecules, but the average behaviour of an individual molecule. Furthermore, by using optical tweezers these molecules can be stretched and/or manipulated.

In this case, since their small size inhibits direct trapping of the molecule itself, a polystyrene bead is used as a handle by attaching to the molecule.

In this chapter, the combination of the single molecule fluorescnce imaging with optical tweezers is explained. The setup combined with different types of flow cells was used to study DNA deformation under uniform flow and DNA condensation. A brief description of the DNA molecule and the DNA sample preparation, along with the initial images of DNA molecules, is also given.

3.2 Fluorescence Microscopy

Fluorescence is the emission of light from a substance when it is excited by radiation [53]. Fluorescence microscopy is the technique used to detect mainly biological samples like molecules, proteins or other structures inside the cell. Fluorescence molecules absorb light at a specific wavelength and after a short interval, called the fluorescence lifetime, they re-emit light at shorter wavelength. The absorption of light is very rapid (10^{-15} sec) and corresponds to an electron rising from the ground state to a higher energy state, called the excited state. Electrons in this state are unstable and will return to the ground state with emission of a photon (light) and heat. The emission energy is the fluorescence and the wavelength of the emitted light is longer than the absorbed one corresponding to less energy. The lost of energy is due to interactions of the molecule with its environment before re-emission and it is manifested in the form of heat.

A fluorescence microscope is a conventional microscope with additional components and features that extend its capabilities. The fluorescence image produced is still magnified but this time the light source is not the one used in brightfield microscopy, but the light emanating from the fluorescent molecules [42]. There are two different light paths for fluorescence microscopy [53]: the diascopic or transmitted fluorescence applied mainly in the early systems, where the excitation light is directed to the sample

through the brightfield condenser lens and the emited light is gathered from the microscope objective; and the most used one, which has been developed quite recently, epi-fluorescence microscopy. Here, the objective serves both for focusing the illumination on the sample and collecting the emitted fluorescence. In the latter setup a dichroic mirror is essential to separate the excitation and emission paths; initially the excitation light is reflected by the dichroic mirror into the back aperture of the objective, which acts in this case as a condenser. The sample fluorescence is collected by the objective and light passes through the dichroic towards the eyepiece or the camera. The dichroic beamsplitter is designed in order to reflect the shorter wavelenghts and transmit the longer ones since the emission energy is lower than the exciting one. Figure 3.1 gives a schematic diagram of the optics of a typical fluorescence microscope.

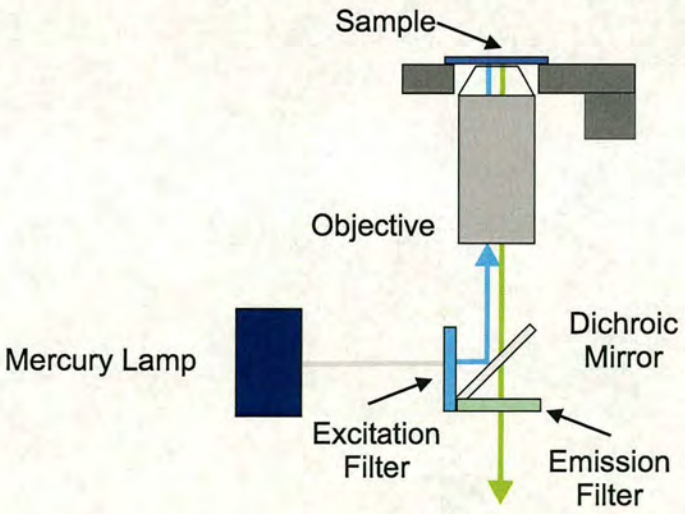

Figure 3.1: Fluorescence optical paths in epi-fluorescnce microscopy: blue line indicates the excitation light and green line the emission light.

In practice, there are two additional filters used in order to enhance the performance of the beamsplitter [43]: an excitation filter placed in the excitation optical path just prior to the mirror in order to select the correct excitation wavelength and the emission filter placed in the emission optical path after the mirror and serves as a selector for

the emission wavelength by cutting all other wavelengths including a small amount of excitation light that is reflected off the sample.

3.3 Introducing DNA

Deoxyribonucleic acid or better known as DNA is a biopolymer controlling the operation of all living cells. It exists in the cell in the form of chromosomes which are arranged in pairs with two members of each pair being almost identical. Figure 3.2 shows a schematic drawing of the structure of DNA.

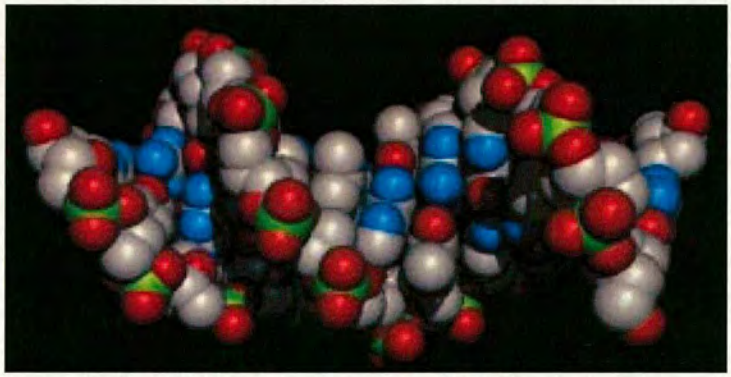

Figure 3.2: The DNA molecule.

The DNA molecule is composed of two strands which coil together to form a 'double helix' [54]. Each strand consists of a series of units called nucleotides, linked to each other with a certain 'directionality', in a head to tail sense known as '5-prime to 3-prime', while the two strands of the molecule run in opposite directions. Each nucleotide consists of about 20 atoms (such as carbon, nitrogen, oxygen) which can be organised into three different groups connected in a particular way: sugar, phosphate and base. Four different types of nucleotides exist in a DNA molecule: they all have the same sugars and phosphates but have four different bases attached to the chain: Adenine, Guanine, Cytosine and Thymine. These bases join the two strands of the DNA

by hydrogen bonds: adenine bonds with thymine and guanine bonds with cytosine. The reason why DNA forms a helix is explained as follows: Phosphates and sugars are very soluble in water but bases are not; they are hydrophobic substances. For the DNA molecule to be stable in water at neutral pH the bases have to come together into the centre of a folded structure, in order to avoid the water. Consequently, the sugars and phosphates are to be located on the outside. The distance between adjacent sugars or phosphates in the DNA chain has a mean value of 6 Å, while the thickness of a base is 3.3 Å which leaves DNA with a hole of 2.7 Å between the bases. In order to get rid of these holes the most obvious form of DNA is an assembly where the two chains climb from the horizontal at an angle of 30° lying on the surface of a cylinder of diameter 18 Å; and the base pairs at the core of the helix are arranged as in the treads of a spiral staircase. Most DNA double helices are right-handed because of certain details of their chemical structure. Moreover, the chemical interactions between base pairs within the helix results in antiparallel chains for natural DNA.

The length of human chromosomes is ≈ 2 m, much larger than the diameter of a typical human cell at about 10 μm. The chromosomes are packed within the nucleus (2 μm). The volume of the DNA and the nucleus of the cell are

$$V_{\text{DNA}} = \pi r^2 L \quad and \quad V_{\text{nucleus}} = \frac{4}{3}\pi R^3 , \tag{3.1}$$

where r and L are the radius and the length of DNA respectively, R is the radius of the cell nucleus. By applying these values for human DNA we obtain a volume fraction of

$$\phi = \frac{V_{\text{DNA}}}{V_{\text{nucleus}}} \approx 1 , \tag{3.2}$$

which shows that the DNA is extremely compacted.

3.4 DNA Preparation

In the two experiments presented in this thesis, bacteriophage λ DNA (New England Biolabs), 48502 bp, 16.5 μm contour length, was used. In the shape experiments

the DNA was at its full length, where in the condensation two different lengths were studied. When a smaller DNA is used, the fragment was made by mixing λ DNA with endonuclease XbaI (Sigma) which cleaves DNA at position 24,508 so the length of DNA is now 23,994 bp giving a contour length of 8.2 μm. The fragment was obtained by mixing 50 mM Tris-HCl pH 7.5, 10 mM $MgCl_2$, 100 mM NaCl and 1 mM dithioerythritol and incubating for 1 hour at 37 °C. For both lengths the preparation method was the same, the one suggested by Bianco *et al.* [55].

Initially λ DNA is annealed, using a biotin-labelled 12-mer oligo (GD-cos1bio, F79654, New England Labs), at the cos1 site of DNA. The reaction between biotin-DNA is at 1:1 ratio, but in order to assure the annealing of the molecule the biotin was added at a $\times$ 500 excess; in this case 30 μl of Tris-Buffer with 1 μl of λ DNA and 0.73 μl of biotin were mixed. The sample was then placed in a water-bath for 30 min at 65 °C and then cooled down for 16 hours remaining in the water-bath. The next step was the ligation of DNA : that was done by adding to the previous sample 3.64 μl of ligase buffer and 1 μl of T4 DNA ligase (NEB 2025, 20000 units) and leaving it in the water-bath for 16 hours at 16 °C. The final volume of the sample was 36.37 μl and the concentration 872.86 pM. After that stage the sample can remain in fridge for several days and serve as the source for daily experiments.

The biotin-tagged DNA was then attached to 1 μm streptavidin-coated polystyrene beads (Bangs Laboratories) through the non-covalent, but still strong interaction of biotin-streptavidin. In order to achieve a ratio of 9:1 DNA:beads 0.95 μl of beads was mixed with 5.31 μl of Tris-Buffer and subsequently 0.69 μl of the DNA sample was added. After mixing it quite gently the sample was put into incubator for 1 hour at 37 °C. Then DNA was fluorescently labelled using YOYO-1 : 7.27 μl of YOYO-1 at C = 0.1 μM was introduced into the sample which was then put back into incubator for 90 min at 37 °C covered by foil. The concentration at this point was measured at 42.19 pM and 90 pM for the two lengths respectively.

Just before the experiments were run, 2 μl of the final sample were diluted in 750 μl of buffer comprising of 720 μl Tris-HCl (20 mM, pH 8), 15 μl i.e. 2% of 2-mercaptoethanol and 15 μl of anti-fading agent (made by mixing 2.3 mg/ml D-(+)-glucose, 0.1 mg/ml glucose oxidase, 18 μg/ml catalase and 20 mM 2-mercaptoethanol). The above technique was established by Dr T.J. Su. The term ionic strength is used in order to give the overall ionic properties of a solution, regardless of the sign of the charge and chemical properties of its ionic components [56]. The ionic strength of a solution is given from the following equation:

$$I = \frac{1}{2}\sum_{i=1}^{n}(c_i \cdot z_i^2) \ . \tag{3.3}$$

The sample consists of 20 mM Tris·HCl, 5 mM NaCl and 2 mM Spermidine.

For Tris and making the assumption that is half dissociated

$$Tris \cdot HCl \leftrightarrows TrisH^+ + Cl^- \ , \tag{3.4}$$

so

$$I = \frac{1}{2}\frac{1}{2}\sum_{i=1}^{n}(c_i \cdot z_i^2) = \frac{1}{2}[20 \cdot 1^2 + 20 \cdot (-1)^2] = 10 \text{ mM} \ , \tag{3.5}$$

For NaCl

$$NaCl \leftrightarrows Na^+ + Cl^- \ , \tag{3.6}$$

so

$$I = \frac{1}{2}\sum_{i=1}^{n}(c_i \cdot z_i^2) = \frac{1}{2}[5 \cdot 1^2 + 5 \cdot (-1)^2] = 5 \text{ mM} \ , \tag{3.7}$$

For Spermidine

$$Sp^{+3}Cl_3 \leftrightarrows Sp^{+3} + 3Cl^- \ , \tag{3.8}$$

so

$$I = \frac{1}{2}\sum_{i=1}^{n}(c_i \cdot z_i^2) = \frac{1}{2}[2 \cdot 3^2 + 3 \cdot 2 \cdot (-1)^2] = 12 \text{ mM} \ . \tag{3.9}$$

The total ionic strength is

$$I = 10 + 12 = 22 \text{ mM} \tag{3.10}$$

for the buffer with Spermidine and

$$I = 10 + 12 + 5 = 27 \text{ mM} \tag{3.11}$$

for the buffer with 5 mM NaCl and 2 mM Spermidine.

3.5 Experimental Apparatus

We performed two experiments with DNA: studies of the DNA molecule vertical deformation under uniform flow and the initiation of the DNA condensation. In both experiments the tweezers setup was based on an inverted, epi-fluorescence, commercial microscope (Eclipse TE2000-U; NIKON). The advantage of the microscope used, was the extra height between the base of the microscope and the objective turret (accomplished by raising the upper part of the instrument) which allows the introduction of extra optical components in the optical path below the back aperture of the objective, without any further modification.

The optical tweezers setup was created by focusing the laser beam from a circularised Diode laser (with λ = 785 nm, maximum power 75 mW; Circulase) through an oil immersion objective (100×, NA = 1.4, Plan-Apo; NIKON). The diameter of the laser beam was $\approx$ 1mm and two lenses with f_1 = 30 mm and f_2 = 200 mm were used to expand the beam in order to slightly overfill the back aperture of the objective. The beam was then raised to the required height, by means of a periscope formed by two mirrors. A further set of lenses, both having the same f = 140 mm, formed the relay system. The beam was then directed to the back of the objective after being reflected by a dichroic mirror, selected for the specific wavelength.

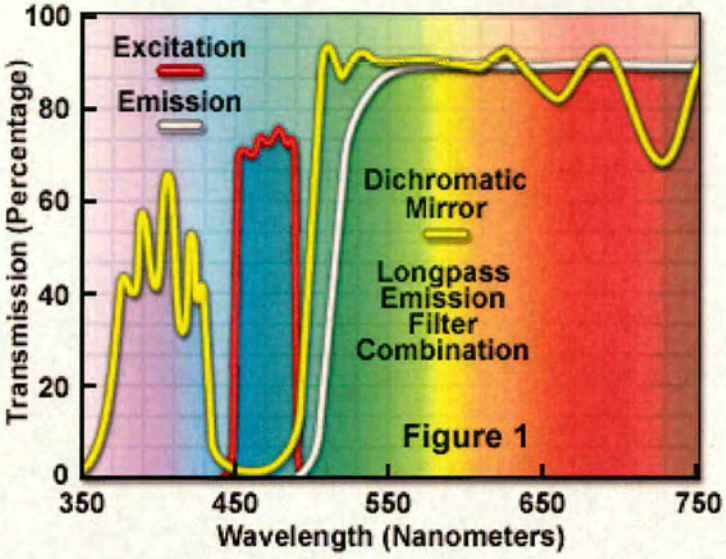

Figure 3.3: Transmissive properties of the Nikon B-2A filter cune. (Source: Nikon webpage at http://www.microscopyu.com.)

The fluorescently labelled DNA was excited with a high mercury lamp (HB-10104AF, NIKON) using the Nikon B-2A filter set with its transmissive properties shown in Figure 3.3 [43]. The latter choice was made to meet the requirements for the used dye; YOYO-1 has its maximum excitation at λ = 491 nm and its maximum emission at λ = 509 nm as shown in Figure 3.4. The crucial part for that setup was to combine fluorescence imaging and the trapping position to coincide at the image plane [57]. This was achieved by making the laser beam slightly divergent i.e. the separation between the two lenses was 24.3 cm instead of the expected 23 cm. Subsequent images of trapped beads, both in brightfield and fluorescence were captured and recorded by a cooled CCD camera (Imager 3, LaVision) as shown in Figure. 3.5. The measured resolution of the microscope was 0.25 μm and the depth of field for the objective 0.2 μm. The field of view was 90 μm in length and 80 μm in width. Figure 3.6 gives the schematic diagram of the set up and the different light paths.

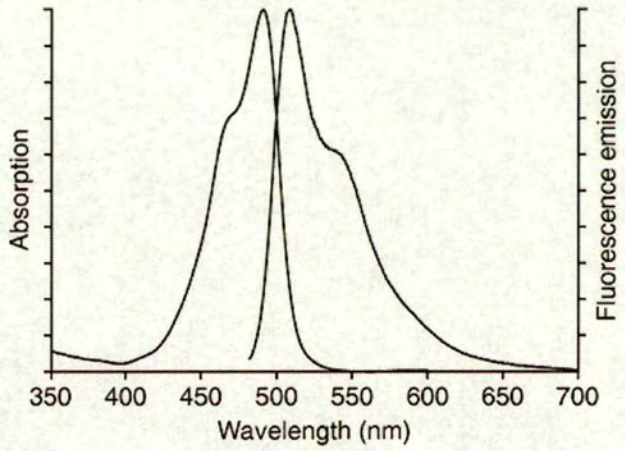

Figure 3.4: YOYO-1 emission and absorption spectra.

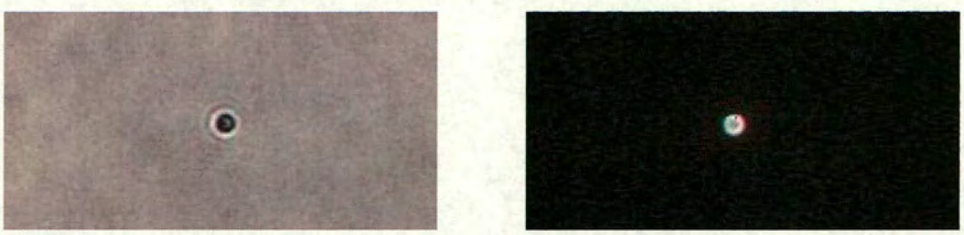

Figure 3.5: Brightfield (left) and fluorescence (right) images of the same trapped bead.

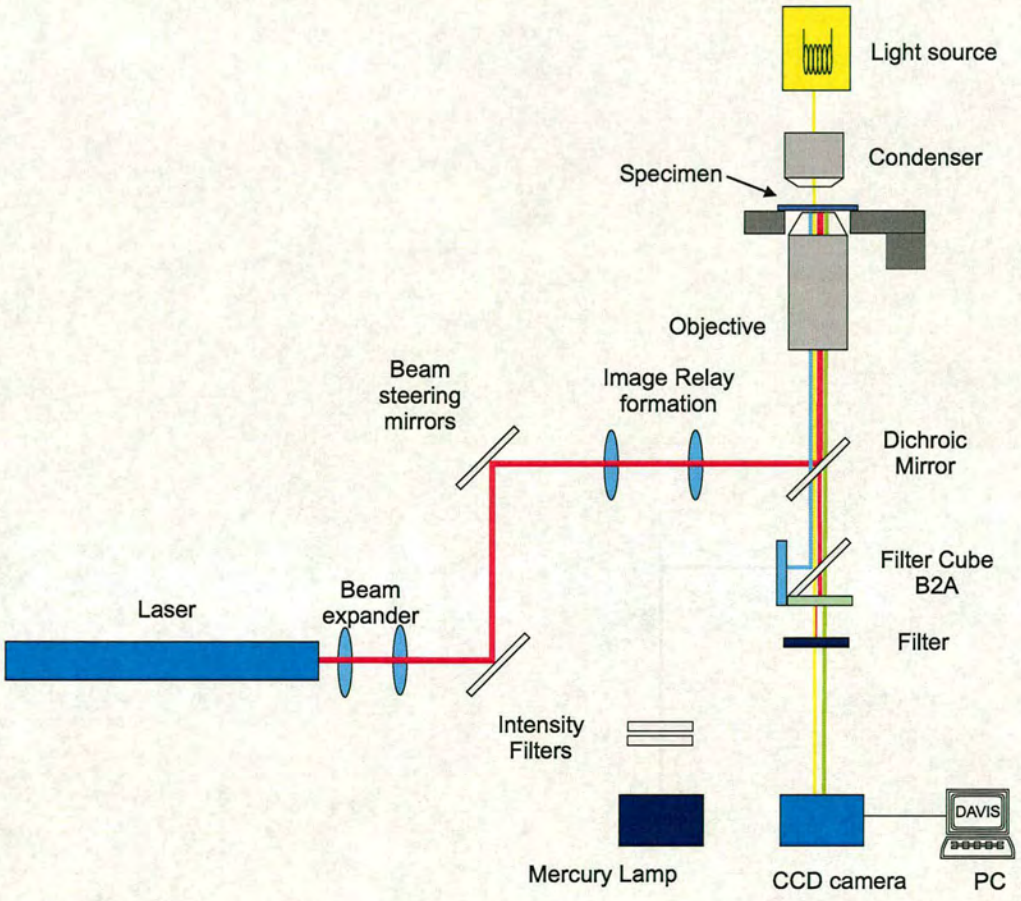

Figure 3.6: Schematic diagram of the fluorescence imaging and optical trapping system incorporated in a commercial microscope. The different optical paths are indicated as follows: red for the trapping laser, yellow for brightfield illumination, blue for excitation and green for emission.

After building the setup and establishing the preparation method of the DNA sample a series of tests were taken to verify the functionability of the system to image and record DNA molecules in flow. In order to observe the DNA molecules a flow cell was constructed. The flow cell was made by milling perspex to a depth of 40 ± 5 μm with a width of 2 mm. The cell was covered by a 0.17 mm thick cover-slip sealed on the perspex with UV-cured glue (61 Optical Adhesive; NORLAND). The inlet and the outlet of the channel were made by drilling the perspex 1.7 mm diameter holes which were then connected to silicon rubber tubing by plastic tips. In order to introduce flow two different methods could be applied: either movement of the stage or use of a syringe pump. The choice of how to achieve flow as well as the shape of the flow cell required depends on the nature of the experiment and will be explained in the chapters of each experiment. Figure 3.7 is a photo of the flow cell used to introduce the samples. Figures 3.8, 3.9 show the initial results from DNA imaging.

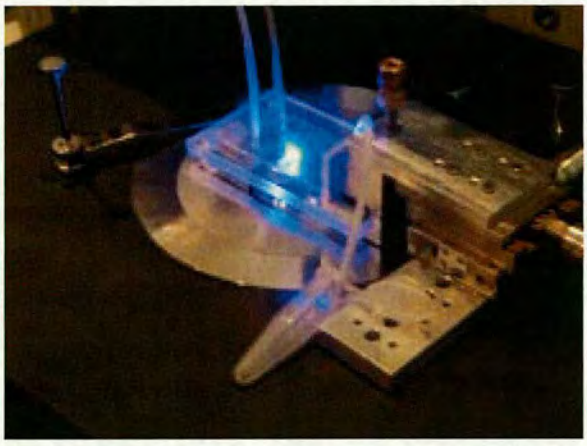

Figure 3.7: Photograph of the flowcell under fluorescence imaging.

From the initial results we were able to verify that the resolution of the fluorescence imaging was good enough in order to distinguish whether there were more than one molecules attached to the polystyrene bead, as shown in Figure 3.10.

Figure 3.8: Fluorescence imaging of DNA: (left) and (centre) the DNA polymer at zero flow, (right) the DNA stretching when flow is introduced in the flow cell.

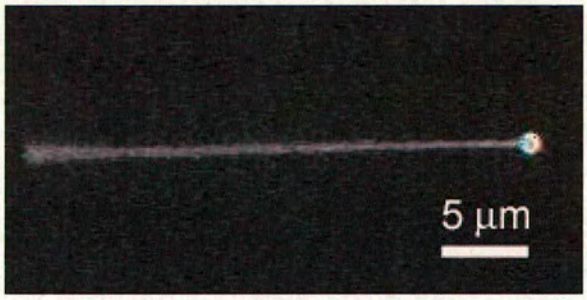

Figure 3.9: DNA concatmer; the shown polymer has a length of 33 μm.

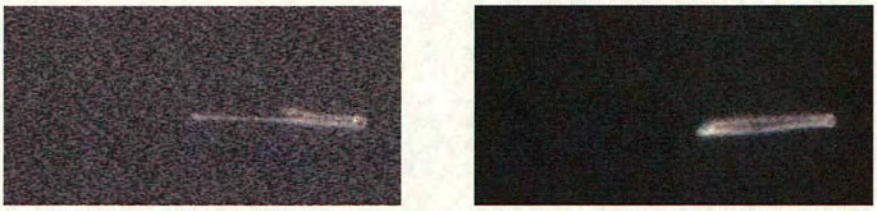

Figure 3.10: Fluorescence imaging of two DNA molecules attached to the same bead.

Chapter 4

DNA Shape under Uniform Flow

4.1 Introduction

The flow behaviour of polymer melts and polymer solutions (non-Newtonian fluids) is very different from that of simple liquids (Newtonian fluids). Non-Newtonian fluids exhibit surprising flow effects such as turbulent drag reduction [58, 59, 60, 61], rod climbing and secondary flows in various geometries [62].

Although the flow behaviour of non-Newtonian fluids is important in many applications such as polymer processing, manufacturing and food industry, it is only for small deformations that their response can be quantitatively described within the context of the linear viscoelasticity theory [63]. The non-linear regime is still the subject of intense experimental [64] and theoretical investigation [65]. For dilute polymer solutions in particular, it is now recognised that we need to develop our basic understanding of the deformation and dynamics of single polymer molecules in different types of flows.

The task appears challenging since

1. Experimentally, classical methods such as light and small-angle neutron scattering [66, 67], rheometry [68] and birefringence [69] measure only average values,

and do not permit the study of effects at the single molecule level.

2. Theoretically, even the simplest possible situation, the flow behaviour of a single macromolecule within a uniform flow, has proven to be complicated [70]: a real polymer chain has many degrees of freedom and full molecular dynamics (MD) simulations are currently impossible; there is a coupling between the polymer deformation and the hydrodynamic field since the flow changes the shape of the polymer chain which in its turn changes the flow field around the chain. This hydrodynamic effect can be of different importance for different parts of the chain; furthermore, the importance of the excluded-volume effect and the finite extensibility of the polymer chain is largely unknown.

Recently, new experimental techniques such as single molecule fluorescence imaging in solution [71, 52] and optical tweezers [72] have allowed the direct observation of DNA molecules under a variety of flows [73, 74, 75, 76, 77, 78, 79]. Results from such experiments hold out the promise of understanding the non-linear deformation of a single polymer chain to an unprecedented degree and detail.

In this chapter, a systematic experimental study of the shape of a DNA molecule stretched out by steady uniform flow at different velocities using optical trapping of single DNA molecules (tethered on polystyrene beads) and single molecule fluorescence imaging is presented. The results show a gradual transition from a regime with strong hydrodynamic interactions at low velocities to a regime with no hydrodynamic interactions at higher velocities.

4.2 Background

Brochard-Wyart *et al.* [80, 81, 82] in a series of papers developed a scaling theory for the deformation of a single chain under uniform flow based on the *"blob"* picture of

single polymer chains [83, 84]. They assumed that the volume occupied by the chain is impenetrable by the flow (non-draining chain). This simple analytical theory predicts four regimes for the overall shape of the deformed DNA molecule. At sufficiently low velocities the molecule is slightly deformed and its size is close to the usual unperturbed dimension. At moderate flow velocities the polymer is stretched and takes a characteristic *"trumpet"* shape. At higher flow velocities the chain section at the tethered point is completely stretched and the chain takes a *"stem and flower"* shape. At the highest velocities the chain is fully stretched.

Perkins *et al.* [75] used uniform flow to stretch a single DNA chain tethered to an optically trapped latex sphere and held stationary at one end (see Figure 4.1). They observed the resulted linear extension L of the DNA at the direction of the flow by single molecule fluorescence imaging. They used DNA molecules of various contour

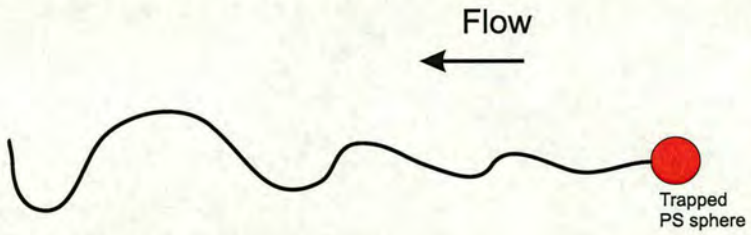

Figure 4.1: Schematic drawing of a single polymer chain tethered to an optically trapped latex sphere and stretched under uniform flow.

lengths L_0 (total length, length measured along the chain backbone) to measure their fractional extensions L/L_0 under different flow velocities v and background solvent viscosities η. While the overall deformed-chain shape observed resembles Brochard-Wyart's predictions, the measured elongation curves $L(v)$ do not agree with the scaling theory. Although DNA is a long molecule (several microns), its persistence length ($\approx$ 50 nm) is large enough to make it a polymer with a relatively low number of Kuhn segments[1] (for example, a DNA molecule with a contour length of 16.5 μm consists

[1]The Kuhn segment is twice as long as the persistence length.

of 165 Kuhn segments). It has been claimed that the applicability of scaling laws and blob theory on such a polymer can be problematic. Perkins *et al.* [75] main result is that the fractional extension is a universal function of $\eta v {L_0}^m$, with $m = 0.54 \pm 0.05$. This result indicates that the influence of the hydrodynamic interactions are significant since if they are not important and the flow penetrates freely and fully the volume occupied by the chain (free-draining chain), the fractional extension is expected to be a universal function of $\eta v L_0$ (the total drag force). Consequently, Perkins *et al.* concluded that the hydrodynamic coupling is so strong that makes the coil to behave like an impenetrable (by the flow) solid object (non-draining chain) even at high velocities. Furthermore, and more importantly, the exponent $m = 0.54 \pm 0.05$ is close to the exponent which one would expect for the size of a polymer chain at *equilibrium size (no flow)*, indicating that the *equilibrium size* instead of the true size should be used for calculating the drag force . This result is very surprising since it is well known that at low Reynolds numbers (and apart from a logarithmic correction[2]) the total drag force is mainly determined by the largest linear dimension [85]; the *true* linear dimension of a DNA molecule elongated by flow, even at low velocities, is several times larger than the equilibrium size. It is clear that the collapse of the L/L_0 vs $\eta v {L_0}^{0.54}$ plots to a universal curve is to a large extent fortuitous and there should be another effect which compensates the underestimation of the linear dimension of the coil. This may be the logarithmic correction which has to be introduced in the functional form of the drag force generated by asymmetric objects. Simulations have recently shown that while for the drag force corresponding to the equilibrium size the collapse of the data to a universal function is approximate, if one considers the *true* drag force[3] the collapse of the data to a universal function is perfect [70]. Perkins *et al.* [75] experiments provided the incentive for several theoretical investigations of the DNA elongation under uniform flow.

[2]The logarithmic correction involves the logarithm of the DNA aspect ratio of the sizes parallel and perpendicular to the flow direction which can take large values at even moderate velocities.

[3]In simulations the true drag force can be easily calculated.

A key concept in many theoretical studies is the worm-like chain (WLC) model. A DNA molecule can be approximated by a thin, elastic, homogeneous rod where the elastic constants are such that small thermal fluctuations produce random, isotropic bending of the chain sections resulting in a random coil for sufficiently long chains [86, 63]. This is a quite general model of a semi-flexible polymer chain called persistent or worm-like chain WLC and accounts for both local chain stiffness and long-range flexibility and is compatible with the particular mechanism of DNA chain flexibility. Bustamante [87] and Vologodskii [88] have shown that the WLC model describes the entropic elasticity of a DNA molecule much better than the freely-jointed chain model [89].

Marko and Siggia [90] used the WLC model to calculate an *approximate* force vs extension, $F(L)$, formula which they used to explain the observed DNA extension-velocity dependence, $L(v)$. They took into account explicitly the logarithmic correction of the drag force and used a mean tension and an effective overall chain deformation. Within the limitation of one adjustable parameter they found good agreement with the experimental measurements.

Larson *et al.* [91] used Monte Carlo simulations which took into account the DNA's elasticity based on the approximate Marko-Siggia WLC relationship [90], $F(L)$, Brownian motion and averaged hydrodynamic interactions to explain the measured chain extension and the DNA mass distribution along the flow direction of Perkins *et al.* [75] and similar experiments using longer DNA molecules [91]. For the longer DNA molecules the exponent m was calculated to be $m = 0.75 \pm 0.02$. They showed that the hydrodynamic interactions act together to create an increased mass distribution at the free end and the extended DNA molecule under steady uniform flow behaves effectively like a half-dumbbell spring with the nonlinear elasticity of the WLC (see Figure 4.2). They argued that the surprising ability of the simple half-dumbbell model with WLC elasticity to explain the experimental results for the fractional extension is due to the following effects which cancel each other: (i) the distribution of drag forces along

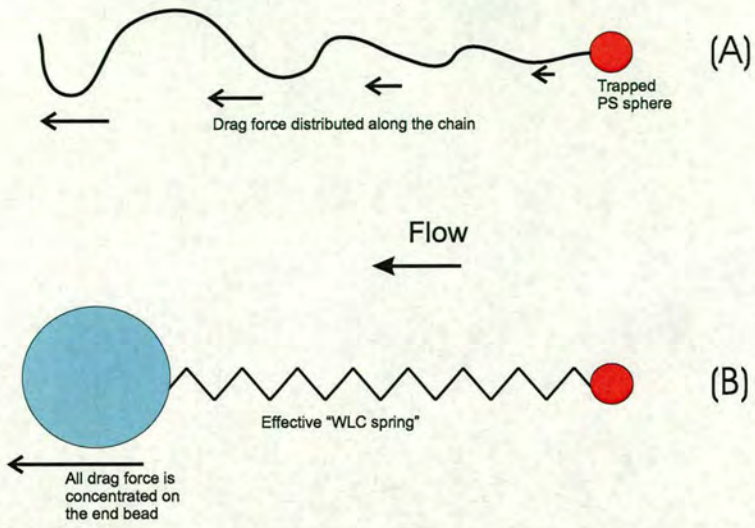

Figure 4.2: The drag force is distributed along the length of the chain (A), but effectively the DNA elongation can be simulated by assuming (B) an effective spring which obeys the WLC nonlinear elasticity and a bead at the free end where the whole drag force is concentrated (half-dumbbell model).

the chain (see Figure 4.2) decreases the slope of the fractional extension with velocity; (ii) the increase of the effective drag coefficient with chain elongation increases the slope of the fractional extension with velocity. It is worthwhile noting that although the half-dumbbell model can fit the extension data it provides no insight about the importance of the hydrodynamic interactions, the finite extensibility of the chain and the excluded volume interactions at different velocities and different parts of the chain at a specific velocity.

Zimm *et al.* [92] and Stigter *et al.* [93] developed theoretical methods on the basis of the *accurate* inverse Marko-Siggia WLC relationship [90], $L(F)$, with averaged hydrodynamic interactions. Both calculations also agree with the measurements of Perkins *et al.* [75].

Rzehak *et al.* [94, 70] performed an extensive numerical study of the deformation of a long polymer chain within uniform flow using Brownian dynamics simulations. Unlike previous numerical and analytical studies they avoided any averaging procedures

for the hydrodynamic interactions and considered systematically a Gaussian chain, a freely-jointed chain and a finitely extensible nonlinear elastic (FENE) chain. They took into account progressively the excluded-volume interactions and the hydrodynamic interactions in order to evaluate the relative importance of these effects to the deformation of the chain. They also developed an analytical blob-model for the free-draining case. The most important conclusion of their studies is that the effect of the excluded-volume and hydrodynamic interactions are position and velocity dependent. They have a stronger influence towards the free end of the chain and are more important at relatively low velocities. Interestingly, they have showed a gradual transition from a nearly non-draining regime at low velocities to a nearly free-draining regime at high velocities. At moderate velocities the flow partially penetrates the polymer coil and the polymer chain is neither non-draining nor free-draining.

These simulations led to the development of a modified blob-model: the so called F-shell blob model [94, 95], which combines the appealing simplicity of the blob-model while taking into account the important effect of the partial draining state of the polymer chain. They also indicated that the experimentally-found chain extension exponents might have no scaling significance since the chain could be in very different draining regimes at different velocities.

Our results are discussed within the framework of the blob models (which are presented in detail in the theory section) and show clearly a gradual transition from a non-draining regime at low velocities to a free-draining regime at high velocities (within the trumpet regime) verifying the numerical predictions and indicating that the F-shell blob model can provide a relatively simple but significant improvement to the initial blob-models for single chain deformation under uniform flow.

4.2.1 Theory

Pincus [83, 84] showed that a single polymer chain under tension can be described by a series of scaling thermal blobs. Each blob corresponds to a length scale where the deformation energy is of the order of the thermal energy $k_{\mathrm{B}}T$, where k_{B} is the Boltzmann constant and T is the absolute temperature. On smaller scales the tension is not important and the chain section can be considered unperturbed following either ideal or swollen statistics (depending on the solvent). On larger scales the deformation energy is larger than $k_{\mathrm{B}}T$ and the conformation is set by the interactions which produce the deformation. The size of the k-th blob R_k is controlled by the balance of the thermal energy $\approx k_{\mathrm{B}}T$ and the deformation energy $\approx R_k F_k$, where F_k is is the total force exerted on the k-th blob:

$$k_{\mathrm{B}}T \approx R_k F_k \Rightarrow R_k \approx \frac{k_{\mathrm{B}}T}{F_k}\,. \tag{4.1}$$

Since each blob is by definition unperturbed from its equilibrium configuration, it satisfies the Flory scaling relationship [89, 96]

$$R_k \approx a {N_k}^{\nu}\,, \tag{4.2}$$

where a is the length of the Kuhn segment (effective monomer unit), N_k the number of Kuhn segments within the k-th blob and the exponent ν depends on the solvent quality: $\nu \approx 3/5$ for a swollen chain due to excluded-volume interactions in good solvent conditions [4] while $\nu = 1/2$ for an ideal chain (chain in a θ-solvent).

The total force F_k exerted on the k-th blob depends mainly on the assumption concerning the hydrodynamic interactions. In the case of a tethered chain in a uniform flow, F_k decreases from the tethered to the free end. This effect according to Equation (4.1) results in increasing blob sizes from the tether to the free end and the polymer chain takes a characteristic "trumpet" shape at moderate velocities. At a limiting velocity

[4] Experiments and more sophisticated calculations have shown that $\nu \cong 0.588$ [97].

the section of the chain near the tethered point can be stretched to such an extent that reaches its minimum size perpendicular to the flow. This is the beginning of the "stem and flower" regime. Figure 4.3 shows a schematic representation of the regimes predicted by the blob models. The first regime accounts for very low velocities where the polymer shape is relatively unperturbed. At higher velocities we progressively acquire the trumpet and the stem/flower regimes. At even higher velocities the polymer chain is fully stretched. The exact deformed shape in the different regimes and their limiting velocities depend on the hydrodynamic model (which governs the drag force) and the solvent conditions. In the following subsections we present the relevant relationships for the trumpet and the stem/flower regimes for the two initial blob models: the non-draining blob model and the free-draining blob model. The more recent partially draining blob model (F-shell blob model) is discussed qualitatively. For the solvent conditions we will present results in the two limiting cases of a θ- solvent and a good solvent. Note that all scaling results are only accurate up to numerical pre-factors that are hopefully not much bigger than unity.

Non-Draining Blob Model

At low Reynolds numbers the drag/hydrodynamic force exerted by the uniform flow with velocity v on a sphere of radius R is given by Stokes law:

$$F = 6\pi\eta v R\,, \tag{4.3}$$

where η is the viscosity of the fluid. The non-draining model supposes that the hydrodynamic coupling within the blobs is so strong that the solvent molecules are completely trapped in the blobs. It is based on the *Zimm model* which treats the pervaded volume of the chain as a solid object moving through the surrounding solvent. The friction coefficient ($\zeta = F/v$) for a blob of radius R is $\zeta_Z = 6\pi\eta R$. The hydrodynamic interactions between the blobs are neglected.

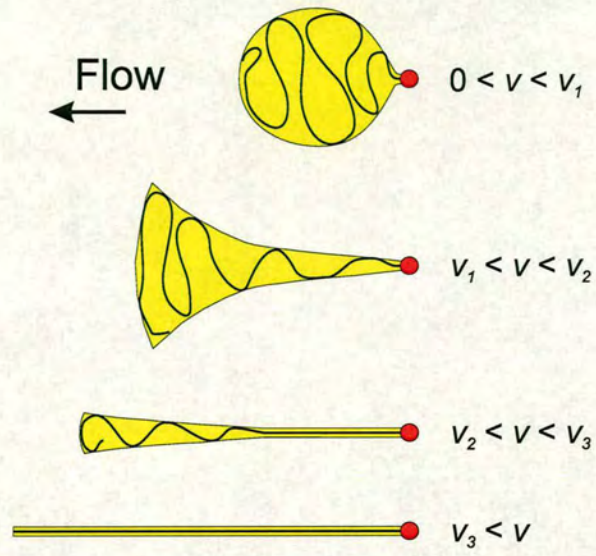

Figure 4.3: Schematic drawing of the overall hydrodynamically-deformed shape of a single polymer chain tethered and kept stationary at one end (red bead on the right) while the other is free under uniform flow. Starting from above: at sufficiently low velocities the molecule is slightly deformed and its size is close to the unperturbed dimension; at moderate flow velocities the polymer is stretched and takes a characteristic "trumpet" shape; at higher flow velocities the chain section near the tethered point is completely stretched while at the free end there is still significant thermal agitation and the chain takes a "stem and flower" shape; at the highest velocities the chain is fully stretched along the whole backbone.

The first blob at the free end (blobs are counted from the free end) experiences only the Stokes drag force, the second blob experiences in addition to the Stokes drag the tension due to the drag of the first blob (Figure 4.4). Thus, the *total force* acting on the k-th is

$$F_k = 6\pi\eta v \sum_{j=1}^{k} R_j \,. \tag{4.4}$$

From Equations (4.1) and (4.4) we can deduce a recursion relationship for the total force F_k exerted on the k-th blob

$$F_k - F_{k-1} \approx \frac{6\pi\eta v k_{\mathrm{B}} T}{F_k} \,. \tag{4.5}$$

In the limit of large k values we can assume that k is a continuous parameter; therefore,

$F_k - F_{k-1} = \frac{dF(k)}{dk}$. Thus from Equation (4.5)

$$F(k) \approx (12\pi\eta v k_B T k)^{1/2} . \tag{4.6}$$

In addition, from Equations (4.1) and (4.6) we deduce that the position of the k-th blob is

$$x(k) \approx 2\left(\frac{k_B T k}{12\pi\eta v}\right)^{1/2} . \tag{4.7}$$

Eliminating k from Equations (4.6) and (4.7) (or starting from Equation (4.4) and since $x_k = \sum_{j=1}^{k} R_j$ (see Figure 4.4)) we can deduce that

$$F(x) \approx 6\pi\eta v x . \tag{4.8}$$

The segment density $\rho(x)$ projected onto the flow direction x is $\rho = \frac{N_k}{R_k}$. If N is the total number of Kuhn segments the relationship $\int_{x=0}^{L} \rho(x)dx = N$ has to be satisfied. By calculating the integral taking into account Equations (4.1), (4.2), (4.6) and (4.7) we can deduce the extension L of the chain with N segments at a particular velocity v. For $\nu \neq 1/2$ we have

$$L \propto N^{\frac{\nu}{2\nu-1}} v^{\frac{1-\nu}{2\nu-1}} , \tag{4.9}$$

which takes the following form under good solvent conditions ($\nu \approx 3/5$)

$$L \propto N^3 v^2 . \tag{4.10}$$

For a θ-solvent, $\nu = 1/2$ we have

$$L \propto \left(\frac{k_B T}{v\eta}\right)^{1/2} e^{\frac{\eta a^2 N v}{k_B T}} . \tag{4.11}$$

The extension of the chain at the direction y perpendicular to the flow direction x is found by $y = R_k$. Using Equations (4.1) and (4.8) we find that the profile of the deformed chain should be hyperbolic (for both good solvent and θ-solvent conditions)

$$y(x) \approx \frac{k_B T}{6\pi\eta v x} . \tag{4.12}$$

The size of the larger blob ($k = 1$) can be found by Equations (4.1) and (4.3) to be $R_1 \approx \frac{k_B T}{F_1} \Rightarrow R_1 \approx \frac{k_B T}{6\pi\eta v R_1} \Rightarrow R_1^2 \approx \frac{k_B T}{6\pi\eta v}$. At low velocities the deformation of the chain is small but if we require the larger blob to be smaller than the Flory radius $R_1 < R_F$ where $R_F \approx aN^\nu$, we deduce the velocity which initiates the trumpet regime (see Figure 4.4)

$$v_1^{\text{non}} \approx \frac{k_B T}{6\pi\eta a^2 N^{2\nu}} . \tag{4.13}$$

The smallest blob at the tethered end is found if we substitute the total force $F = 6\pi\eta v L$ into the Pincus relationship (Equation (4.1)) $R_m \approx \frac{k_B T}{6\pi\eta v L}$. In order for the trumpet regime to be valid, the size of this blob must exceed the size of the Kuhn segment $R_m > a$. This relationship determines the maximum velocity for the trumpet regime. Under good solvent conditions ($\nu \approx 3/5$)

$$v_2^{\text{non}} \approx N^{1/5} v_1^{\text{non}} . \tag{4.14}$$

At this velocity the chain enters the stem and flower regime. This regime holds until a velocity where the size of the larger blob also becomes equal to the Kuhn segment. Under good solvent conditions ($\nu \approx 3/5$)

$$v_3^{\text{non}} \approx \frac{k_B T}{6\pi\eta a^2} = N v_2^{\text{non}} . \tag{4.15}$$

Free-Draining Blob Model

In this model the solvent is assumed to freely-drain through the polymer chain (all hydrodynamic interactions between the different segments of the chain are neglected) and the friction/drag law is based on the Rouse-model where all N Kuhn segments individually contribute to the friction coefficient $\zeta_R = N\zeta_0$ where ζ_0 is the friction coefficient for a Kuhn segment.

For an ellipsoid (large axis a and small axis b) the Stokes law includes a logarithmic correction $F = \frac{4\pi\eta a v}{log(a/b)}$. The DNA Kuhn segment has a large aspect ratio ($a \approx 100$ nm

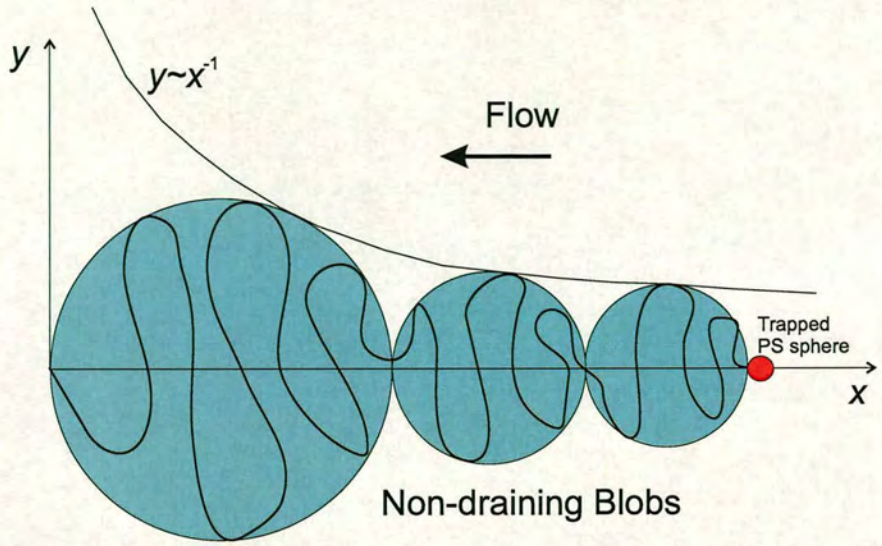

Figure 4.4: non-draining chain model at intermediate velocities: the polymer chain which is immobilised at one end (the polystyrene bead is not drawn to scale) is stretched under uniform flow breaking up into a string of non-draining blobs. The tension is non-uniform and it decreases towards the free end; subsequently the blobs are larger at the free end and the chain takes a trumpet shape.

and $b \approx 2$ nm) and the logarithm is at the range of 2. Thus, the effective hydrodynamic radius [92] of the DNA Kuhn segment is expected to be smaller than its linear size a. Here, for simplicity and in order to account for this effect we will neglect the numerical coefficient while keeping the length a for the hydrodynamic radius

$$F \approx \eta a v \,. \tag{4.16}$$

Thus, the *total force* acting on the k-th blob for the free-draining model is

$$F_k \approx \eta a v \sum_{j=1}^{k} N_j \,. \tag{4.17}$$

From Equations (4.1), (4.2) and (4.17) we can deduce an exact recursion relationship for the total force F_k exerted on the k-th blob

$$F_k - F_{k-1} \approx \eta a v \left(\frac{k_B T}{a F_k} \right)^{1/\nu} . \tag{4.18}$$

In the limit of large k values we can assume that k is a continuous parameter and therefore $F_k - F_{k-1} = \frac{dF(k)}{dk}$. Thus from Equation (4.18)

$$F(k) \approx (\eta a v k)^{\frac{\nu}{\nu+1}} \left(\frac{k_B T}{a}\right)^{\frac{1}{\nu+1}} . \tag{4.19}$$

Since $x_k = \sum_{j=1}^{k} R_j$, using Equations (4.1), (4.19) and substituting the sum with an integral we deduce

$$x(k) \approx 2 \left(\frac{k_B T}{\eta a v}\right)^{\frac{\nu}{\nu+1}} (ak)^{\frac{1}{\nu+1}} . \tag{4.20}$$

Eliminating k from Equations (4.19) and (4.20), we find that the drag force at position x is

$$F(x) \approx \frac{1}{a} (k_B T)^{1-\nu} (\eta a v x)^{\nu} . \tag{4.21}$$

The segment density $\rho(x)$ projected onto the flow direction x is $\rho = \frac{N_k}{R_k}$. If N is the total number of Kuhn segments the relationship $\int_{x=0}^{L} \rho(x) dx = N$ has to be satisfied. By calculating this integral taking into account Equations (4.1), (4.2), (4.19) and (4.20) we can deduce the extension L of the chain with N segments at a particular velocity v

$$L \propto N^{\frac{1}{\nu}} v^{\frac{1-\nu}{\nu}} . \tag{4.22}$$

Under θ-solvent conditions ($\nu = 1/2$)

$$L \propto N^2 v , \tag{4.23}$$

while, under good solvent conditions ($\nu \approx 3/5$)

$$L \propto N^{5/3} v^{2/3} . \tag{4.24}$$

The extension of the chain at the direction y perpendicular to the flow direction x is found by assuming $y = R_k$. Using Equations (4.1) and (4.21) we find that the profile of the deformed chain should be

$$y(x) \approx a \left(\frac{k_B T}{\eta a v}\right)^{\nu} x^{-\nu} . \tag{4.25}$$

Under θ-solvent conditions ($\nu = 1/2$)

$$y(x) \propto x^{-1/2}. \tag{4.26}$$

The free-draining condition stretches the chain more strongly and the profile is smoother (compare the Figures 4.4 and 4.5).

The trumpet regime (see Figure 4.5) is initiated at the velocity

$$v_1^{\text{free}} \approx \frac{k_B T}{\eta a^2 N^{\nu+1}}. \tag{4.27}$$

The trumpet regime holds until velocity

$$v_2^{\text{free}} \approx \frac{k_B T}{\eta a^2 N} = N^{\nu} v_1^{\text{free}}. \tag{4.28}$$

At this velocity the chain enters the stem and flower regime which holds until the velocity

$$v_3^{\text{free}} \approx \frac{k_B T}{\eta a^2} = N v_2^{\text{free}}. \tag{4.29}$$

A Partially Draining Blob Model: F-Shell Blob Model

Rzehak *et al.* [94] have shown by Brownian dynamics simulations that at higher velocities the flow penetrates the blobs resulting in a gradual transition from a nearly non-draining chain at low velocities to a nearly free-draining one at higher velocities. The flow penetrates partially the polymer coil and the polymer chain is neither totally non-draining nor totally free-draining.

To account for this behaviour within the framework of blobs they introduced a modified blob-model: the "free-draining shell", or F-shell, blob model [94, 95] which takes into account the important effect of the partial draining state of the polymer chain in a simplified fashion. In the partially draining blob model each blob contains a non-draining impenetrable inner core with variable diameter and a free-draining shell of constant thickness D (see Figure 4.6).

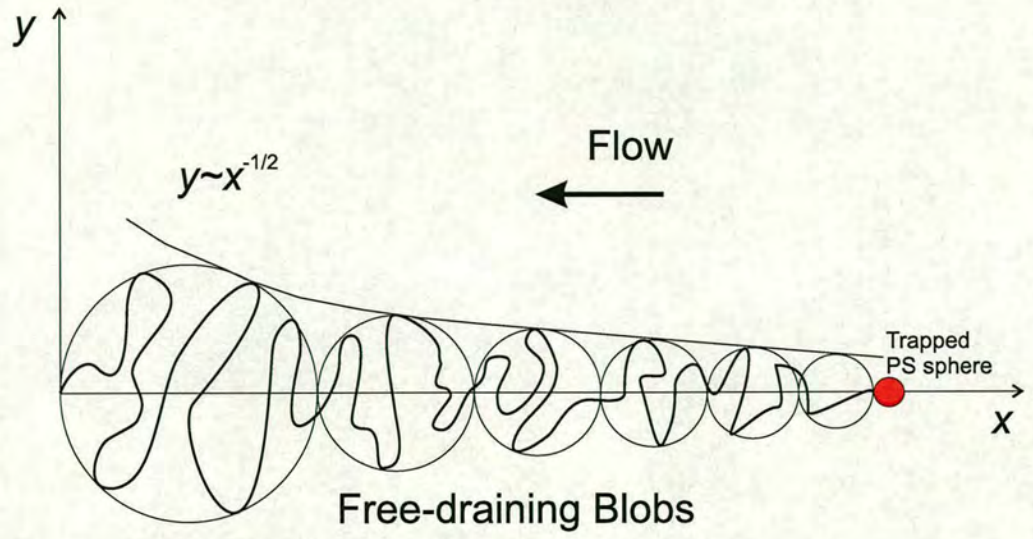

Figure 4.5: Free-draining chain model at intermediate velocities: the polymer chain which is immobilised at one end (the polystyrene bead is not drawn to scale) is stretched under uniform flow breaking up into a string of free-draining blobs. The tension is non-uniform and it decreases towards the free end; subsequently the blobs are larger at the free end and the chain takes a trumpet shape. The profile is smoother compared to the non-draining chain model (Figure 4.4).

At low velocities the majority of the segments lie within the inner impenetrable cores and the effect of the free-draining shell is minimal; the chain behaves effectively as non-draining. At higher velocities the chain is stretched, the number of blobs increases while their size decreases and gradually most segments lie within the free-draining shells; the chain behaves effectively as free-draining. At moderate velocities, the F-shell blob chain deformation is intermediate between the two extreme cases of non and free-draining blob models leading to intermediate behaviour [94, 95]. It has to be noted that despite the simplicity of the F-shell model, it can be solved only numerically [95]. The two previous models can be viewed as the two limits of the F-shell model: $D = 0$ corresponds to the non-draining model and $D = R_1$ corresponds to the free-draining model. By tuning the parameter D intermediate behaviour can be attained.

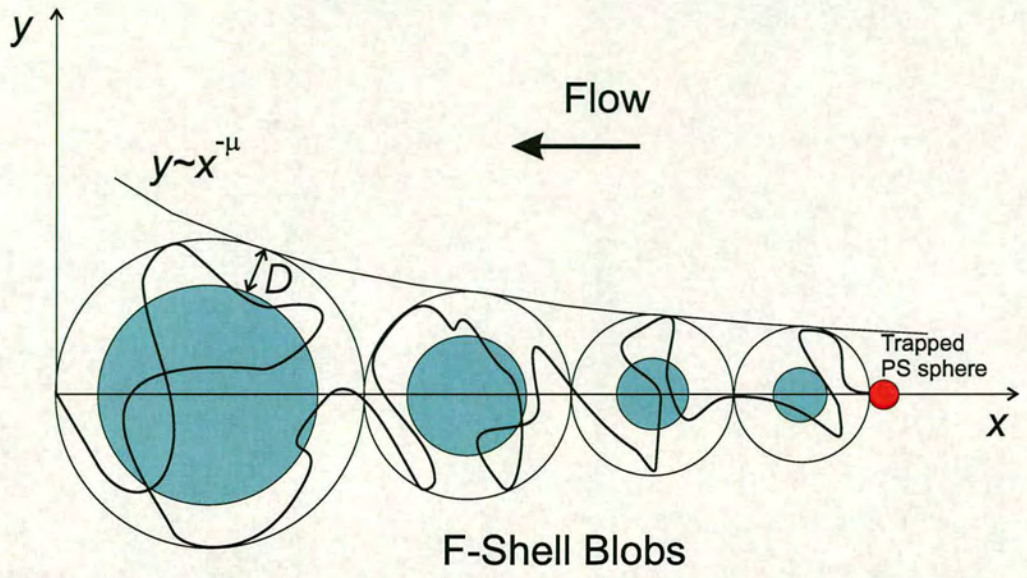

Figure 4.6: Partially-draining chain model at intermediate velocities: the polymer chain which is immobilised at one end (the polystyrene bead is not drawn to scale) is stretched under uniform flow breaking up into a string of partially-draining blobs. The blobs contain an inner non-draining core which is surrounded by a free-draining shell of constant thickness D.

Excluded-Volume Interactions

The excluded volume interaction in an athermal solvent of a non-spherical Kuhn segment is

$$v_c \approx a^2 d\,, \tag{4.30}$$

where a is the length of the Kuhn segment and d is its effective diameter. Its occupied volume is $v_0 \approx ad^2$.

The Flory theory of polymer solutions [89, 97] indicates that if

$$\frac{v_c}{a^3} N^{1/2} > 1 \Rightarrow \frac{d}{a} N^{1/2} > 1 \tag{4.31}$$

the excluded volume interactions are important and they should be taken into account.

4.3 Experiments

The experimental set up the preparation of the DNA-bead sample and the flow cell used have been described in the previous chapter. The buffer and DNA sample were kept separately in a light-sealed box full of ice. The cell was coated by a BSA liquid in order to inhibit the beads adhering to its walls and then rinsed with the same buffer used at the experiments. After that stage the lights were switched off and the experiment began.

Initially the cell was filled with the sample and a bead was trapped using brightfield illumination at a measured height of $\approx$ 9-10 μm from the lower surface of the cell. The imaging was then switched to fluorescence to check whether DNA was attached to the bead.

The cell was then moved with constant speed via an attachment to an Encoder Driver Linear Actuator (COHERENT) which was controlled by a LabView programme; the minimum speed of the actuator was 0.5 μm/s with a resolution of 0.02 μm/s. The movement of the cell was stable within the range of velocities applied: 3 μm/s to 200 μm/s.

The movies were recorded with a CCD camera (LaVision, Imager3) having a linear response detector, with t = 1000 ms exposure time. At low flow rates movies could last several minutes while at the higher rates the duration was much shorter due to the larger displacement of the bead along the cell which resulted in the loss of the focus and the frequent escape of particles from the trap. The length of the DNA molecule under different flows was measured with the same software used for imaging (DaVis).

4.4 Results

Figure 4.7 shows a typical fluorescence image of a DNA molecule held fixed at one end while deformed by a uniform flow.

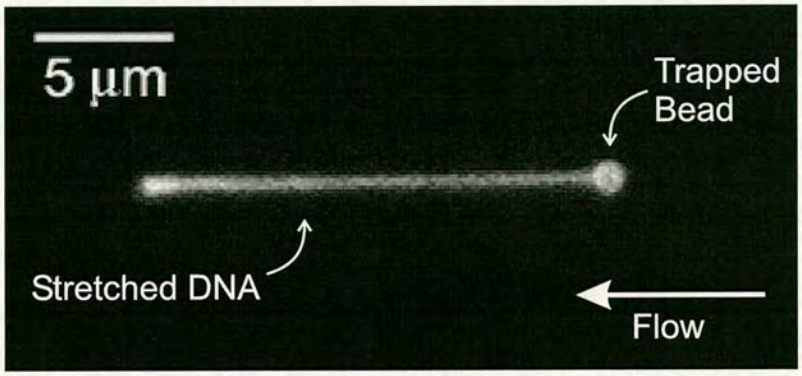

Figure 4.7: DNA deformation under flow. The flow velocity is 50 μm/s.

Figure 4.8 shows typical fluorescence images of a DNA molecule held fixed at one end while deformed by a uniform flow at different flow velocities. Increasing the flow velocity results in polymer elongation.

Figure 4.9 presents the increase of the DNA length with the flow velocity in a log-log plot. The elongation does not follow a power low and the slope decreases at higher velocities suggesting the existence of an asymptotic plateau at higher velocities.

The size of the DNA perpendicular to the flow (width) appears to decrease. This is illustrated in Figure 4.10 where the maximum width (at the free end) and the minimum width (at the fixed end) at a particular velocity is plotted versus the flow velocity. In both cases the slope decreases at higher velocities and the fixed end width attains a plateau of about 0.43 μm at $\approx$ 50 μm/s while the free end width continues to decrease as seen in the figure. Thus, the DNA chain gets longer and thinner with increasing flow velocity. To illustrate the change in the DNA conformation the outer contour shape of the DNA coil was extracted from the images. In Figure 4.11 the DNA contour profiles

at two specific velocities are presented. The profile at the low velocity is reminiscent of a trumpet-like shape while at higher velocities the profile near the fixed end is nearly horizontal with a characteristic protrusion at the free end which is reminiscent to the stem/flower shape.

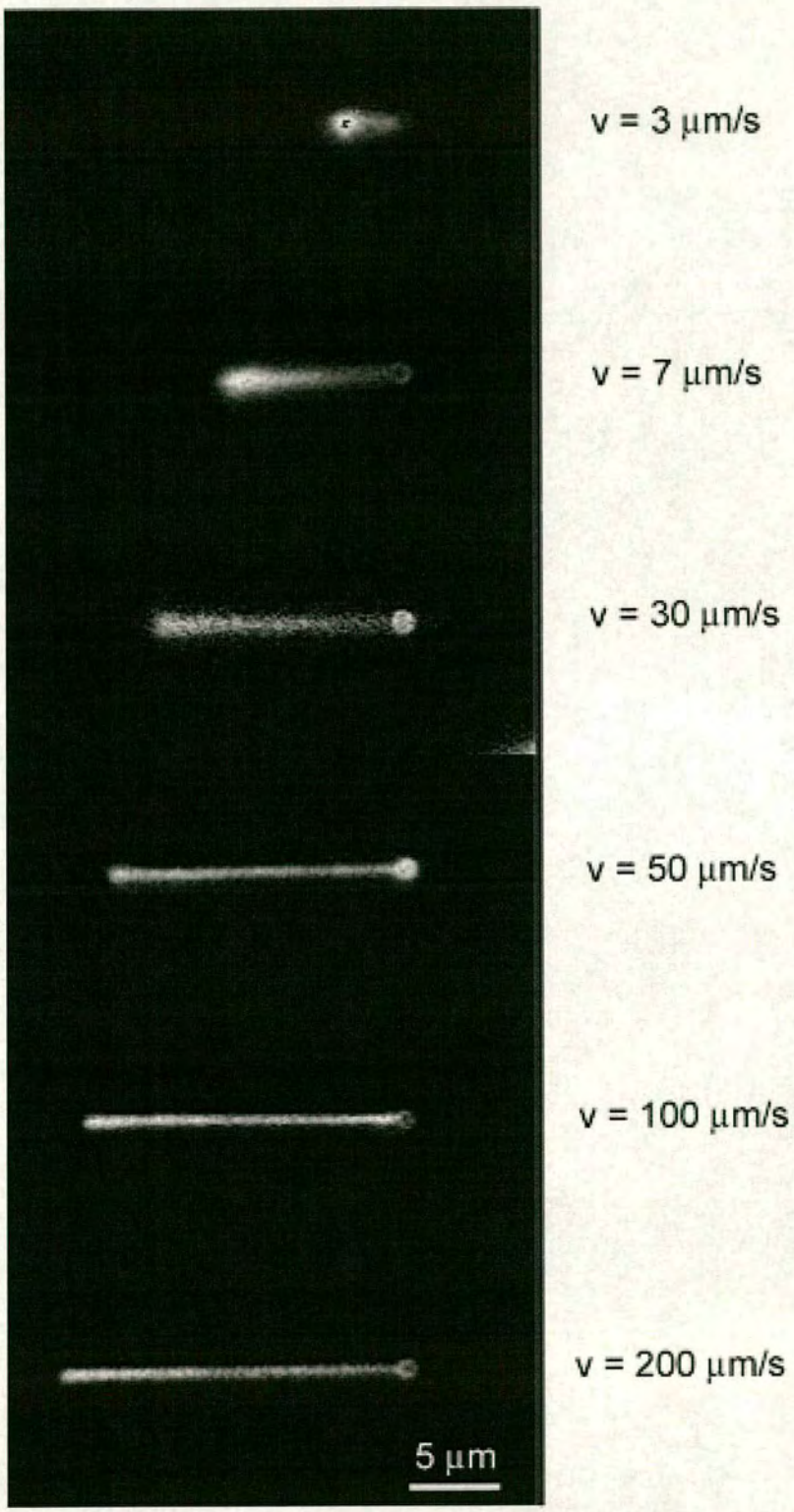

Figure 4.8: DNA deformation under flow at different velocities. flow direction is towards left.

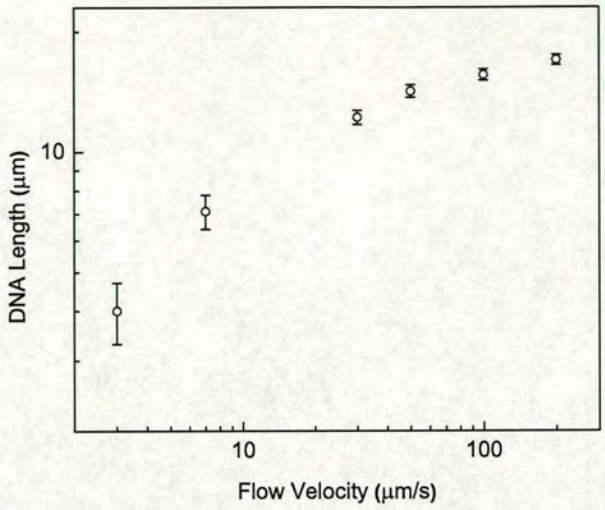

Figure 4.9: DNA length plotted versus the flow velocity.

In order to investigate quantitatively the DNA contour shape and compare it with the blob-model scaling predictions, we extracted DNA contour profiles by processing tens of fluorescence images at different velocities. We used MatLab to take a series of profiles of different intensity levels and we selected the intensity profile which shows a clear cross section of the DNA shape and it is as close as possible to the noise level (but above it). We performed a fitting procedure in order to obtain the value of the exponents associated with the perpendicular to the flow chain extension (its shape).

In fitting power laws to the shape data, it is important to take into account the fluorescent blurring effect (illustrated in a schematic drawing in Figure 4.12). Due to this effect, both the DNA width and the length are overestimated. The DNA coil appears larger than it is in all directions. For example, Yoshikawa *et al.* [98, 99] comparing the hydrodynamic and the fluorescent radius of unperturbed DNA coils in solution calculated the blurring effect to be 0.3 μm. Perkins *et al.* [75] has measured the 2σ width

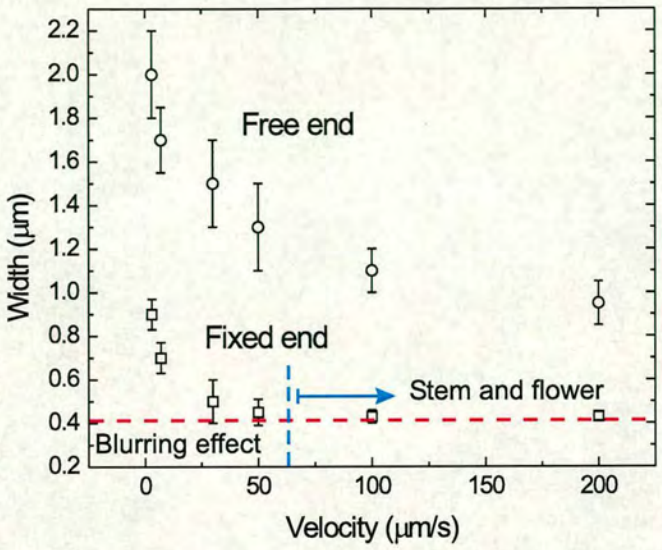

Figure 4.10: Width at the free and and at the fixed end plotted versus the flow velocity.

of a highly extended DNA double strand to be about 0.4 μm which indicates a similar blurring effect (the DNA diameter is about 2 nm). In order to account for this effect we used the following fitting function:

$$y - y_0 = A(x - x_0)^{-\mu} \tag{4.32}$$

which contains four independent fitting parameters. The parameter y_0 is associated with the overestimation of the DNA width and the parameter x_0 is associated with the overestimation of the DNA length. The fitting process using four independent parameters gave unreasonable values for x_0 and y_0. However, Figure 4.10 shows that the fixed end width of the DNA takes a constant value of ≈ 0.4 μm when it is fully stretched. Since the DNA diameter is about 2 nm, we deduce that the half-width of the blurring effect is 0.2 μm (this is the half-width of the "stem" at high flow velocities). The values of μ presented here were obtained by a 2-parameter fitting procedure by

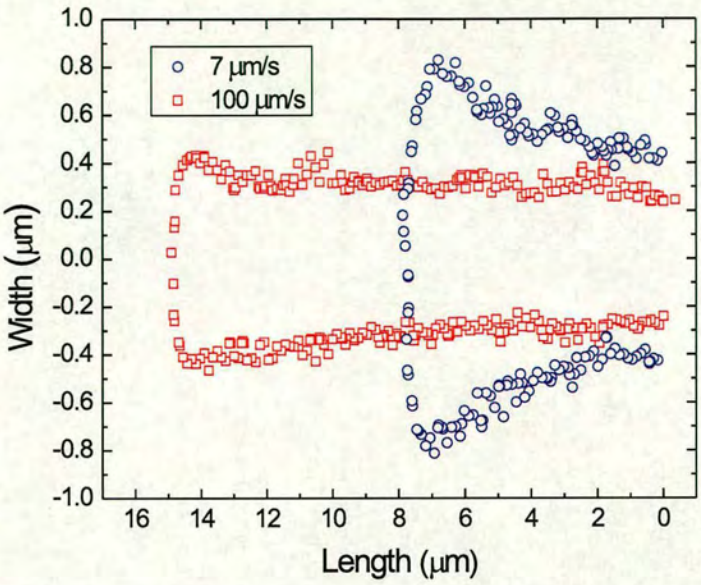

Figure 4.11: Contour shapes of DNA at different velocities. Flow direction is towards left. The two intermediate deformation regimes are clearly shown: trumpet shape at low velocities and stem and flower shape at high velocities.

taking that $x_0 = y_0 = 0.2\ \mu$m.

Figures 4.13 to 4.18 show some typical profiles at different velocities and the fitting results. The value of the exponent μ changes with the flow velocity from a value close to 1 until it reaches a plateau of 0.3 at higher velocities as it can be seen in Figure 4.19 where μ is plotted versus the flow velocity.

4.5 Discussion

The length vs flow velocity relationship was the main focus of several previous experimental and theoretical studies (e.g. [75, 91]) As it can be seen in Figure 4.9 and

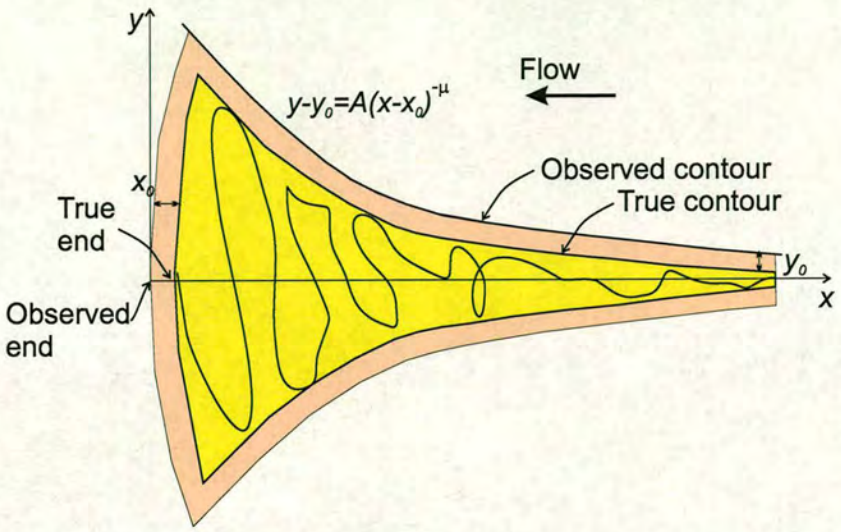

Figure 4.12: DNA profile and blurring effect due to fluorescence imaging.

in agreement with the previous studies the length dependence on velocity cannot be described by a simple power law as predicted by the non and free-draining models. There are several reasons for this behaviour: the finite length (relatively small number of Kuhn segments) and the finite extensibility of the DNA chain leads to an upper limit / asymptotic plateau in the chain elongation; it is not certain that the DNA chain behaves in a non-draining or free-draining manner at all flow velocities; furthermore, it is possible that different parts of the chain are in different draining regimes even at low and moderate velocities[5]. The significance of excluded volume interactions is unknown and even more crucially it might be different for different parts of the chain and it could vary with the velocity.

The DNA effective diameter d is about 2 nm and the Kuhn segment is $a \gtrsim 100$ nm (The binding of the fluorescent die is expected to stiffen DNA and increase the persistence length). The DNA used has a contour length of ≈ 16.5 μm which indicates

[5]At higher velocities where we are well in the stem/flower regime, by definition the stem is free-draining while the flower can be non-draining.

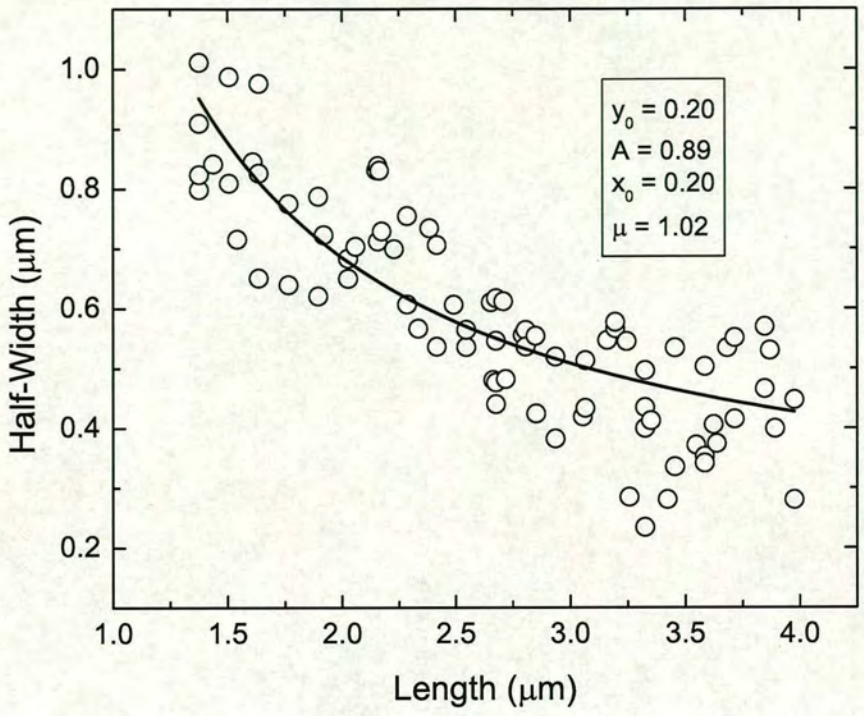

Figure 4.13: DNA Shape at a velocity of 3 μm/s.

that $N = 165$ Kuhn segments. For these values (Equation (4.31)) $\frac{d}{a}N^{1/2} \approx 0.65$, which is smaller than but quite close to 1. Bearing in mind that the calculation is approximate one can cautiously deduce that for the unperturbed chain one should take into account the excluded volume interactions. However, we would expect that at even low velocities, where the chain extends a few times its unperturbed size and the monomer concentration is reduced, the excluded volume effects are suppressed and the chain can be considered ideal [90] .

The profiles of the DNA shape can be fitted by a power law. The shape exponent μ takes a value close to 1 at low velocities (3 μm/s) (Figure 4.19) which is consistent with the value of the exponent predicted by the non-draining blob model (Equation

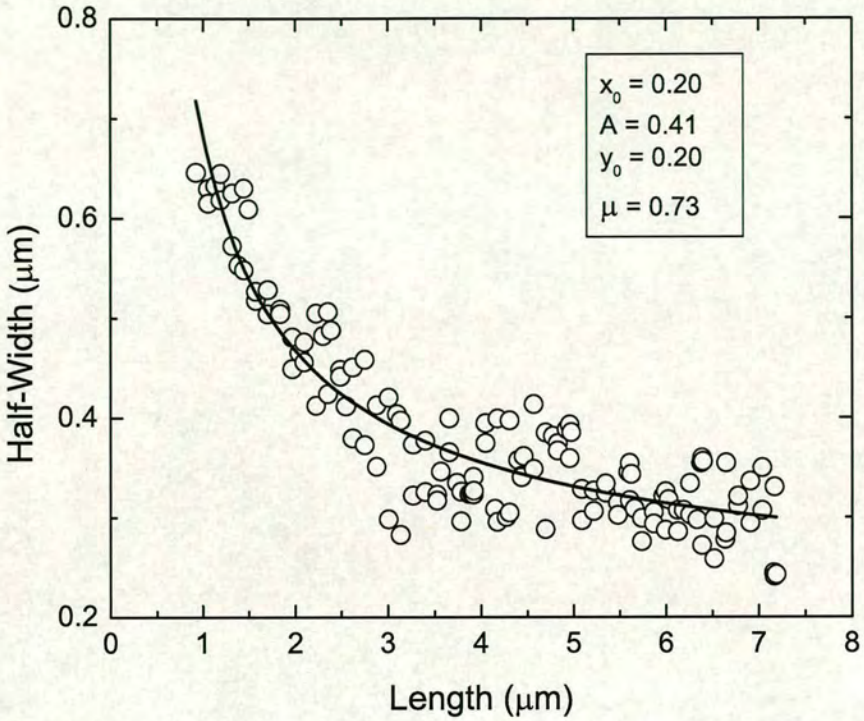

Figure 4.14: DNA Shape at a velocity of 7 μm/s.

(4.12)). The exponent is the same for both good and θ-solvent conditions (see also Table 4.1), so that we cannot distinguish between them and evaluate the excluded volume interaction significance. At moderate velocities (7, 30 and 50 μm/s) the exponent changes taking lower values between 0.85 and 0.45. This behaviour could be due to a combination of two effects (i) the gradual transition from non-draining to free-draining conditions, (ii) the gradual suppression of excluded volume interactions (for the free-draining chain $\mu \approx 0.6$ for good solvent conditions and 0.5 for an ideal chain (Equation (4.25)). However, since the excluded volume interactions are likely to be already fully suppressed even at low velocities (see calculation above), the *gradual transition from non-draining to free-draining conditions* is the most probable explanation.

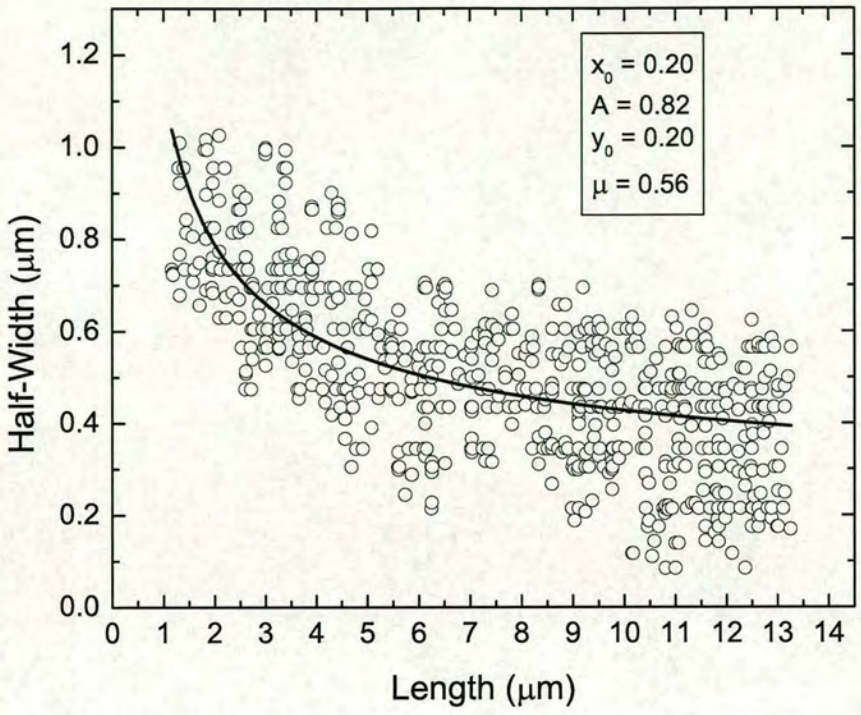

Figure 4.15: DNA Shape at a velocity of 30 μm/s.

These results are consistent with simulations by Rzehak *et al.* [94] who showed by using Brownian dynamics simulations that the flow can penetrate the blobs. As the blobs decrease in size at higher velocities more and more segments pass from a non-draining state to a free-draining one resulting in a gradual transition from a nearly non-draining chain at low velocities to a nearly free-draining one at higher velocities. Consequently, a modified blob-model such as the F-shell blob model [94, 95] which takes into account this important effect of the partial draining behaviour appears promising in explaining the single polymer chain deformation at uniform flow.

The fact that the width at the tethered end reaches a plateau signifies the initiation of the stem and flower regime. Figure 4.10 indicates that the stem and flower regime

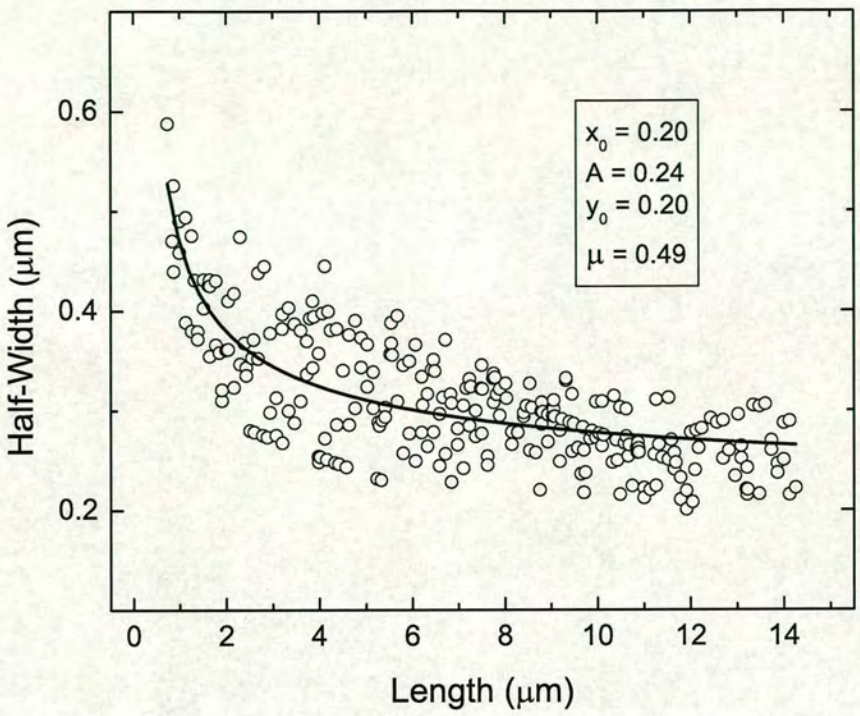

Figure 4.16: DNA Shape at a velocity of 50 μm/s.

is reached at a velocity in the range of 50 μm/s. However, Figures 4.17, 4.18 show that there is a small but finite slope at the stem part of the chain (the profile is not completely horizontal) indicating that the stem and flower shape is an approximate one. In addition, we observe that the flower width at the free end continues to decrease and has not reached a plateau at 200 μm/s indicating that the total stretching regime (4th regime) has not been attained yet. The values of the shape exponent at higher velocities (100 and 200 μm/s) probably have no scaling significance: The reduced width along a major part of the chain indicates that the number of Kuhn segments per blob tends towards 1. In addition, the scalable part of the chain is now restricted only to the flower which occupies a relatively small part of the chain and contains only a

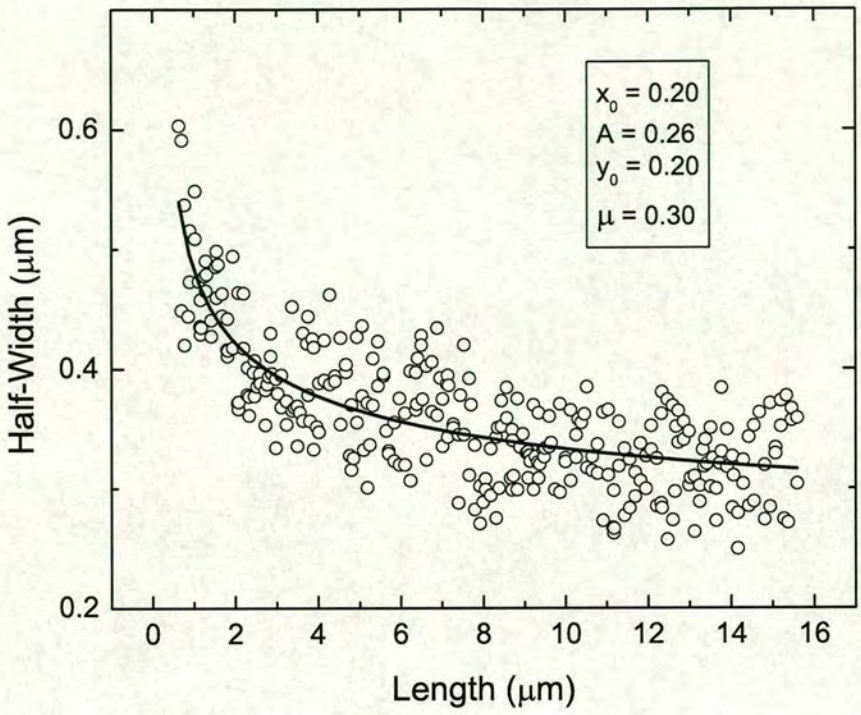

Figure 4.17: DNA Shape at a velocity of 100 μm/s.

few blobs making the application of scaling relationships questionable.

Using the equations for the limiting velocities for the two intermediate regimes, we find that the trumpet regime for non-draining blobs is predicted to start at $v_1 \approx 0.2$ μm/s and end at $v_2 \approx 0.6$ μm/s where the stem and flower regime starts; the latter ends at $v_3 \approx 100$ μm/s. For the free-draining chain we deduce (both solvent conditions give similar results): $v_1 \approx 0.2$ μm/s, $v_2 \approx 2.5$ μm/s and $v_3 \approx 330$ μm/s. These values do not agree with the observations. However, one should note that calculating absolute values (instead of characteristic exponents) from scaling theories is not at all accurate. Scaling relationships neglect several constants of order unity. Brochard-Wyart [80, 81, 82] does not use the constant 6π in the Stokes law for the non-draining blob model. In this case:

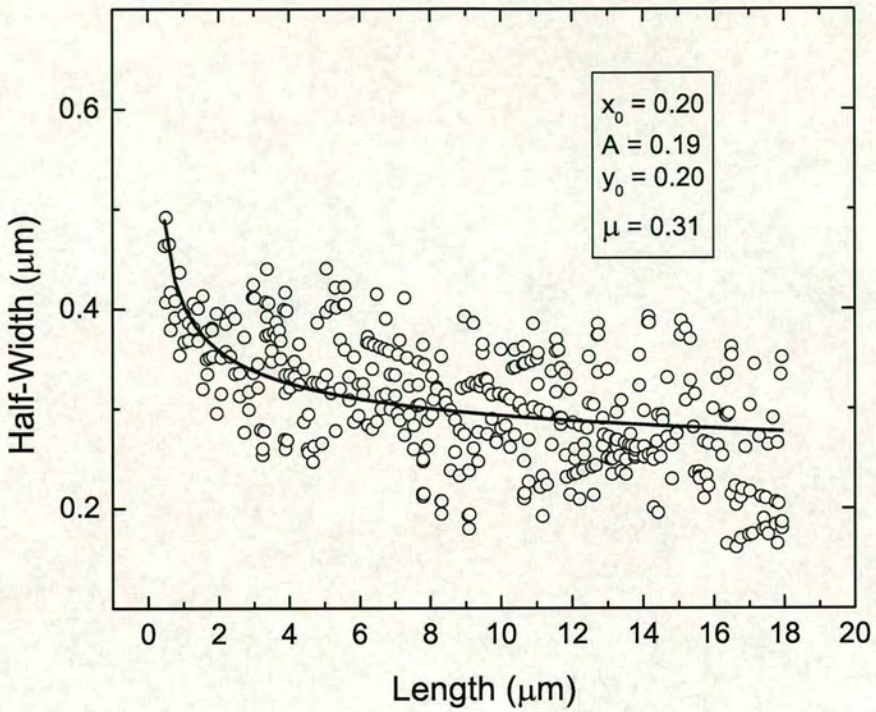

Figure 4.18: DNA Shape at a velocity of 200 μm/s.

$v_1 \approx 2$ μm/s, $v_2 \approx 6$ μm/s and $v_3 \approx 1000$ μm/s. The non-draining blob model predicts a very limited range of velocities for the trumpet regime (Equation (4.14)). In contrast, the velocity range for the trumpet regime is wider for the free-draining blob model (Equation (4.28)). This is consistent with our observations where we find a relatively wide range of velocities for the trumpet shape (≈ 3 μm/s to ≈ 50 μm/s) and shape exponents which indicate a gradual passing into a free-draining state.

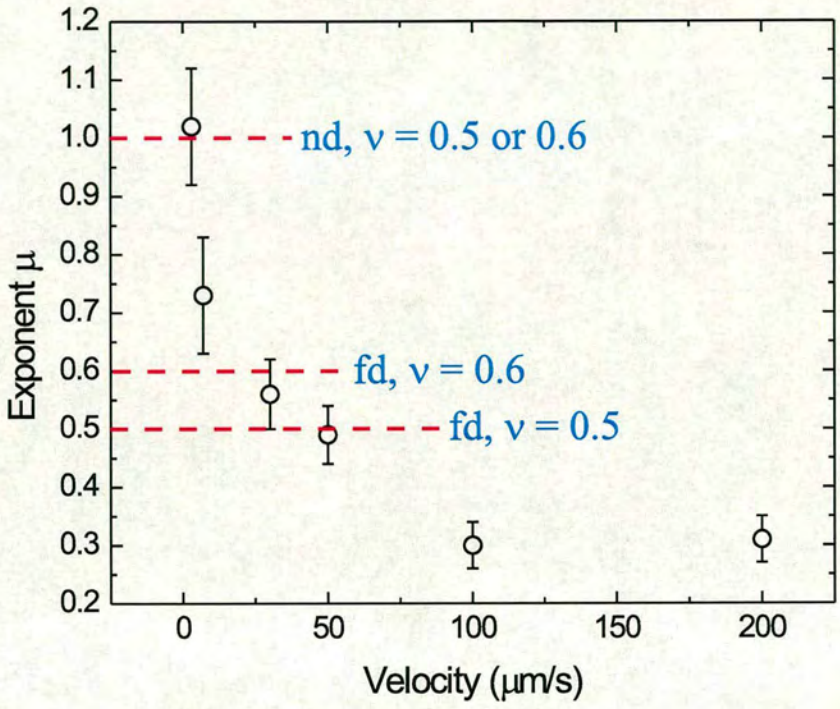

Figure 4.19: exponent μ plotted versus the flow velocity.

Model		μ
fd	$\nu = 0.5$	$\mu = 0.5$
	$\nu = 0.6$	$\mu = 0.6$
nd	$\nu = 0.5$	$\mu = 1$
	$\nu = 0.6$	$\mu = 1$

Table 4.1: Shape exponents μ for the free-draining (fd) and the non-draining (nd) model.

4.6 Conclusions

The deformation of a DNA chain fixed at one end under uniform flow was directly investigated using single chain fluorescence imaging and optical trapping. The results were discussed within the scaling theory framework of the non-draining and free-draining blob-models. While the blob-model predictions for the DNA elongation and the limits of the different shape regimes were not verified by the observations, the DNA contour shape was successfully fitted by power laws and the calculated characteristic exponents indicate that the chain undergoes a gradual transition from a non-draining state to a free-draining one within the trumpet regime. These observations indicate the importance of the F-shell blob model and demonstrate that single chain fluorescence imaging combined with analysis from simple scaling theory can provide useful insights into the behaviour of polymer chains under flow.

Chapter 5

DNA Condensation

5.1 Introduction

The kinetic process of the initiation of DNA condensation induced by spermidine was studied by single molecule fluorescence imaging in combination with optical tweezers and a laminar flow cell. The DNA molecule was attached by one end to a colloidal particle which was held stationary within the flow cell by an optical trap. The DNA was stretched under the flow and it was then moved to a condensing agent (spermidine) rich area where it was observed to rapidly contract slightly but remained stretched for a considerable period of time (a few to $\approx$ 30 s depending on the flow rate of $\approx$ 50 to 250 μm/s) in the presence of spermidine before it collapsed abruptly (typically $\lesssim$ 100 ms). The lag or latency time, τ_l (i.e. the time needed for the start of collapse of hydrodynamically stretched DNA after the DNA entered the condensing agent zone) increased with the increase of flow rate, the ionic strength and DNA contour length. The effect is reversible, but consecutive re-entries to the spermidine region led to a decrease in latency times. The results indicate the extreme sensitivity of the collapse initiation on the competitition of cations for DNA binding sites and the weakened spermidine affinity for binding when the DNA chain is under tension.

5.2 Background

The DNA condensation from a disordered, coiled state to an orderly compact state is accompanied by a spectacular decrease of the volume occupied by the DNA molecule [100]. The phenomenon is used in viruses, bacteria and eukariotic cells to pack their genomic DNA in confined spaces. For example, in the case of T4 phage DNA the 1-dimensional compression ratio inside the virus capsid is more than 500 [101]. It is believed that the transition plays an important role on the DNA self-regulation and expression. Furthermore, renewed interest for compacted DNA has been generated by the need to develop effective methods of gene delivery for therapy. A reversible and easy to implement method of compacting the DNA without causing any structural damage can play an important role in gene therapy.

Condensation can be induced by polyamines [102], inorganic multications [103], cationic polypeptides [104], basic proteins [105], alcohols [106] and neutral crowding polymers [107]. Furthermore, it can be influenced dramatically by polymer concentration [98], salt concentration [108], pH [109] and solvent effects [101].

Early light scattering studies of condensation in dilute DNA solutions have shown that the transition is steep but continuous [106, 110]. These and other studies using conventional techniques such as viscosimetry, sedimentation etc. [107, 111], probe a large number of DNA molecules and all results are averaged over the statistical ensemble of many molecules. In this way, the equilibrium properties (such as the initial and final radius of gyration) can be determined but they are not suitable for evaluating the kinetics since not all DNA chains are expected to start collapse simultaneously. Furthermore using an ensemble of DNA molecules the condensation process of individual DNA molecules can be obscured by the aggregation and precipitation processes which happen in parallel.

However, recent single molecule fluorescence imaging (SFI) techniques [51, 50] probe individual molecules and have clearly demonstrated that for a single DNA molecule

the condensation is a discontinuous, "all-or-none" transition [103, 112].

Biomolecules are too small to be visible using conventional optical microscopes. However, if the biomolecules are tagged with fluophores, visualisation is possible using fluorescence microscopy and subsequently individual biomolecules can be directly studied. Furthermore, combining SFI with optical tweezers provides the opportunity to micromanipulate individual molecules and expose them with unprecedented control in various environments. Brewer *et al.* [113] used SFI, optical trapping and a dual-port flow cell to study directly the condensation kinetics of individual DNA chains induced by protamine. It was found that the DNA molecule collapsed with a nearly constant speed from its free end. A study of DNA-chromatin assembly by Ladoux *et al.* [114] revealed that the assembly proceeds with at least three steps with DNA wrapping as the final step.

Much effort has been concentrated on (i) measuring the dimensions and shapes of condensed DNA mainly by scanning electron microscopy (SEM); they were found to be toroids and rods [115, 116, 117]; (ii) measuring the minimum concentrations (critical concentrations) of different condensing agents which are sufficient to induce condensation [118, 108].

Yoshikawa's group has pioneered the use of SFI to study the thermodynamic aspects of the DNA condensation. They have shown that the DNA collapse is a proper first order transition with the DNA being metastable near the critical concentration [119] [1]. Furthermore, the collapse occurs via the classical process of "nucleation and growth" i.e. similar to the formation of a crystal/condensed phase from a metastable and supersaturated fluid [120]. These experiments and further simulations studies [121, 122] have shown that the condensation nucleus occurs mainly at the DNA ends and then proceeds along the DNA backbone; furthermore, the nucleus need not involve many

[1] This metastable regime which results in a mixed population of both coiled and collapsed chains is the reason for the continuous appearance of the transition using the traditional techniques of light scattering, UV spectroscopy, viscosimetry, sentimentation etc.

Kuhn segments.

Theoretical and simulation studies of semiflexible chain condensation have been concentrated mainly on the kinetics of the process *after* nucleation [123] and on intermediate structures during condensation [124]. Kikuchi *et al.* [125] showed that in the absence of hydrodynamic interactions the collapse is starting at the free ends of the chain while in the presence of hydrodynamic interactions the collapse is uniform across the chain and more rapid.

Porschke [126] employed stopped-flow and field-jump experiments combined with equilibrium titration and light scattering detection to study the dynamics of DNA condensation. Although his data on the the actual collapse are obscured by the above mentioned asynchronous behaviour of the DNA molecules, he clearly observed a short "induction" period ($\lesssim$ 20 ms) before condensation by spermine. He argued that there is a threshold amount of condensing agents which have to bind on the DNA before condensation occurs and excluded-volume interactions between the bound and free condensing agent molecules during the final stages of the binding process can result in delayed kinetics.

In this chapter, we present a systematic experimental study of the nucleation kinetics of DNA condensation of a 48,000 λ-phage DNA and a 24,000 base fragment using spermidine as the condensing agent under different flow speeds and salt concentrations.

5.2.1 DNA as a Random Coil: a Worm-Like Chain

A DNA molecule can be approximated by a thin, elastic, homogeneous rod where the elastic constants are such that small thermal fluctuations produce random, isotropic bending of the chain sections resulting in a random coil for sufficiently long chains [86]. This is a quite general model of a semi-flexible polymer chain called persistent or worm-like chain WLC and accounts for both local chain stiffness and long-range

flexibility. This model is compatible with the particular mechanism of DNA chain flexibility[2]. The persistence length ℓ_p is a characteristic of polymer flexibility and determines the maximum length of a chain section which can be considered as a straight line. Beyond this length the thermal fluctuations result in random bendings and directional correlations are lost. Since directional correlations extend in two directions along the backbone, it is not a surprise that the effective Kuhn segment can be proven to be twice as long as the persistence length.

Applying macroscopic elasticity theory one can calculate the elastic bending energy for a length s of a DNA part

$$\Delta E_{bending} = \frac{\kappa s}{2R_c^2} , \tag{5.1}$$

where κ is the bending stiffness and R_c is the radius of curvature of this part of DNA.

The bending stiffness is connected with the Young's modulus E: $\kappa = EM$, where M is the area moment of inertia which for a rod with a radius r is $M = \pi r^4/4$.

The bending stiffness is connected with the persistence length with the following relationship

$$\kappa = \ell_p k_{\mathrm{B}} T , \tag{5.2}$$

where k_{B} is the Boltzmann constant and T is the absolute temperature.

If a stretching force F exerted on a WLC chain of a contour length L_0 results in an extension x, the $F - x$ relationship is given by the following approximate formula [87, 90]

$$F = \frac{k_B T}{\ell_p} \left[\frac{1}{4\left(1 - \frac{x}{L_0}\right)^2} - \frac{1}{4} + \frac{x}{L_0} \right] , \tag{5.3}$$

This relation takes into account *only entropic contributions* and ignores the chain extensibility at high enough stretching forces. The corrected equation for extensions near

[2]The mechanisms of polymer chain flexibility can vary. It is worthwhile noting that the flexibility of most synthetic polymers is due to the rotational-isomeric mechanism and are better described with the freely-jointed chain (FJC) model.

the full length takes the following form [127]

$$\frac{x}{L_0} = 1 - \frac{1}{2}\left(\frac{k_B T}{F\ell_p}\right)^{1/2} + \frac{F}{K}\,, \tag{5.4}$$

where K is the stretch modulus and is connected with the Young's modulus: $E = K/\pi r^2$ and the bending stiffness: $\kappa = Kr^2/4$.

5.2.2 DNA Condensation: a Coil-globule Phase Transition

A DNA double helix under specific solvent conditions collapses into a dense globule. Lifshitz, Grosberg and co-workers developed the statistical mechanics theory of a generic polymer coil-globule transition [128], while Post and Zimm were the first to study the condensation of a single DNA molecule [129] using the Flory-Huggins theory of polymer solutions taking into account the third virial coefficient (in addition to the second one) since in the condensed phase the number of triple collisions is not negligible. The free energy ΔG_s of a single chain in solution is

$$\frac{\Delta G_s}{k_B T} = N\left[(\chi - 1) + \frac{B\omega}{2^{3/2}\alpha^3} + \frac{C\omega^2}{2\cdot 3^{5/2}\alpha^6} + \frac{3}{2}(\alpha^2 - 1) - \ln\alpha^3\right]\,, \tag{5.5}$$

where N is the polymerization index, α is the swelling coefficient giving the ratio of the polymer radius of gyration to that in θ-conditions (α in the condensed state $\ll 1$), χ is the parameter of the interaction energy difference of like and unlike species ($\chi = \frac{z\Delta\epsilon}{k_B T}$, z is the number of neighbours), B and C are the second and third virial coefficients connected to χ as follows

$$B = \frac{1}{2} - \chi\,, \tag{5.6}$$

$$C = 1 + 12\frac{\chi^2}{z} - 16\frac{\chi^3}{z^2}\,, \tag{5.7}$$

The parameter ω is defined as

$$\omega = \left(\frac{9}{\pi\langle R_o^2\rangle}\right)^{\frac{3}{2}} V_p\,, \tag{5.8}$$

where $\langle R_o^2 \rangle$ is the mean-square end-to-end distance in the unperturbed state, and V_p is the molecular volume of the polymer. When χ is $> \frac{1}{2}$, the stronger polymer-polymer attractions induce the polymer to collapse into a dense globule.

A general conclusion of the theory [128] is that for flexible chains the transition is continuous while for stiff polymers such as DNA the transition is discontinuous. For both flexible and stiff chains the coiled (swollen) state is characterised by (i) low polymer concentration and (ii) fluctuations comparable to the size of the swollen chain. The globular (condensed) state for flexible chains is characterised by (i) high density and (ii) small fluctuations compared to the size of the globule; i.e. the condensed state of a flexible chain has an amorphous structure and liquid-like behaviour [86]. However, for stiff chains the collapsed state can be compared with a "crystalline" state [120]. The toroid or rod shape of the condensed DNA state can be considered as a small crystal [112].

The free energy per base pair (bp) can be estimated to be in the range of 0.1 and 0.01 $k_B T$ [101]. This small value per bp implies that to achieve condensation many DNA base pairs must change together as a unit and consequently DNA condensation is a very highly cooperative effect.

5.2.3 The Role of Charges

DNA is a negatively charged strong polyelectrolyte. Polyelectrolytes dissociate in solution forming charges along the chain and small counterions. A consistent way of describing the electrolyte-counterions system is the nonlinear Poisson-Boltzmann equation. The linear version of this equation (if the electrostatic potential is relatively weak) reduces to the Debye-Hückel equation which leads to potential V solutions of the form

$$V(r) = \frac{4k_{\mathrm{B}}T}{Zq_e} \exp\left(\frac{-r}{r_D}\right), \tag{5.9}$$

where r is the distance, q_e is the elementary charge unit, Z the valence and r_D the Debye length. This solution shows that the effect of counterions is to screen the electrostatic interaction. The screening is determined by the Debye length

$$r_D = \left(\frac{\epsilon_\mathrm{r} \epsilon_\mathrm{o} k_\mathrm{B} T}{2 I {q_e}^2} \right)^{1/2} , \tag{5.10}$$

where ϵ_r is the dielectric constant, ϵ_o is the vacuum permittivity and I is the ionic strength (IS).

For strong polyelectrolytes (high density of charges along the chain) such as DNA a fraction of counterions stay close to the chain partially neutralising it. This phenomenon is called counterion condensation [130] (not to be confused with the DNA condensation) [3] and can be predicted only by the non-linear Poisson-Boltzmann equation.

The electrostatic repulsion between the charges along the backbone results in a stiffening of the chain and to an increase in the persistence length. The additional electrostatic persistence length is

$$\ell_e = \frac{1}{4} \frac{{q_e}^2}{4\pi \epsilon_\mathrm{r} \epsilon_\mathrm{o} k_\mathrm{B} T} \left(\frac{r_D}{b} \right)^2 , \tag{5.11}$$

where b is the linear charge spacing and $\frac{q_e^2}{4\pi\epsilon_\mathrm{r}\epsilon_\mathrm{o} k_B T}$ is defined as the Bjerrum length. DNA is a strong electrolyte and the electrostatic repulsions (screened to some extent from the counterions) have to be neutralised for DNA to collapse. This can be achieved by using multications (over 3+) such as spermidine. Unications and dications are unable to induce condensation.

If two cations with different valences exist in the solution, there will be a competition for binding on the DNA phosphate sites. The theory which governs this competitive counterion condensation of two cations has been worked out by Manning [130] and used by Wilson with several condensing agents and salts in a variety of combinations [106]. Z is the valence, C the concentration, V the molar volume (surrounding the

[3] We use the term "binding" to refer to this counterion condensation.

DNA) within which the cations are bound and θ the fraction of DNA phosphate binding sites occupied. If we denote with the subsripts 1 and 2 the two cations, the equations which describe the binding are:

$$1 + \ln \frac{10^3 \theta_1}{C_1 V_1} = -2Z_1 \xi (1 - Z_1\theta_1 - Z_2\theta_2) \ln(1 - e^{-\frac{b}{r_D}}) \,, \tag{5.12}$$

$$\ln \frac{\theta_2}{C_2} = \ln \frac{V_2}{10^3 e} + \frac{Z_2}{Z_1} \ln \frac{10^3 \theta_1 e}{C_1 V_1} \,, \tag{5.13}$$

where the molar binding volume is

$$V(z) = 4\pi e N_A (1 + Z) \left(\xi - \frac{1}{Z} \right) b^3 \,. \tag{5.14}$$

The ξ is the counterion condensation parameter and is equal to the ratio of average linear charge spacing b to Bjerrum length. The total fraction of the neutralized DNA phosphate charges is

$$r = Z_1\theta_1 + Z_2\theta_2 \,. \tag{5.15}$$

Using these equations, Wilson and Bloomfield [106] showed that under different solution conditions and condensing agents a decrease in charge density of $\approx 90\%$ is enough for condensation to occur [106]. They also found that increasing the salt concentration results in an increase in the minimum multication concentration necessary to induce collapse.

5.2.4 What is the Exact Mechanism of the DNA Collapse?

We still lack the fundamental understanding of the exact reason for the DNA collapse by multivalent cations. Although the DNA has to be neutralised by about 90 % in order to achieve condensation, the remaining 10 % is enough to retain a sufficiently high repulsive force to resist collapse. One possible explanation can be induced dipole interactions due to fluctuating ion clouds around the DNA [131, 132]. These forces are conceptually similar to London dispersion forces but instead of fluctuating electron

clouds the ion fluctuations are considered. However, an alternative explanation is the hydration forces [101], i.e. attractive forces between the DNA strands arising due to the restructuring of the water around the DNA because of the multivalent cations presence. In addition, it is believed that the multivalent cations create a bridging effect between different DNA segments stabilising the compacted structure [110, 101].

5.2.5 Local Distortions

The counterion condensation theory assumes that the counterions reside on the DNA strand but they are not adsorbed on specific sites and can move freely along the chain. However, there is crucial experimental and theoretical evidence that the multivalent cations which induce the DNA condensation can locally distort the DNA strand and affect its stiffness. Drew *et al.* [133] studied DNA crystals and found that spermine occupies the major groove in the DNA structure; this groove is associated with local distortion in the DNA structure. This claim is supported by simulation studies [134, 135]. Marquet *et al.* [136, 137, 138] in a series of papers showed that spermine both bends DNA in A+T-rich regions and stiffens it in G+C rich regions. Experiments involving single DNA molecules stretched by optical tweezers have deduced that both the persistence length and the stiffness are dramatically altered in unexpected manner in the presence of ions and condensing agents [139]. Rouzina *et al.* [140] argued that binding of multivalent cations can induce sequence dependent "infrequent but strong" DNA bending with the overall effect of decreasing the persistence length and increasing the entropic flexibility. Tobias *et al.* [141] showed theoretically the DNA sensitivity to small structural changes at the free end. These small changes, which may be induced by anchoring of condensing agents, could lead to large variations on the tertiary structure. Recently, Coleman *et al.* [142] presented a theory where in stress-free double-helix DNA, the local bend, twist, and stretch of DNA varies from one base-pair step to another.

5.3 Experiments

In this experiment a Y-shaped flow cell was used as shown schematically in Figure 5.1. The cell was 40 $\pm$ 5 μm deep while each channel was 2 mm wide giving a combined channel of 4 mm width. The two channels meet at an angle of 20° and the corners were slightly rounded in order to have less perturbation of the flow and prevent mixing. The two inlets and the outlet of the channels were made in a similar way as for the single channel flow cell and were also connected to silicon rubber tubing by plastic tips. The different samples (solutions) were introduced into the channel through two 1 ml syringes attached to a computer controlled moving stage (COHERENT). The two channels were called the *sample zone*: where the DNA-beads are located and the *reaction zone*: where the spermidine-buffer flows.

The experimental set up and preparation of the DNA-bead sample have been described previously. In the experiments described in this chapter two different samples were used.

The first one was comprised of:

- 720 μl of 20 mM Tris-HCl buffer
- 15 μl of 2-mercaptoethanol (2%)
- 15 μl of an anti-fading agent (a mixture of 2.3 mg/ml D-(+)-glucose, 0.1 mg/ml glucose oxidase, 18 μg/ml catalase and 20 mM 2-mercaptoethanol (1 in 50 parts), and
- 2 μl of the DNA-bead sample ($C_{\text{final}} = 0.2$ pM).

The second one :

- 717.89 μl of 20 mM Tris-HCl buffer

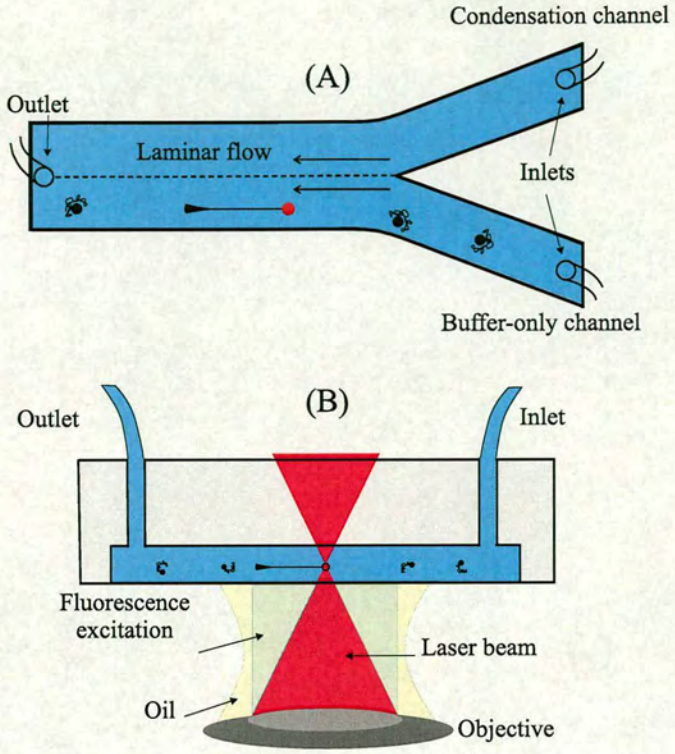

Figure 5.1: (A) Top view of the flow cell. The DNA-bead was pumped from the sample syringe and the spermidine from the reaction syringe into the channels with the same speed, producing a laminar flow within the sample and reaction zones. By moving the optically trapped bead, the attached linear DNA was transfered from the sample zone into the reaction zone where the condensation occurred. (B) Side view of the flow cell. The cell had a glass window on the bottom allowing excitation of fluorescent dye molecules intercalated on the DNA.

- 15 μl of 2-mercaptoethanol (2%)
- 15 μl of an anti-fading agent (a mixture of 2.3 mg/ml D-(+)-glucose, 0.1 mg/ml glucose oxidase, 18 μg/ml catalase and 20 mM 2-mercaptoethanol (1 in 50 parts), and
- 2.11 μl of Spermidine $(NH_3C_3H_6NH_2C_4H_8NH_3)^{3+}$, $C_{\mathrm{Sp}} = 2$ mM.

All the above were kept separately in a light-sealed box full of ice. The cell was coated

by a BSA liquid in order to inhibit the beads adhering to its walls and then rinsed with the same buffer used at the experiments. After that stage the lights were switched off and the two samples were prepared by mixing the above components.

Both samples were introduced simultaneously into the cell, initially by pushing the syringes very slowly by hand and then by attaching them to the driven stage. We verified that the mixing between the two samples is negligible by taking brightfield images while scanning across the cell: the two zones are well defined by the presence (sample zone) or absence (reaction zone) of beads and the mixing region is limited. The flow speed was measured by recording a sequence of brightfield images in the sample zone at an exposure time of 1 ms: thus, it was possible to measure the trajectory length and the corresponding time. The maximum flow rate standard deviation was 13%. We used velocities in the range of $\approx$ 50 to $\approx$ 250 μm/s.

The experiment was done in the following way: First a bead was trapped in brightfield at a measured height of $\approx$ 9-10 μm above the lower surface of the cell. The imaging was then switched to fluorescence to check whether the DNA was attached to the bead. On a "good" day a 35% rate was achieved. There were also cases where two beads were trapped or more than one molecule were attached to one bead or the DNA was cut. We selected for analysis only those events where one DNA molecule with a length deviation of no more than $\pm$ 0.5 μm from the expected length was observed (in order to minimise length polydispersity effects). We estimate that the error in determining the length of any particular DNA molecule is $\pm$ 0.2 μm.

The bead-DNA was transfered to the *spermidine reaction zone* by moving the microscope stage. The time for the molecule to collapse was recorded and if the fluorescence image was still good enough the bead-DNA was transfered back to the sample zone and the whole procedure was repeated until the molecule was not adequately visible anymore or the DNA became detached from the bead.

Four different series of measurements were performed: two different lengths of DNA,

with contour lengths of 16.5 μm and 8.2 μm, were introduced in buffers with and without NaCl. The concentration of the added NaCl was 5 mM. The exposure time for all the movies recorded varied depending on the length and the ionic conditions: e.g. for the 24 kbp fragment in Tris-buffer we used $t_{\rm exp} = 25$ ms while for the 48 kbp DNA in 5mM NaCl Tris-buffer $t_{\rm exp} = 200$ ms.

The lag time was measured as follows: in the sequence of the fluorescent images (while we transfer the bead-DNA to the reaction zone) we identified the first frame where no beads appeared floating in the field of view signifying the moment of entrance into the reaction zone; Afterwards (and if no more beads were observed) we identified the first frame where the DNA was fully collapsed [4]. The difference in time between the two images corresponds to the lag time τ_l.

5.4 Results

Figure 5.2 (A)-(E) shows a typical example of fluorescent images at the different stages of the experimental procedure. The bead was trapped and the DNA was stretched by the hydrodynamic flow (A), then it was moved into the reaction zone (B), a rapid short contraction was observed in the reaction zone (C), in addition the fluorescent image faded continuously (D) until condensation occured abruptly (E).

DNA observed in pure buffer did *not* significantly fade over the same period. This indicates that the fading mechanism in the reaction zone is not related to photobleaching.

Figures 5.3 and 5.4 show 3D and 1D fluorescence intensity plots respectively. Initially the hydrodynamically stretched DNA molecule was outside the sperimidine reaction zone, and the conformation was reminiscent of the stem and flower regime [80, 82]: Starting at the tethered end the DNA was stretched and appeared to take the conformation of an almost straight line for a considerable amount of length (stem); while at the

[4]The collapse of the DNA occurs in one frame in the vast majority of the cases.

free end the stretching was much less and the thermal fluctuations produce a disordered "protrusion" (flower) (see previous Chapter for details on the DNA shape under flow).

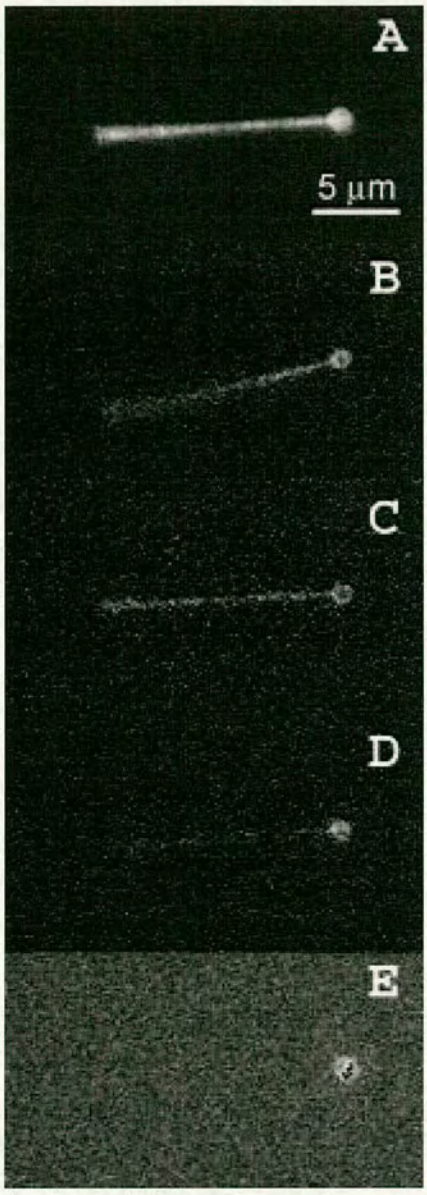

Figure 5.2: Fluorescence images of a DNA molecule (A) in the sample zone without spermidine, (B) entering into the reaction zone, (C) in the spermidine reaction zone, (D) in the spermidine reaction zone after a few seconds (just before collapse), (E) just after collapse.

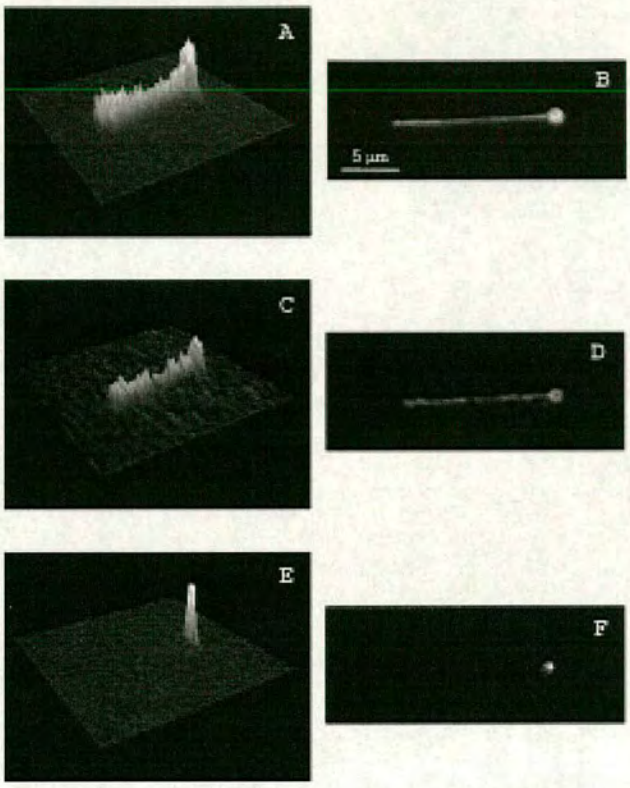

Figure 5.3: 3D fluorescence intensity plots and fluorescence images of (A, B) in sample zone without spermidine, (C, D) in the spermidine reaction zone, (E, F) after collapse.

We clearly observed a small contraction δL_{fast} in the DNA length of 0.7 $\pm$ 0.4 μm upon entrance within the spermidine reaction zone which subsequently remained constant (until collapse). This difference in length corresponds to a percentage shortening $\delta L_{\text{fast}}/L_{\text{init}}$ of 2% to 9% (L_{init} is the initial length before the entrance of the DNA in the spermidine zone). The contraction decreased with the increase of flow velocity and possibly reached a saturation at higher speeds as shown in the Figure 5.5.

This small contraction was followed by a long period (several seconds) during which the DNA seemed unaffected until suddenly collapsed. The collapse happened very rapidly, typically the time resolution used was inadequate to follow it. There were very

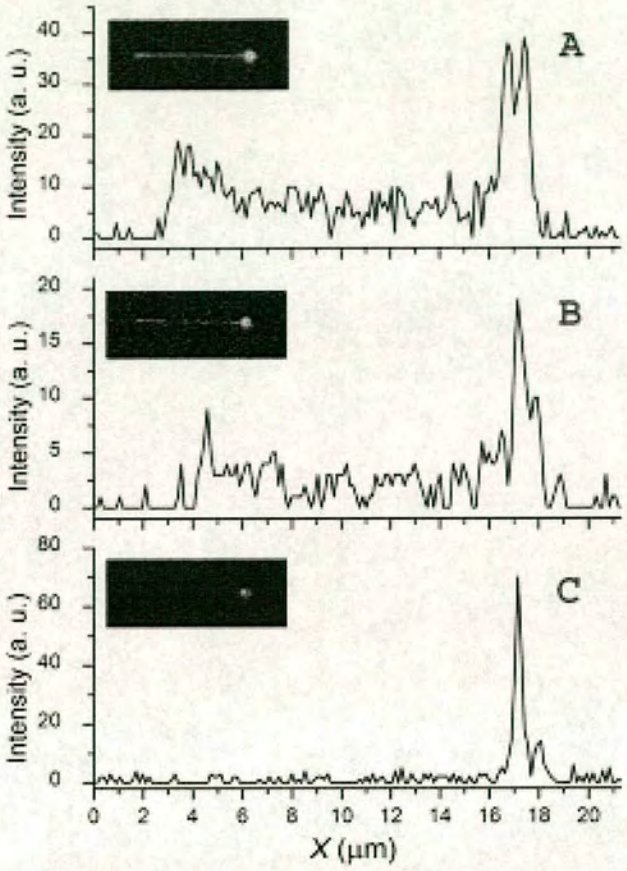

Figure 5.4: 1D Fluorescence intensity plots along the stretched DNA molecule (the inset shows the corresponding fluorescence image): (A) in sample zone without spermidine, (B) in the spermidine reaction zone, (C) after collapse.

few exceptions where the collapse was slow enough to allow some intermediate snapshots (Figures 5.6 and 5.7). The nucleation event appeared to happen at the free end and then the collapse proceeded rapidly along the DNA backbone towards the tethered end. The limited resolution of optical microscopy combined with the blurring effect of fluorescence microscopy did not permit us to observe the shape of the condensed shape.

The condensation by spermidine was observed in buffers of both lengths of DNA, with

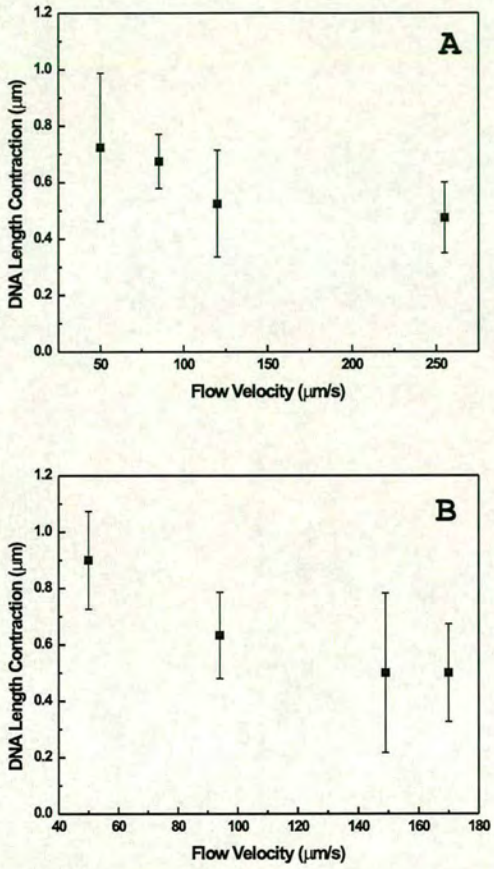

Figure 5.5: Contraction of the 48 kbp λ- phage DNA upon entrance in the spermidine reaction zone at different flow velocities (A) without NaCl and (B) in NaCl. Increasing the flow velocities there was a progressive decrease in the shortening.

and without NaCl, over a flow range of about 50 to 250 μm/s. The latency period within the reaction zone was the longest time of the whole condensation process and thus it constitutes the dominant feature of the experiments.

Figure 5.8 shows the lag time τ_l plotted versus the flow velocity v for two different DNA strand lengths and two ionic strengths. The error bars correspond to one standard deviation, σ, in the measured velocities and latency times. The data at each point

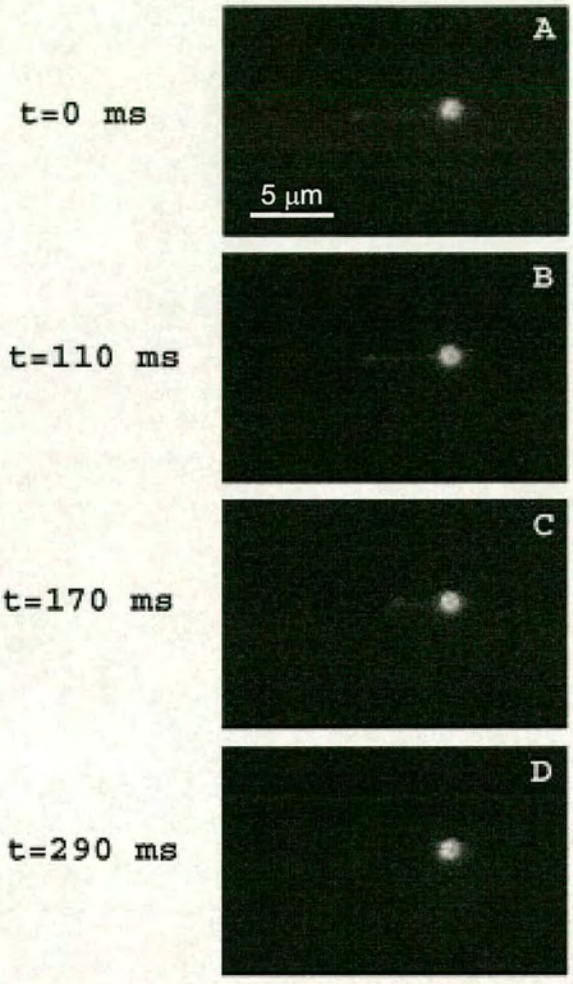

Figure 5.6: Fluorescence images of successive snapshots during condensation for 24 kbp fragment of λ-DNA: (A) nucleation at the free end, (B, C) progression of condensation towards the tethered end, (D) complete collapse. The flow velocity was 80 μm/s.

were obtained by averaging four to nine runs. We observe that: (I) the latency time is monotonically increasing (roughly linear) over this range. The lines in Figure 5.8 are a guide to the eye. The curve corresponding to short DNA without NaCl has a quite gentle slope and it is difficult to determine where it crosses the velocity axis. The rest of the curves extrapolate to lower velocities when the latency time becomes

small $\tau_l \rightarrow \approx 0$ μm/s. It is also noted that the linear extrapolation of the curve corresponding to long DNA with NaCl crosses the velocity axis at low negative velocities but within the standard deviation range ($\pm$ 13 %) of our flow velocity measurements [5]. (II) the latency time increased dramatically with the addition of salt for both DNA strand lengths. The lag time vs flow velocity curves became steeper with the addition of salt. The effect is more pronounced for the short DNA strand. (III) The latency time strongly depends on the length of the DNA strand and it was longer for the long one.

Figure 5.9 shows the effect of consecutive exposures to the spermidine reaction zone. The DNA was left for a few seconds outside the reaction zone in the period between the consecutive re-entries. It is clear that the latency time decreased on the second entrance to the reaction zone and decreased even further upon a third exposure.

[5]However, we cannot exclude the possibility of non-linear behaviour at low velocities.

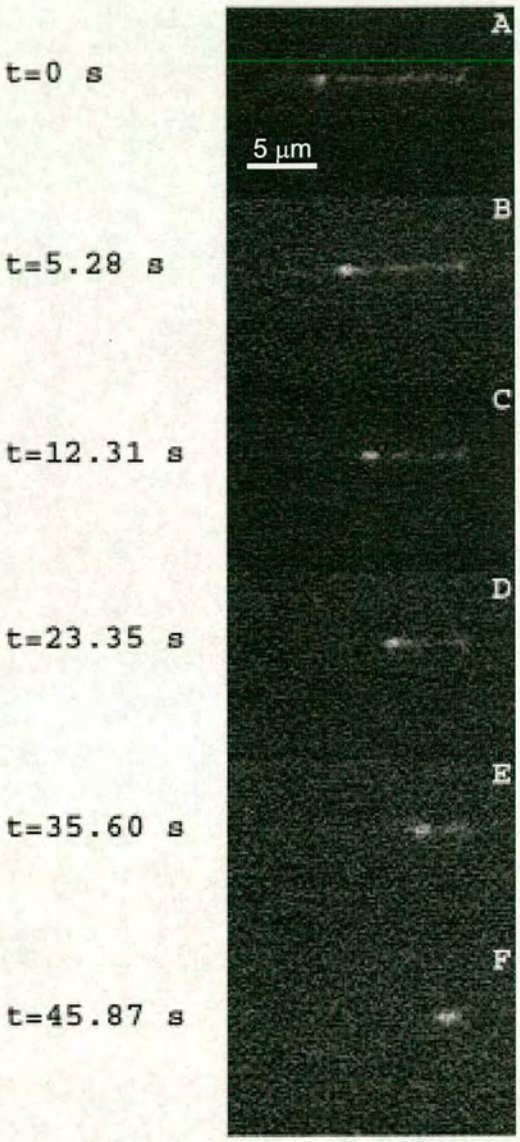

Figure 5.7: Series of successive fluoresence images during collapse (48 kbp λ-DNA). The flow velocity was 94 μm/s. The collapse started at the free end (A) and initiated a cascade of aggregation which progressed towards the tethered end (B-E) until the full collapse (F). It has to be stressed that the *duration of this particular condensation was untypical*: in 99% of the cases the collapse took $\lesssim$ 100 ms. It was observed that this particular bead carried two DNA chains which collapsed slowly in an entangled formation. Intermolecular aggregation takes much longer times to finish [126].

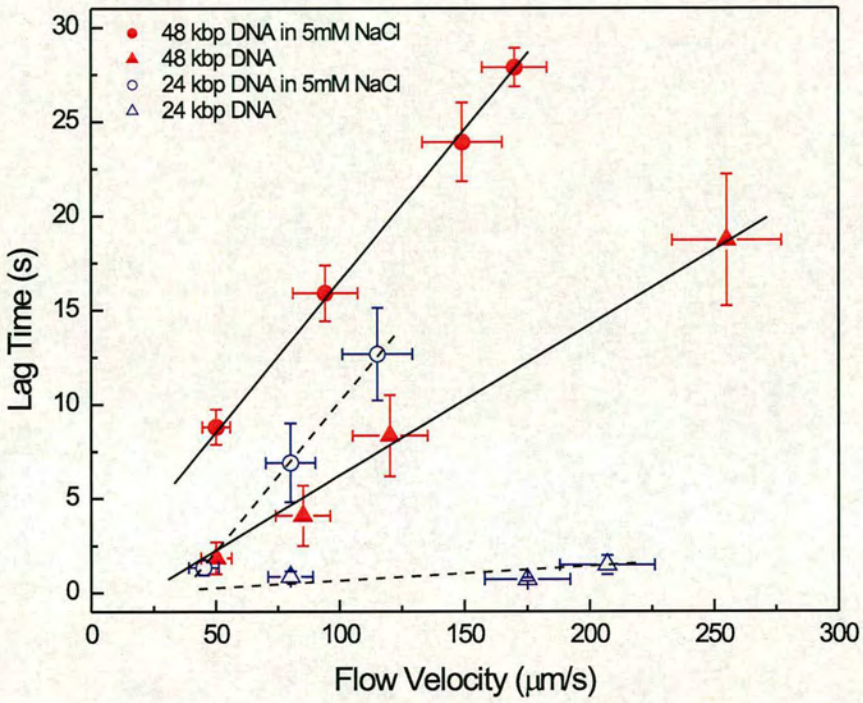

Figure 5.8: Plot of the lag time (time interval in spermidine until condensation occured) versus the flow velocity for: (i) 48 kbp DNA in 5 mM NaCl (filled circles) and without NaCl (filled triangles), (ii) 24 kbp DNA in 5 mM NaCl (open circles) and without NaCl (open triangles). The lines are to guide the eye: continuous line for 48 kbp DNA, dotted line for 24 kbp DNA.

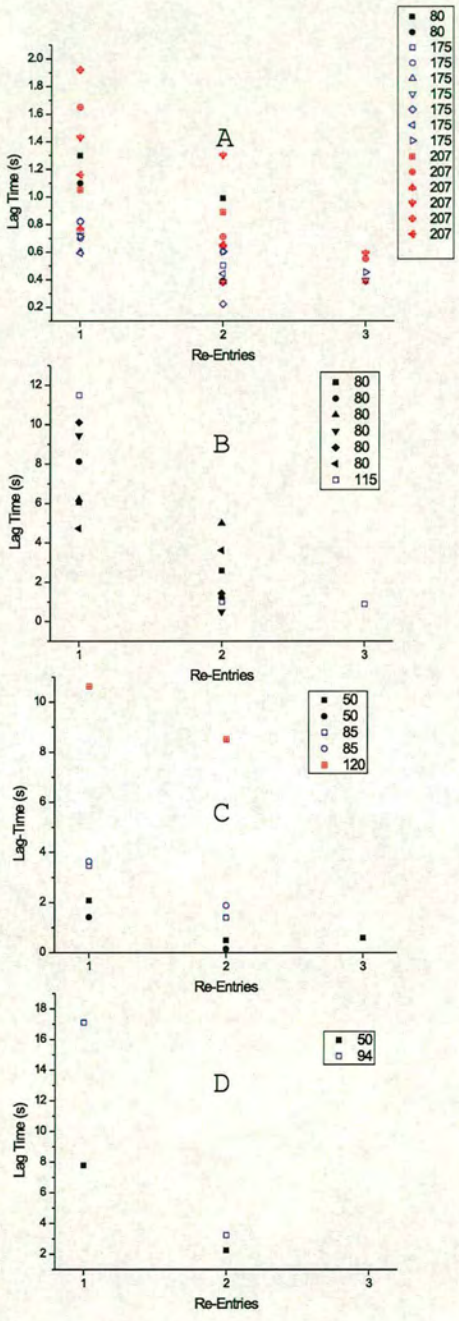

Figure 5.9: Plot of the lag time associated with consecutive exposures into the spermidine reaction zone for 24 kbp DNA: (A) without NaCl & (B) in 5 mM NaCl; for 48 kbp DNA: (C) without NaCl & (D) in 5 mM NaCl.

5.5 Discussion

5.5.1 Nucleation Time

The most striking observation of our experiments is the long latency times τ_l which preceded the collapse of DNA (Figure 5.8). Firstly, it is important to discuss the nucleation time of the collapse. Condensation experiments [113, 114] under flow have shown that the nucleation occurs at the free end, while condensation experiments without flow have clearly shown the possibility of nucleation within the backbone of the DNA molecule [143, 139]. The end segment (if free) is the most probable initiator of the nucleation since it has increased rotational freedom compared with the movement of the segments within the length of the chain. However, nucleation along the chain is not impossible. Simulations [121, 144] suggest that the effect is nucleated by random encounters of segments and the nucleation time is mainly governed by the diffusive (Brownian) movement of the segments and the expectancy time to encounter another segment. The diffusive relaxation time of a "monomer" Kuhn segment of length $a = 2\ell_p$, which signifies the time duration τ_{B} (order of mangnitude) required for the segment to move a distance of its own size a [97], can be a good estimate for the zero-flow Brownian nucleation time τ_{nucl}:

$$\tau_{\mathrm{nucl}}(v=0) \gtrsim \tau_{\mathrm{B}}(v=0) \approx \frac{\eta a^3}{k_{\mathrm{B}}T} \approx 0.25 \text{ ms} , \tag{5.16}$$

where η is the solvent viscosity and $k_{\mathrm{B}}T$ is the thermal energy (we used $\eta = 1$ cP $= 10^{-3}$ Pa s, $a = 100$ nm). This estimate in the ms range is not far from Porschke's measurement of an induction time of ≈ 10 ms and for cation coverage kinetics of ≈ 100 ms (for 1.5 μM spermine [126]). We assume that the nucleation process at zero velocity is governed by an effective activation energy U_0 and we make an Arrhenius' law argument to estimate the effect of the flow on the expectation time of the nucleation at finite velocities. The hydrodynamic drag tends to straighten out the DNA which

decreases the mobility of the segments and diminishes the probability of a segment-segment encounter. The rate of "successful" segment-segment encounter events at zero velocity is proportional to the Boltzmann weight $\tau_{\rm nucl}^{-1}(v=0) \propto e^{-U_0/k_{\rm B}T}$. The hydrodynamic drag tends to straighten out the DNA which decreases the mobility of the segments and diminishes the probability of a segment-segment encounter. At a finite flow velocity v, a drag force of $f \approx \eta v L$ increases the effective activation energy to $U(v) = U_0 + fa$ which decreases the rate of "successful" segment-segment encounters to $\tau_{\rm nucl}^{-1}(v) \propto e^{-(U_0+fa)/k_{\rm B}T}$. Thus, a lower bound (and an order of magnitude) estimation of the nucleation time at a finite velovity v is

$$\tau_{\rm nucl}(v) \approx \tau_{\rm nucl}(v=0) \times e^{fa/k_{\rm B}T} \gtrsim \tau_{\rm B}(v=0) \times e^{fa/k_{\rm B}T} \,. \tag{5.17}$$

The drag force increases along the backbone of the chain and towards the tethered end making the probability of nucleation within the length of the chain almost impossible. However, the drag force at the free end is $\approx \eta v a$ and the exponential factor remains in the order unity, even for the maximum flow velocity, v = 250 μm/s, used. Consequently, in the case of "instantaneous" and uniform binding of spermidine along the whole DNA length (we will see later that we believe that this did not occur in our system) one could expect that an "instantaneous" nucleation event at the free end is enough for a progression of the nucleation towards the tethered end of the DNA. In other words, the expectancy time of the nucleation event at the free end (which can induce complete condensation in the case of uniform spermidine binding) remains small and unaffected by the flow and it is unlikely to be the reason for the condensation latency times, $\approx$ 1 to 30 s, we observed. There should be an additional reason (beyond the direct effect of the flow on nucleation kinetics) to account for the delay of the nucleation event to progress towards the tethered end of the chain.

5.5.2 Competition with YOYO-1

We now turn our attention to the competitive binding of spermidine and the fluorescent label YOYO-1. At zero flow, spermidine has to displace other cations already bound to the DNA including charged dyes such as the YOYO-1 dye which we used to fluorescently label the DNA. In order to induce condensation, the spermidine has to neutralize $\gtrsim 90$ % of the negative charges on DNA. Yoshinaga *et al.* [145] and Murayama *et al.* [146] showed that the critical spermidine concentration needed for condensation of YOYO-1-dyed DNA is much higher than when the DNA is not labeled by YOYO-1 indicating that the spermidine competes with the fluorescent label for binding on the DNA backbone. This is consistent with our observation of rapid fading of the DNA molecule when it is situated within the spermidine-reaction zone of the cell (Figures 5.2, 5.3, 5.4). This fading effect cannot be attributed to photobleaching because it does not happen when spermidine is absent. Our data indicate a latency time which tends to very small values ($\tau_l \to 0$ s) at zero flow velocity and in the literature there is no evidence of any significant delay time in spermidine-induced YOYO-1-bound DNA condensation under zero flow. Thus, we deduce that it is the flow which inhibited the spermidine binding and led to a slow replacement and release of YOYO-1 bound molecules.

5.5.3 Kinetics of Replacement of YOYO-1

Flow might have an influence on spermidine binding since continuously drags molecules away from the DNA backbone. In order to evaluate the effect of the flow with respect to the diffusive motion for a molecule with characteristic size d, we take the ratio of the time it takes the molecule to diffuse its own linear dimension (diffusive relaxation time): $\tau_B \approx \eta d^3/k_B T$ and the time it takes the flow to *convect* it along the same distance: $\tau_v \approx R/v$. Thus, $\tau_B/\tau_v = \eta v d^2/k_B T \sim 10^{-4}$ for an object of size $d = 1$ nm at $v \sim 100$ μm/s in water. This means that the flow has almost no influence on the

"residence time" of a spermidine molecule at a binding site, i.e. the "residence time" is dominated by diffusion.

5.5.4 Spermidine-induced Bending

The flow can affect the spermidine binding in another rather unexpected way. Rouzina and Bloomfield [140] have shown that multications can induce surprising strong bendings of the order of 20-40° every 6 bp. These bendings are difficult to attain at the highly-stretched stem segments of the DNA chain making the spermidine binding difficult. The enthalpic penalty which needs to be paid for creating the bending when the chain is subjected to a force f is [147, 148]

$$\Delta E_{\rm enth} \approx \alpha^2 \sqrt{\kappa f}\ , \tag{5.18}$$

where α is the bending angle induced by the spermidine bonding and $\kappa = \ell_p k_{\rm B}T$ is the bending stiffness of the DNA. The binding energy of the spermidine on a free to bend DNA is $\approx$ 1 - 3 $k_{\rm B}T$ [149] and in the case of a tension f which tends to stretch out the DNA is reduced by the above amount $\Delta E_{\rm enth}$. As we have discussed, the (hydrodynamic drag) force acting on the DNA in our experiment varies along its length and the maximum drag experienced at the tethered DNA end is $f \sim \eta v L(v)$, where $L(v)$ is the length of the DNA stretched out by a flow of speed v. Assuming $\alpha \approx 20\,^\circ \equiv \pi/9$ radians [140], $L(v) \approx 16\ \mu$m (i.e. the contour length of λ-DNA) and $v = 100\ \mu$m/s, we find that $\Delta E_{\rm enth} \approx k_{\rm B}T$. Thus, we deduce that the flow-induced correction $\Delta E_{\rm enth} \approx 1\ k_{\rm B}T$ is comparable to the binding energy of spermidine on tension-free DNA and subsequently was a strong effect in our experimental system. Furthermore, force measurements with dual-trap optical tweezers [143, 150, 151] have shown characteristic plateaus of $\approx$ 1 pN in the force. Plateau-type forces were predicted [152, 153] during the elongation of a collapsed chain in poor solvent conditions. Halperin *et al.* [152] argues that this phenomenon corresponds to a first order transition of a collapsed globule to a stretched chain and during the force plateau, a globular

domain coexist with a stretched chain domain. The analogy with the DNA force experiments is direct and implies that forces in the order of $\approx$ 1 pN are strong enough to induce the transition from a collapsed spermidine-bound state to the stretched chain without any bound sperimidine [6]. This means that a tension of $\approx$ 1 pN is sufficient to unbind any bound spermidine from DNA. In our experiments the maximum force at the tethered end (for $L = 10\ \mu$m and $v = 100\ \mu$m/s) is $f \approx \eta v L \approx 1$ pN. Consequently, we expect that flow-induced stretching inhibits significantly the ability of spermidine to bind on DNA for a large portion of its length beginning from the tethered end. We attribute the long latency times observed to this effect.

5.5.5 Fast Contraction

Baumann *et al.* [139] showed that an addition of spermidine leads to a decrease in the persistence length of DNA. This effect is attributed to infrequent but strong bending induced by multication binding in the major groove of DNA which has already been discussed. The IS and spermidine concentration they used were not in the same range with our experiments but from their measurements is reasonable to assume a maximum of $\approx$ 20 % decrease. As we have discussed the spermidine will bind mainly near the free end of the DNA. We saw in the previous chapter that the first, least stretched blob at the free end has a size (for $v = 100\ \mu$m/s and $\eta = 10^{-3}$ Pa s):

$$R_1 \approx \sqrt{\frac{k_B T}{\eta v}} \approx 0.2\ \mu\text{m} . \tag{5.19}$$

If this blob contains N_1 Kuhn segments of size a, the size of the blob is $R_1 \approx N_1^{0.6} a$ which after contraction ($\tilde{a}$ = 0.8 a) is $\tilde{R}_1 \approx \tilde{N}_1^{0.6}\tilde{a} = \left(\frac{N}{0.8}\right)^{0.6} 0.8\ a = 0.91\ R_1 \approx 0.18\ \mu$m. This leads to a difference in length of $R_1 - \tilde{R}_1 \approx 0.02\ \mu$m, which is not consistent even in the order of magnitude of the contractions we observed (Figure 5.5).

[6] During the transition both states co-exist. This is in analogy with the co-existence of saturated liquid and saturated vapour during simple liquid evaporation which is a first order phase transition.

However, if we assume that the spermidine binding in this blob follows the (probably) very fast zero-flow kinetics (see subsection 5.5.1) one can expect an "instantaneous" condensation of the first blob (and perhaps the first few blobs) upon entry in the spermidine reaction zone resulting in an "instantaneous" contraction of $\delta L_{\text{fast}} \gtrsim 0.2$ μm, which is consistent with the order of magnitude of our measurements (Figure 5.5). Far from the free end and closer to the tether the chain is significantly stretched and straightened out by the flow (stem) inhibiting the binding of spermidine and our previous considerations apply, giving rise to the long latency times (see subsection 5.5.4). At higher velocities the stem part of the chain increases and the flower part decreases resulting in progressively smaller shortenings. The contraction should reach saturation at very high velocities due to the decreasing influence of the flower (at very high velocities we expect a stretched stem-alone conformation) in qualitative agreement with the decreasing slope in our data (Figure 5.5). Quantitatively, we can estimate the dependence of the contraction on the flow velocity by applying the approximation $\delta L_{\text{fast}} \approx R_1$; from Equation (5.19) we obtain:

$$\delta L_{\text{fast}} \text{ (in } \mu\text{m)} \approx \frac{2}{\sqrt{v \text{ (in } \mu\text{ms}^{-1})}} . \tag{5.20}$$

A two-parameter free fit to the shortening data (Fig. 5.10) collected for the long DNA in high salt gave (in the same units as above) $\delta L_{\text{fast}} = 6.6v^{-0.51}$ (regression coefficient = 0.99). The strikingly good fit is no doubt fortuitous[7] but it is indicative that we are on the right track.

5.5.6 Length Dependence

The length dependence on the latency time is rather surprising: One would expect that for the same flow velocity the shortest molecule has a higher fraction of its backbone stretched, and taking into account the arguments associated with the decreased affinity

[7]The data without salt do not work nearly so well: free fit gives a -0.3 exponent.

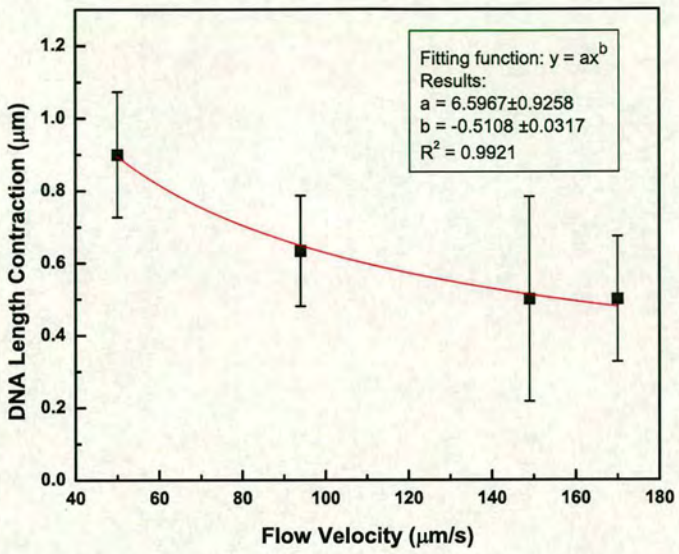

Figure 5.10: Contraction of the 48 kbp λ-phage DNA in NaCl at different flow velocities.

of spermidine for the stem part of the chain, one deduces that the latency times would be longer; the opposite was observed. However, we note that since the drag force is proportional to the length L, the tension exerted on the tethered end section of the DNA will be larger for the long molecule resulting in stronger stretching and thus in decreased rates of spermidine binding compared with the shorter chain. Quantitatively, from Equation (5.18) and since $f \propto L$ we deduce that $\Delta E_{\text{enth}} \propto \sqrt{L}$: longer DNA lengths result in a higher enthalpic penalty for the spermidine binding which indicates that the associated latency times should be longer for the longer chains in agreement with our observations (Figure 5.8). Applying Equation (5.18) we obtain an amplification factor of $\sqrt{2} = 1.41$ for a DNA molecule with double length, which might be significant since we have already estimated that the enthaplic penalty ΔE_{enth} is of the order of magnitude of the spermidine binding energy.

Furthermore, the bending stiffness of the free end depends strongly on the *specific* DNA sequence near the free end which is different for the two strands. Consequently, the observed behaviour might be also affected by local variations in stiffness near the free end of the full-length λ-DNA and its fragment. As we have already mentioned models for sequence specific DNA stiffness have already appeared: Coleman *et al.* [142] presented a theory where in stress-free double-helix DNA, the local bend, twist, and stretch of DNA varies from one base-pair step to another. Tobias *et al.* [141] showed theoretically the DNA sensitivity to small structural changes at the free end. Our findings and arguments have stressed the importance of the bending stiffness, flexibility and conformational kinetics of the free end since (in our system) it is there that the condensation is nucleated, a sequence specific dependence is not far-fetched. However, a simulation study accounting for the exact base sequence at the free end has to be employed to elucidate this point.

5.5.7 Salt Dependence

We observed longer latency times upon the introduction of NaCl (Figure 5.8). The effect of NaCl concentration on the latency time is complicated and several effects might be involved:

(i) Salt decreases the persistence length of DNA [139] leading to faster Brownian diffusion (Equation (5.16)); *thus, the latency time is expected to decrease.*

(ii) Shorter persistence length leads also to a smaller overall size, which results in weaker tension and consequently weaker stretching and smaller enthalpic penalty for the spermidine binding (Equation (5.18)); *thus, again we expect a shorter latency time.*

(iii) Baumann's *et al.* data at the strong stretching limit [8] (Figure 5 and Table 1 in reference [139]) reveals that the persistence length variations in our range of I ($\approx$ 22 mM

[8] Which is more relevant for estimating the probabilities of a nucleation effect involving few Kuhn segments and extreme bending.

to 27 mM) are small while the enthalpic (bending or stretching) stiffness increases dramatically (and surprisingly) with I. Electrostatically, this is very unexpected since increasing the concentration of counterions should lead to a decrease of the DNA charge and decreased stiffness. However, it is not all electrostatics, they argue that the reason for this unexpected behaviour might be the localised melting of A+T rich regions at low I. In general, increase in I will reduce local melting, increasing enthalpic (stretching or bending) stiffness and also reduce intermolecular electrostatic repulsion increasing flexibility (i.e. decreasing the entropic stiffness). In our range of I the former effect is more significant than the latter leading to a slowing down of kinetics upon the introduction of NaCl in the solution. It becomes much more difficult for the free end to create a small loop of high curvature with the adjacent segments and initiate collapse; *thus, we expect a longer latency time.*

(iv) It has been observed that increasing the salt concentration results in an increase in the minimum multication concentration necessary to induce collapse [106, 108]. This implies that there is a competition for DNA binding between NaCl and Spermidine. The small monovalent Na^+ cations quickly diffuse and bind on the DNA chain in large numbers decreasing the number of possible reaction sites for the spermidine. Energetically, the spermidine^{3+} multication binding is more favourable and it is expected that ultimately a large number of Na^+ will be replaced by the spermidine molecules. *This replacement process might take extra time and lead to a longer latency time.*

Since addition of salt led to longer latency times, we suggest that effects (iii) and (iv) as the dominant ones.

5.5.8 Collapse Time

Apart from very few exceptions the DNA collapse time was short ($\lesssim$ 100 ms) and at the time resolution limit of our experimental system. The duration is an order of magnitude shorter than with other condensing agents such as protamine [113] and histones [114].

It is difficult to establish the underlying reasons of these differences since the exact mechanism of DNA condensation is not well-understood and it might be vary with different condensing agents. Our measurements might indicate that the spermidine is a more efficient bridging agent between different segments of DNA during the collapse cascade process (and after nucleation).

5.5.9 Re-entries

Successive re-entries into the reaction zone resulted in shorter times (Figure 5.9). This is clearly because most of the YOYO-1 molecules have already been irreversibly displaced during the first long entry, so that spermidine binding now does not have to involve displacing a large number of strongly bound fluorescent-dye molecules.

5.6 Conclusions

We have employed single molecule fluorescence imaging combined with optical tweezers and a laminar flow cell to study the nucleation kinetics of DNA condensation. It was found that the spermidine-induced condensation of hydrodynamically-stretched linear DNA involves three steps: (i) an initial rapid contraction followed by (ii) a long latency period which depends on the flow velocity, ionic strength and DNA length (iii) until the DNA collapses suddenly and rapidly. We have argued that the observed behaviour is due to a combination of several effects, mainly: limited diffusion at the stretched part of the chain, competition in DNA binding between spermidine and the other cations (dye (YOYO-1) and Na^+) and *primarily stretching-induced spermidine-binding inhibition*. To our knowledge, this is the first experimental study of the kinetics of the initiation of DNA condensation under flow.

Part II

New Developments in Optical Tweezers Instrumentation

Chapter 6

Combining Optical Tweezers and Adaptive Optics

6.1 Introduction

As it has been mentioned before, there are extensive applications of optical tweezers in manipulation and force measurements in colloidal science where the colloidal particles are directly trapped, and in biological schemes where the species of interest are attached to micron sized transparent beads to facilitate trapping. When used for force measurement applications, accurate characterisation of the trap quality is required.

Lateral movement within the image plane can be simply obtained by either moving the sample with a fixed trap configuration, or for example with a twin plane galvanometer or piezo-electric mirror configuration that alters the angle of the trapping laser beam [154]. A well-corrected microscope objective is isoplanatic over a reasonable region about the centre of the field of view so the trap strength will be approximately constant. When a single objective is used both for trapping and imaging, movement of the trap out of the imaging plane requires partial defocus of the input laser beam. In this case

the trap is no longer located in the focal plane of the microscope objective, and the trapping quality degrades. Even when the trapping and imaging planes are coincident and they are displaced deeper into the sample the trapping quality still deteriorates, if there is no refractive index match.

This chapter presents the use of a miniature deformable membrane, an adaptive optical component[1] [155], to perform both the illuminating beam defocus and aberration correction. The optical properties of the membrane mirror used are also examined.

6.2 Background

6.2.1 Characterisation of an Optical Trap

Since tweezers have such a wide variety of applications, it is important to have a detailed characterisation of the trap, particularly in experiments with quantitative force measurements. There are several parameters describing the quality of an optical trap. The most important amongst these are the maximum trapping force, the potential depth of the trap and the force constant [156].

The trapping force F is given as the sum of two components the gradient and the scattering force. The maximum trapping force is the highest gradient of the potential well and can be found experimentally since it is equal to the escape force, i.e. the minimum constant force that has to be exerted to a particle in order to escape the trap. The potential depth is defined as the area enclosed by the force curve and the horizontal axis as depicted in Figure 6.1 [156]. The potential depth governs the stability of the trap and for practical use should be large compared to the thermal energy of the trapped particle.

[1] Optical components or assemblies whose performance is controlled so as to compensate for aberrations, or to adapt to changing conditions or needs.

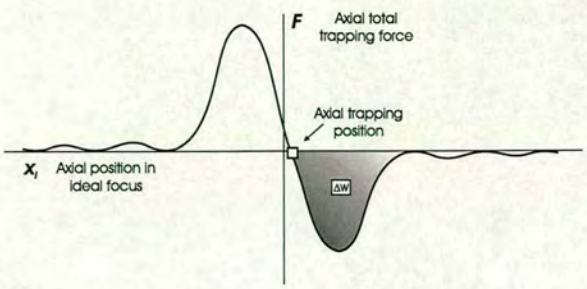

Figure 6.1: Plot of the total optical force versus the axial position of ideal focus. The grey area gives the potential energy depth, or the energy difference required by the trapped particle to escape the trap.

The force constant or trap stiffness is described as [154]:

$$k_{x_i} = \frac{dF}{dx_i} \tag{6.1}$$

where $x_i = x,y,z$ depending on which axis we define the stiffness for. It constitutes the slope of the force versus particle position graph and is therefore a measure of the spatial width of the trap. For a given laser power the larger the force constant measured the tighter the trap. The trap stiffness is of great experimental importance as it is used to get quantitative force measurements by recording the spatial displacement of the trapped particle from the trap centre. All three parameters, the maximum trapping force, the potential depth and the force constant are not independent and for a focused Gaussian beam they are related through a simple linear dependence [156]. In this ideal case measuring just one of the parameters is enough to characterise the optical trap completely.

6.2.2 Spherical Aberration-Effect on Optical Tweezers

As discussed previously, in order to create an optical trap a laser beam has to be tightly focused giving a diffraction limited spot. In most of the experiments, specimens (for example particles, bacteria or cells) are suspended in water while imaging and trapping

are performed by means of an oil-immersion high numerical aperture (NA) microscope objective. It is well known, that when focused light transverses a media interface it will experience spherical aberration which causes the outermost rays of the beam to focus in front of those in the centre (Figure 6.2) [38].

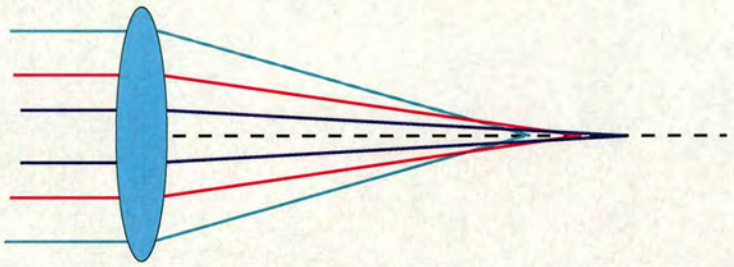

Figure 6.2: Spherical aberration caused by a single lens when light passes through; the outer rays focus closer to the lens.

A common way to overcome this problem would be to use spherical-aberration corrected microscope objectives. Such objectives correct spherical aberration by employing glass elements (combination of lenses) with different shapes in order to bring the peripheral and axial rays to a common focus. However, most objectives are well corrected for a certain image plane close to the surface of the cover glass whereas for many applications the optical trap should be as deep inside the sample as possible in order to minimise spurious interactions with the interface.

The result of the spherical aberration (SA) introduced by the refractive index mismatch at the glass-water interface is quite significant resulting in an elongated focus and the quality of the trap degrades rapidly as it is moved deeper inside the sample [156, 157]. This limits the trapping depth to a few tens of microns and makes quantitative force measurements very difficult, as the force calibration of the trap will be extremely sensitive to the depth inside the sample. Figure 6.3 presents the change of the focal position when light focused by an oil immersion microscope objective encounters the coverslip glass and then the sample. The actual focus position (AFP) is the depth where the rays come into focus, while the nominal focus position (NPF) gives the depth were they

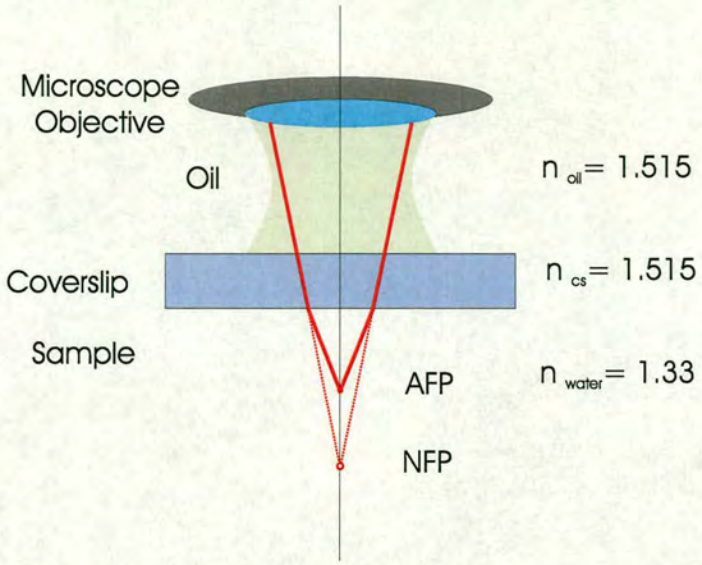

Figure 6.3: Spherical aberration by refractive index mismatch between the coverslip glass and the sample medium (here water). Here the second medium has a lower refractive index so the light rays bent more after the interface; dot lines represent the optical path for index-match and they are focused at the Nominal Focal Position (NFP) while the lines represent the aberrated optical path and the rays are focused at the Actual Focal Position (AFP).

would be focused if there was no light refraction. The difference Δz between the two positions is given by

$$\Delta z = \left(1 - \frac{n_{\text{water}}}{n_{\text{glass}}}\right) z\,, \tag{6.2}$$

where n_{water}, n_{glass} are the refractive indices of the water and the glass respectively, z is the distance of the NFP from the coverslip and AFP is obtained by multiplying the NFP distance by the relative refractive index [154]. Figure 6.4 shows the different intensity distributions of highly focus beams without and with SA. When a wavefront is incident on a interface the difference in refractive indices yields a change in the phase velocity and the direction of the wavefront. The intensity distribution at the aberrated focus was calculated by taking into account this phase change and was done by Dr. J. Arlt using

a LabView program based on the algorithm proposed in [156].

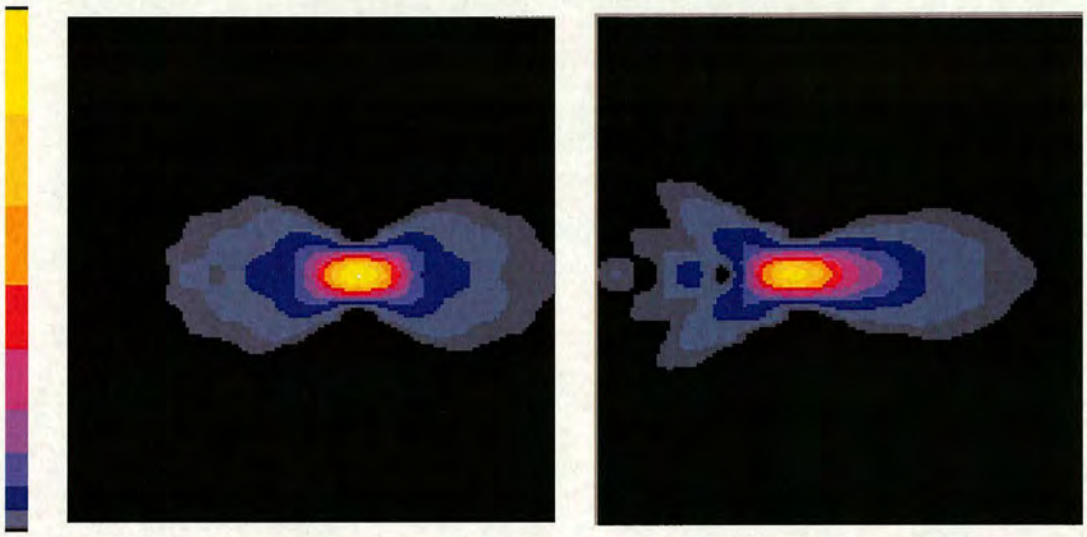

Figure 6.4: Intensity distributions of highly focused laser beams which propagate in z direction: Left the ideal focus and right the spherically-aberrated-focus. The horizontal axis corresponds to z-axis where the vertical one is either x or y axis. Each figure is 10 μm $\times$ 10 μm in size with z-axis extending from 4 μm to 14 μm. The nominal focus is 10 μm deep into water sample while the actual focus is at 8 μm. The scale, on the left, represents increasing intensity values as it goes from the bottom to the top.

As can be seen from Figure 6.4, spherical aberration mainly affects the axial intensity distribution around the focus, so it will mainly affect the axial trap parameters; at d = 20 μm deep into the sample the axial force constants are less than 10% of the corresponding lateral force constants [156]. Recently, there has been considerable theoretical and experimental interest in the effects of aberrations on the trap quality. Detailed simulations for both particles smaller than the wavelength of the trapping laser [156] and in the ray-optics regime [154] show that the quality deteriorates quickly with depth inside the sample, especially for very high NA objectives: for example Fallman and Axner [154] have calculated that the decrease of the trapping force is 76% for an oil immersion objective with NA = 1.35 when it goes deeper into the sample by 10 times the bead radius, while it is 52% under the same conditions for an objective with

NA = 1. The escape force has been studied experimentally for both upright [158] and inverted tweezers [159] and the effects of aberration on the spring constant are investigated in [160], including correction using a deformable membrane mirror (DMM). Very recently it has also been demonstrated that a spatial light modulator can be used for correcting aberrations [161].

6.2.3 Two-photon Fluorescence

To get an instantaneous measure of the trap quality, two-photon excitation fluorescence imaging can be applied. The method was initially incorporated in optical tweezers by Liou *et al.* [162] and has been used as a force probe in the pN-regimes by Florin *et al.* [163]. Since then it has been used quite often as a visual control for trapped particles [159, 164]. Two-photon excitation is accomplished through the *simultaneous* absorption of two photons each of them having half the energy required in order to excite the fluophore. The intensity of the emmited fluorescent light is [165]

$$I_{\text{fluor}} \propto I_{\text{exc}}^2 \tag{6.3}$$

where I_{exc} is the intensity of the excitation light. In the case of a particle trapped at the laser focus the instantaneous fluorescence signal is to first approximation proportional to the squared peak intensity of the trapping beam and as such is a measure for the potential depth of the trap, since a change in the two photon intensity signifies a corresponding change in the intensity at the focus of the laser beams and thus at the trapping forces.

6.3 Deformable Mirror: Description and Characterisation

The deformable membrane mirror (DMM) is a thin reflective surface and its fabrication is based on the technology of silicon bulk micromachining [155]. The membrane is made from a silicon chip coated with silicon nitride as shown in Figure 6.5. This results in extremely strong and very thin membranes, in the order of 100 nm. The back of the silicon it etched out and the front is covered by gold or aluminium (as in our case) in order to become reflective. The aperture shape of the mirror is approximately circular and its diameter is 15 mm.

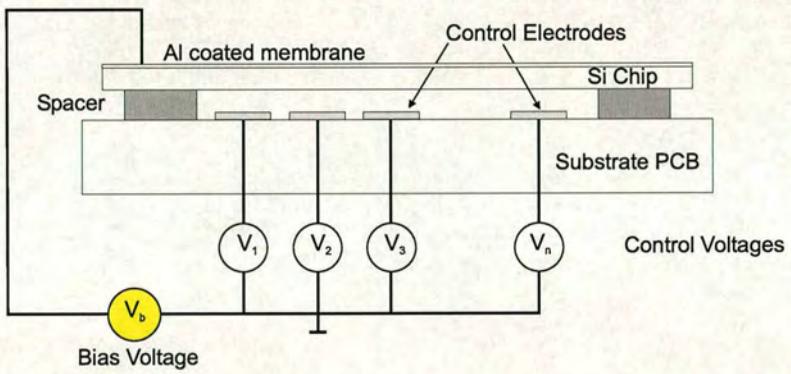

Figure 6.5: Schematic structure of the membrane. (Source: attached documentation included in mirror package.)

The chip is then mounted over a PCB (Printed Circuit Board) holder which comprise the spacer, the connector and a 37 electrode array. The gap between the chip and the holder is $\approx 100\ \mu$m. The electrodes are arranged in a hexagon grid and they control the shape of the membrane when voltage is applied to them. Figure 6.6 shows a photograph of the DMM and the array of the electrodes; as can be seen the hexagon consists of one central pad and three concentric rings. The centre to centre distance between the actuators is 1.833 mm and the whole structure is located within 12 mm circle under

the mirror. The maximum voltage applied to actuators is 180 V while the maximum optical load for a wavelength of 633 nm CW is 0.03 $\mathrm{W/mm^2}$.

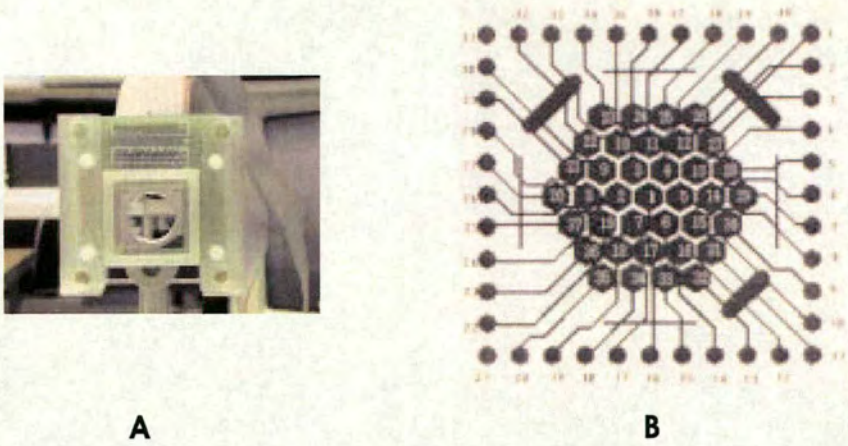

Figure 6.6: A): Photo of the deformable mirror. B): Electrodes array at the back of the mirror. (Source: attached documentation included in mirror package.)

The deflection $S(x, y)$ of the membrane, under an external load $P(x, y)$ is given by the Poisson equation [155]

$$\nabla^2 S(x, y) = -P(x, y)/T \,, \tag{6.4}$$

with boundary conditions:

$$S_c = Z_c = 0 \,, \tag{6.5}$$

where $S(x, y)$ is the deflection of the membrane, $P(x, y)$ is the load distribution, S_c is the deflection of the border and Z_c is the profile of the wafer on the membrane contour and T is the tension of the membrane and depends on membrane materials and dimensions.

If the voltage applied on the mirror is known then the pressure distribution is

$$P(x,y) \approx \epsilon \frac{V^2(x,y)}{2d(x,y)^2} \,, \tag{6.6}$$

where $V(x,y)$ is the voltage applied on the electrodes, ϵ is the dielectric constant, and $d(x,y)$ is the distance between the mirror and the actuators (in the general case this depends on the membrane deflection).

By applying voltage to the membrane we can change its shape and therefore we are able to compensate for low-order optical aberrations such as defocus, astigmatism, coma and spherical aberration. The result is an improvement to the imaging system and in our case a better trapping efficiency. In order to investigate the shape of the membrane a commercial Fizeau interferometer (Interfire 633) was used. Figure 6.7 gives the schematic diagramme of the interferometer, using a helium-neon gas laser of a few mW power, at $\lambda = 632.8$ nm in single mode as the laser source. The laser beam was initially focused through a very well corrected objective onto a 5 μm pinhole in order to remove coherent noise produced by reflections within the objective and give a clean beam. The expanded beam was then collimated using a lens before it impinged on the Fizeau plate. The latter was an optical flat with its front side partially reflective and the back side coated in order to be antireflective; with that configuration a portion of the beam was reflected back into the system while the rest of it travels to the component under test, i.e. the mirror in our setup, gets reflected back and the two beams interfere. The two beam dividers located in the beam path before the collimating lens enabled the capture of the interference fringes on a CCD camera as well as viewing them on a screen.

Φ(x,y) is the phase difference between the two beams in a double pass interferometer [166]

$$\Phi(x,y) = \frac{2\pi}{\lambda} 2d(x,y) \,, \tag{6.7}$$

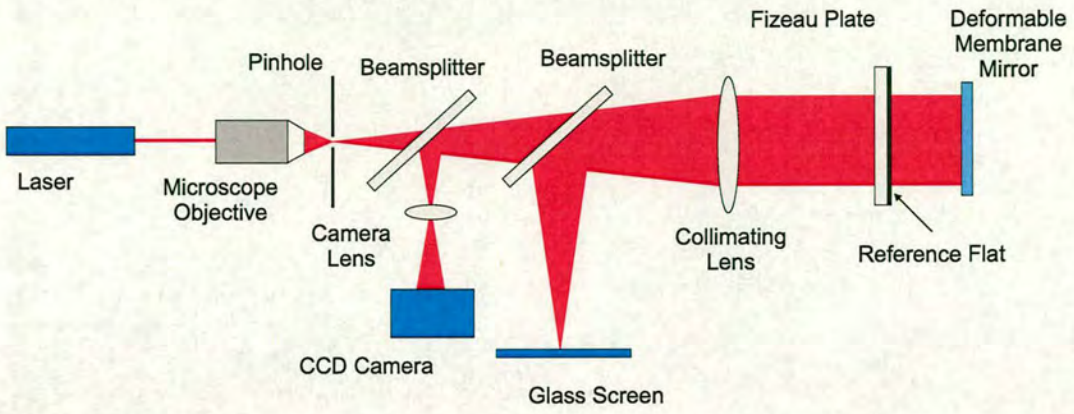

Figure 6.7: Arrangement of Fizeau interferometer.

where $2\pi/\lambda$ is the wavenumber, and the factor 2 arises from the fact that the beam passes twice from the mirror. The phase difference between consecutive bright or dark fringes is equal to 2π which corresponds to a distance of $\lambda/2$ as can be derived from equation (6.7). Thus, counting figures gives a measure of deformation in units of $\lambda/2$.

Figures 6.8 to 6.11 give the fringe patterns when different combinations of voltages applied to the mirror: in Figure 6.8 only the central pad was used and it can be seen that the number of fringes remained almost constant regardless of the voltage applied. When one or more rings are involved (Figure 6.9, 6.10, 6.11 give the patterns when the central and one, the central and two and finally the central and all three rings are used respectively) the number of fringes increases with a stronger effect for higher voltages. By comparing the different configurations for the same voltages it is also obvious that the interference pattern becomes more 'dense'.

By counting the number of fringes we deduced the following:

- the maximum displacement of the central pad versus the applied voltage, given in Figure 6.12.
- the profile of the membrane shape given in Figure 6.13. and

- the effective focal length of the mirror was found to be $f_{\text{eff}} = 3.5$ m.

The last image in each of Figures 6.8-6.11 gives simulated mirror surface for the maximum voltage applied i.e. how the shape of the DMM is deformed corresponding to the latest interference pattern. The software was available within the University and it calculates the number of fringes and the membrane deformation when a known tension is applied to the mirror. The tension was initially evaluated by matching the interference patterns measured by the interferometer with that given from the software [167].

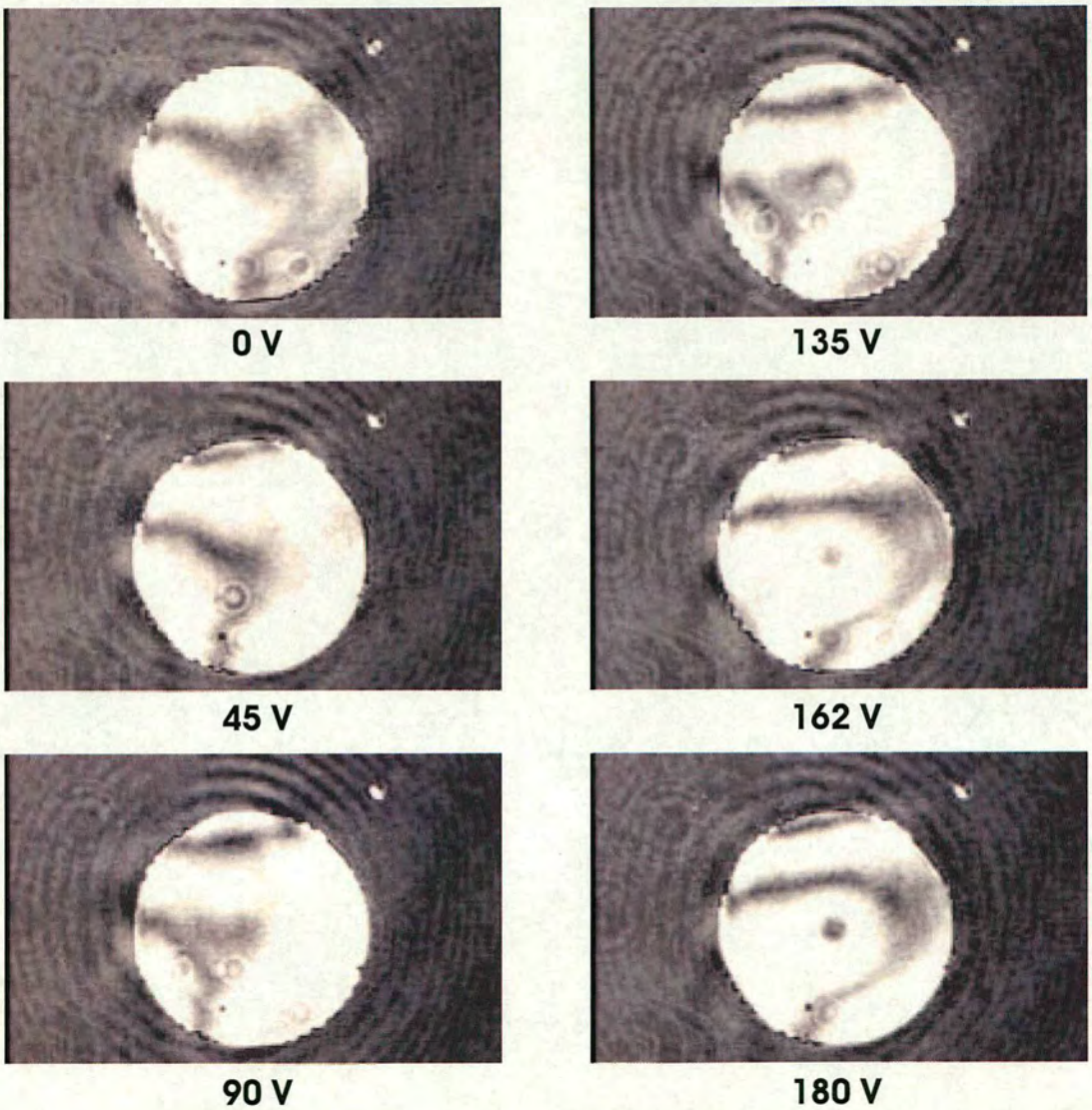

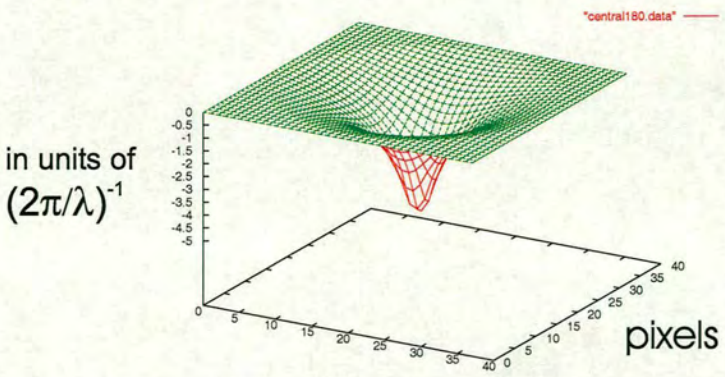

Figure 6.8: Interference pattern when voltage is applied to the central pad.

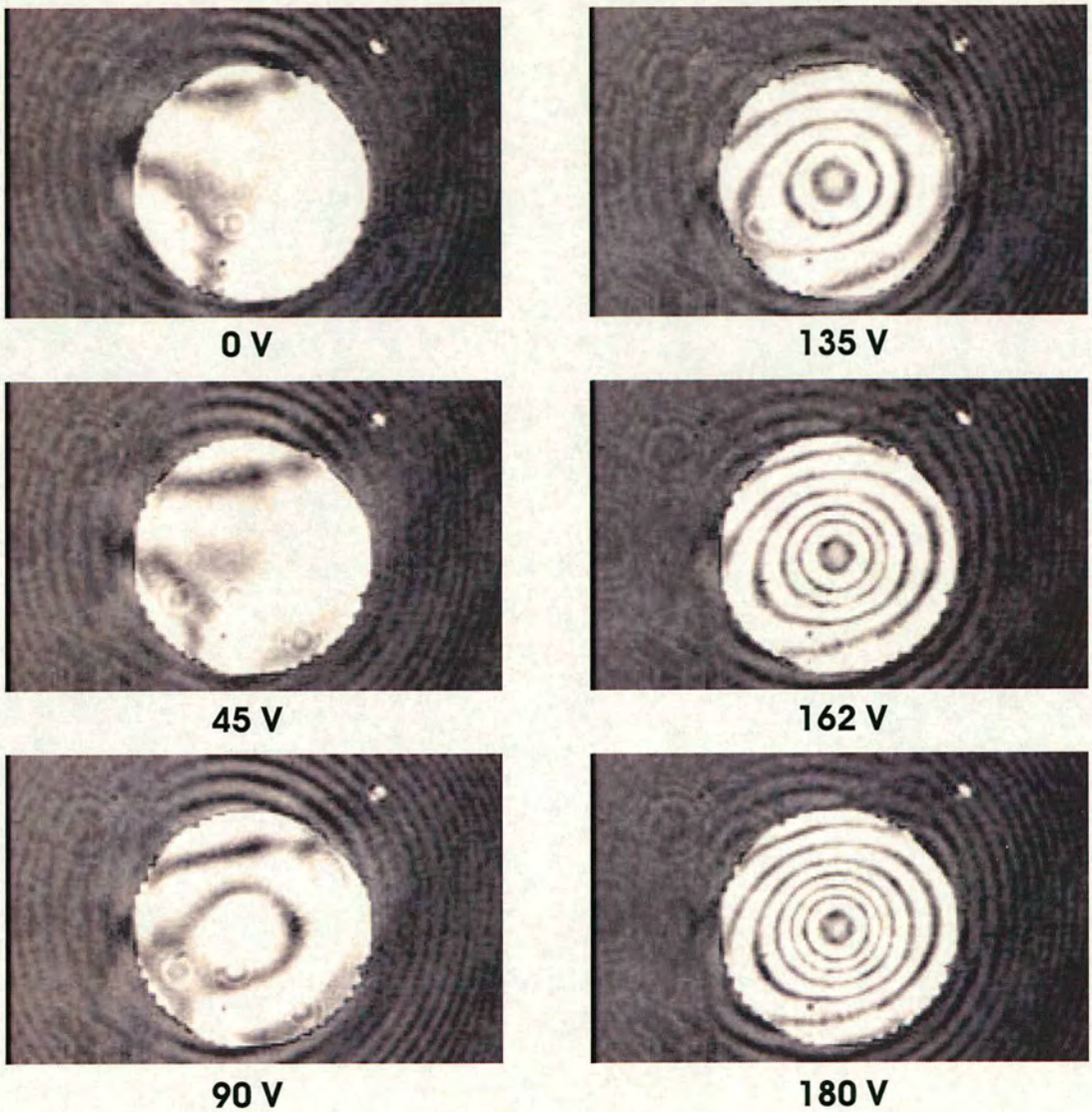

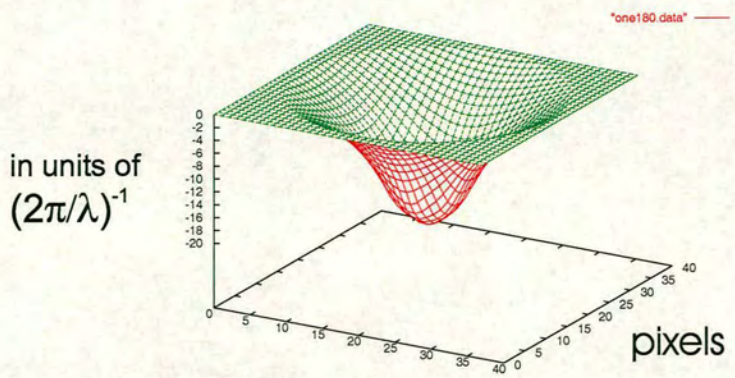

Figure 6.9: Interference pattern when voltage is applied to the central pad and first ring.

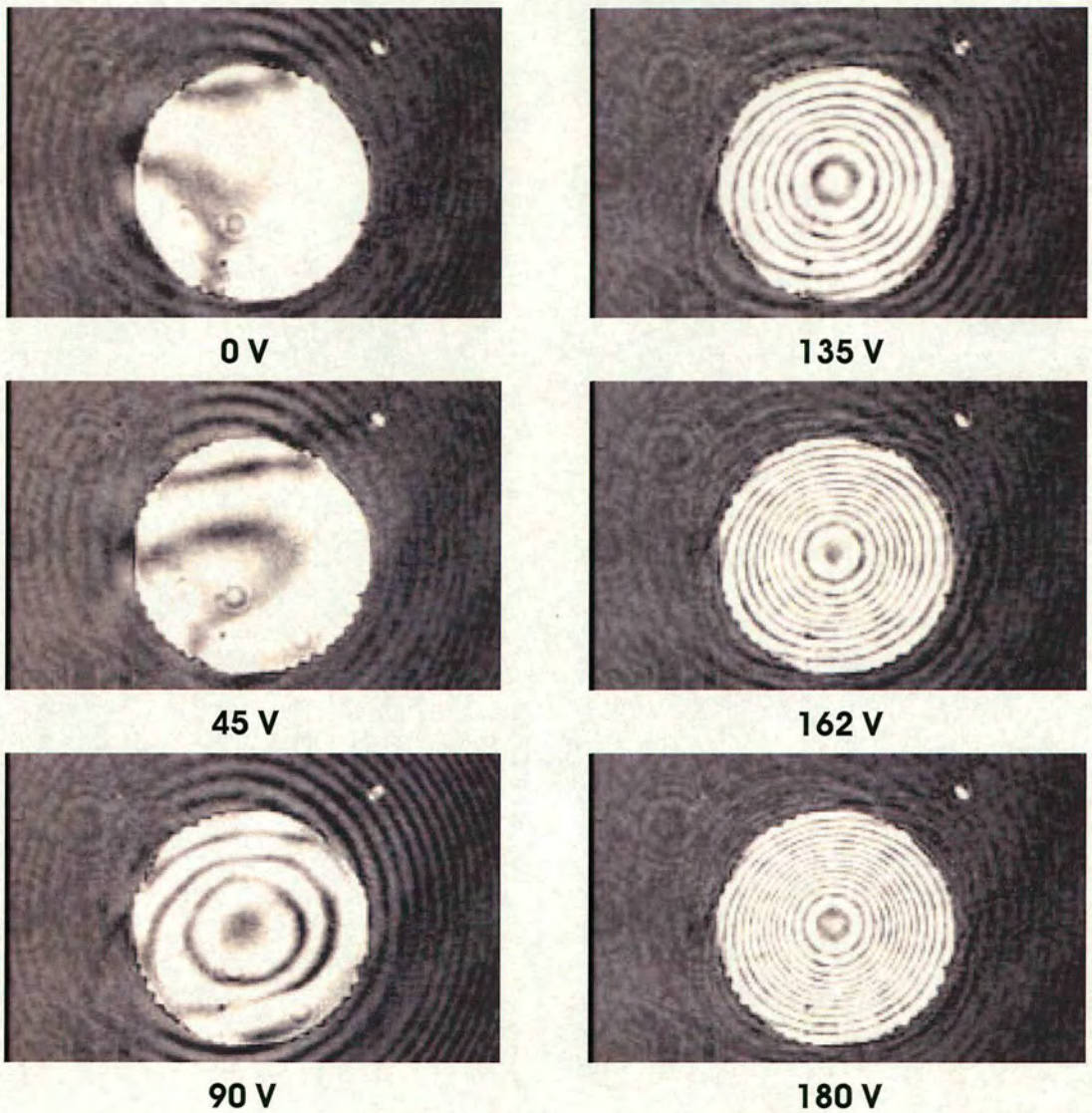

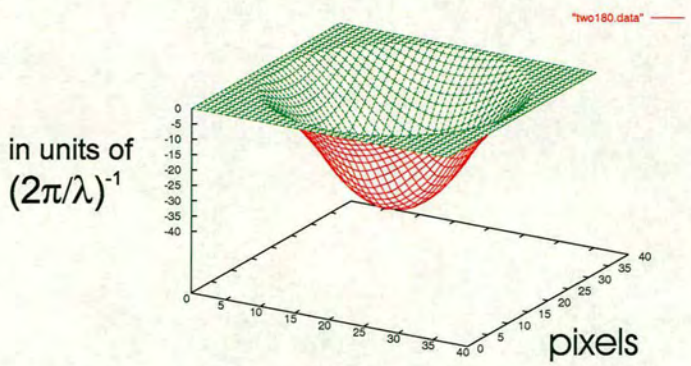

Figure 6.10: Interference pattern when voltage is applied to the central pad, first and second rings.

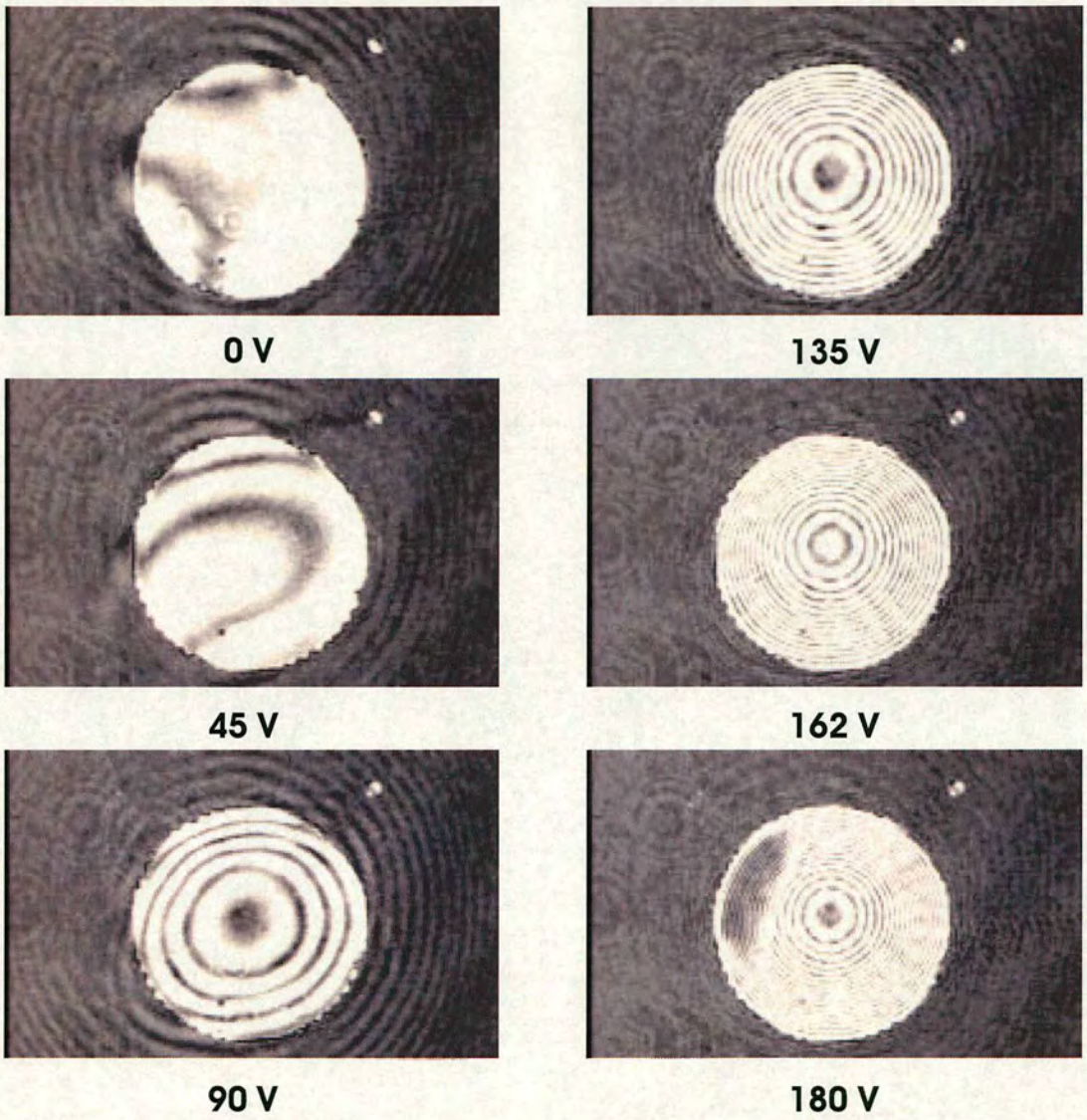

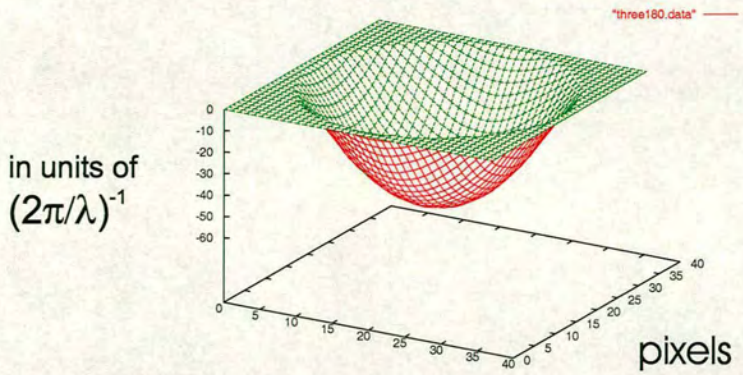

Figure 6.11: Interference pattern when voltage is applied to all actuators.

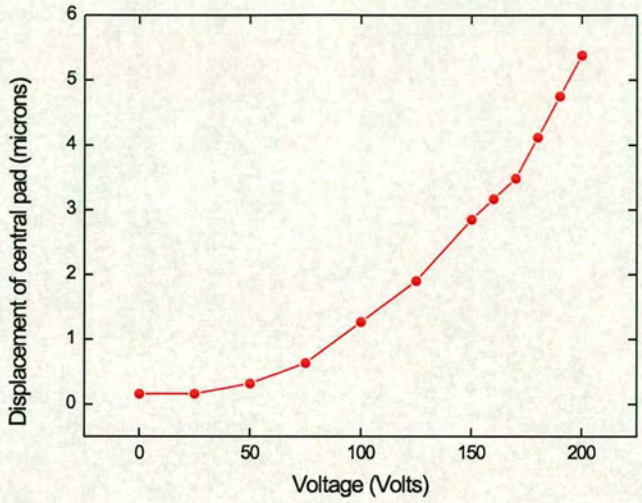

Figure 6.12: Central displacent in terms of voltage when all rings were set to the same voltage.

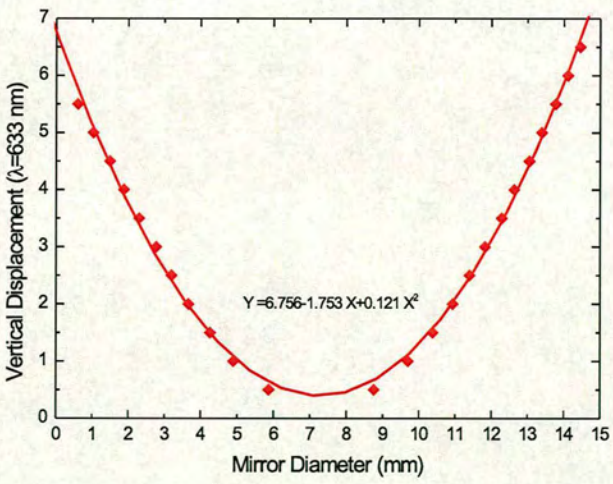

Figure 6.13: Profile of the shape of the membrane when all electrodes are undergoing the highest voltage (180 V).

6.4 Experiment 1: Moving the Trapped Particle Along Z-axis

The experimental setup combines inverted optical tweezers with adaptive optics as shown in Figure 6.14. The adaptive optics component used is a deformable membrane mirror as described in a previous section. In the first experiment a Gaussian beam from a He-Ne laser running at a power of 35 mW was initially expanded using two lenses, with focal lengths f_1 = 40 mm and f_2 = 160 mm respectively. Since the estimated effective focal length of the mirror was 3.5 m the DMM had to be placed at that distance away from the back aperture of the microscope objective. The beam path was folded by several mirrors. Before the objective, another pair of lenses with the same focal length $f_3 = f_4$ = 100 mm was used as the relay system.

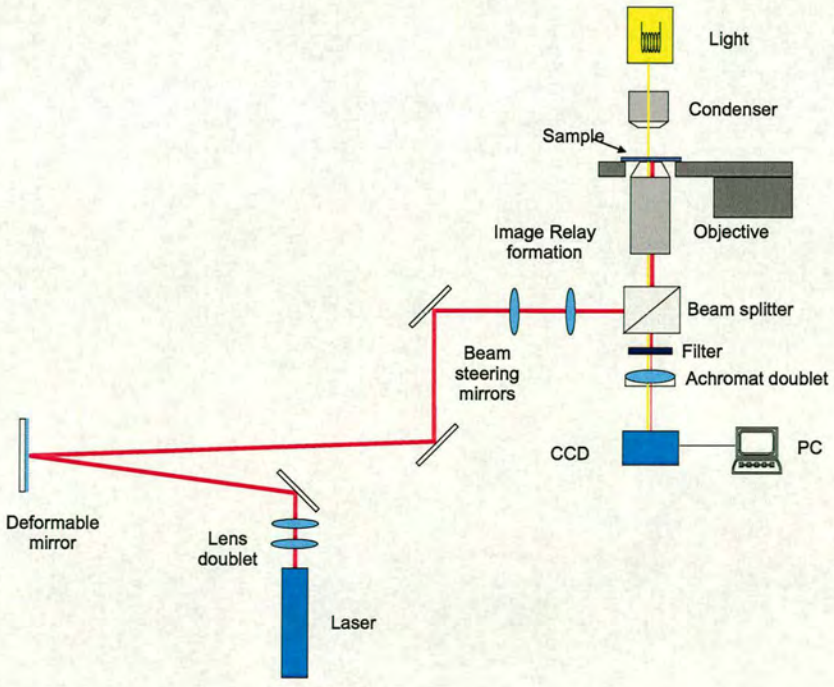

Figure 6.14: Schematic diagram of the tweezers setup used to defocus the laser beam and move the bead in z-axis.

The idea of the experiment was to capture a bead and move it deeper into the sample while defocusing the laser light by applying voltages to the DMM. After a bead was trapped, increasing voltages were applied to the central and all concentric rings electrodes which yielded in the movement of the trapped particle. It was observed that the bead escaped the trap at a voltage of 140 V. Figure 6.15 shows three different snapshots of the movie captured with the corresponding voltages applied to the DMM.

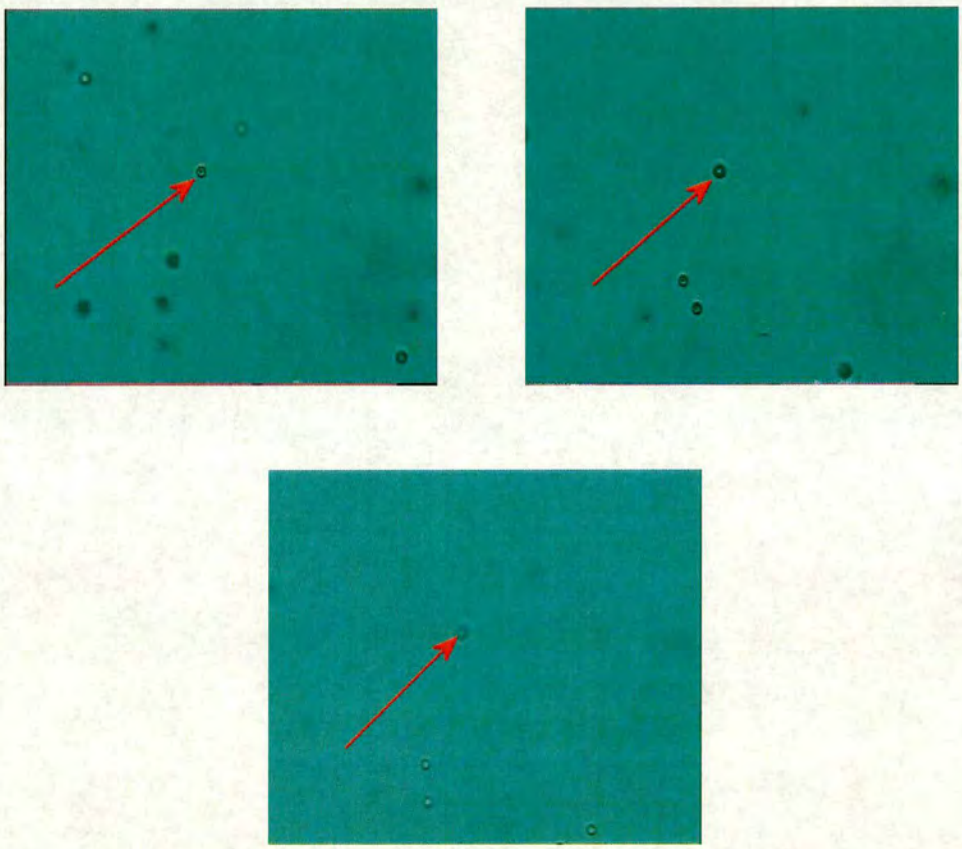

Figure 6.15: Snapshots while the trapped bead is moving deeper into the sample. The three images correspond to 0 V, 90 V and 130 V (just before the bead escaped the trap).

In order to identify how deep the trapped bead moved, the brightfield images of a bead attached to the glass surface were recorded. Figure 6.16 gives these images while the microscope objective was moved in the vertical direction. By comparing the size of

the trapped bead with the size of the 'stuck' bead we estimated that the bead moved about 2 μm at 140 V [168].

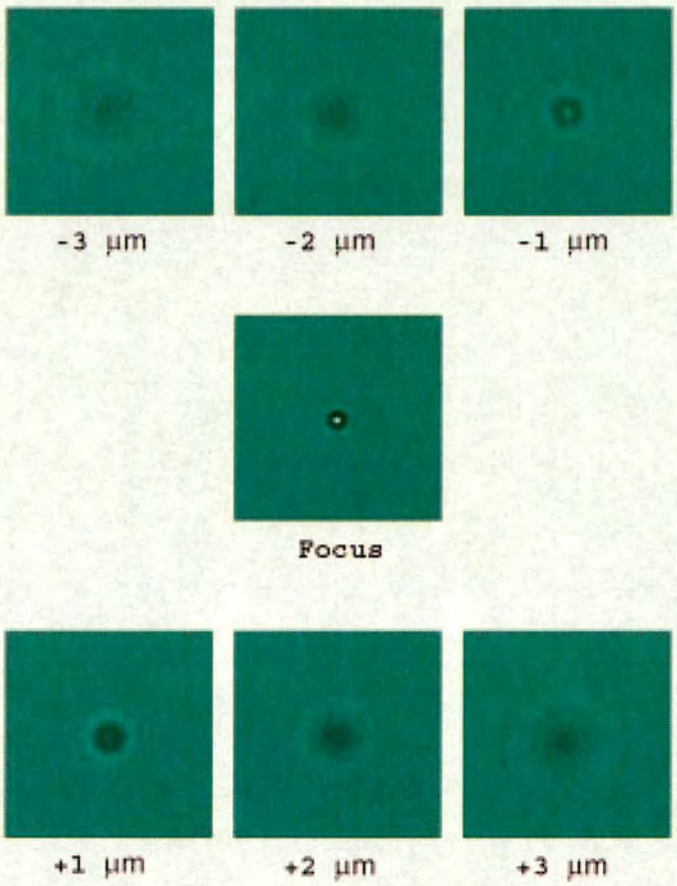

Figure 6.16: Brightfield images of a bead stuck on the glass surface while the focus of the microscope objective changes. The minus sign gives the images of the bead as the objective moves out of the focus towards the coverslip, while the plus sign signifies depths deeper into the sample.

The performance of the axial movement of the particle could be further improved by using another laser with higher power in order to enable stronger trapping and also change the relay lenses system in order to decrease the beam diameter and match the back aperture of the microscope objective better, but we did not persue this experiment.

6.5 Experiment 2: Correcting Spherical Aberrations

In the second experiment the set up was slighly changed and the deformable membrane was used for aberration correction. Figure 6.17 gives a schematic diagram of the setup.

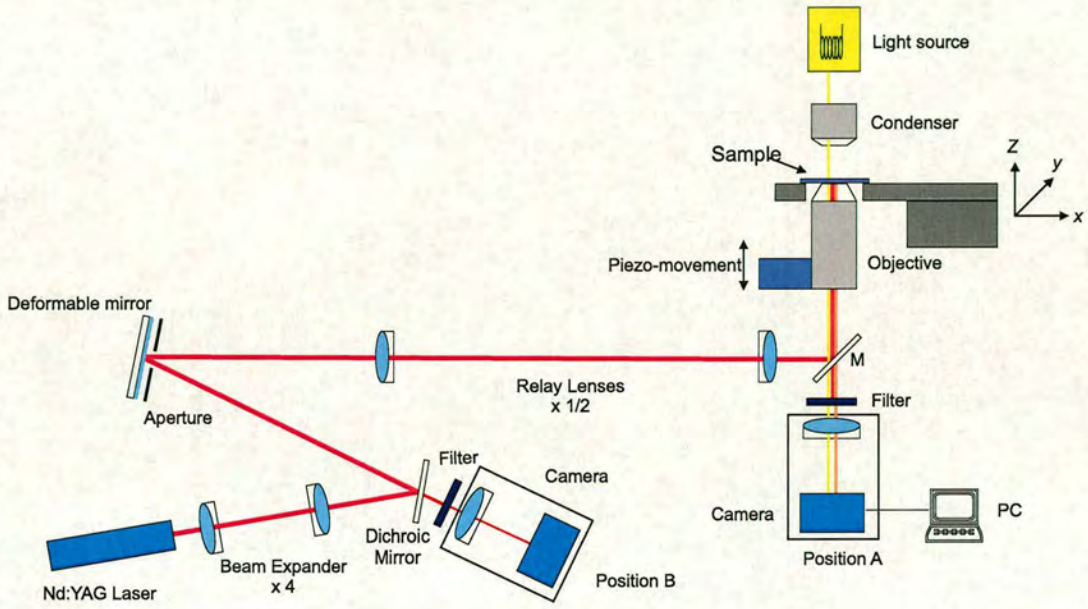

Figure 6.17: Schematic diagram of the tweezers setup. The red line gives the laser optical path, the yellow the brightfield illumination and the orange the two photon excitation.

A beam from a Nd:YAG laser at a wavelength of λ = 1064 nm was initially expanded with a telescope f_1 = 40 mm and f_2 = 160 mm . The selection of the focal lengths was based on the fact that the initial diameter of the beam was 4 mm and it had to be expanded by 4 times in order to match the size of the deformable membrane mirror ($\approx$ 15 mm in diameter). A second telescope f_3 = 250 mm and f_4 = 140 mm was used to match the beam size to the exit pupil of the microscope objective ($\approx$ 6.5 mm in diameter) and make its back focal plane conjugate to the DMM. The beam was then reflected off a dichroic mirror (M) at the back aperture of a high numerical aperture oil-immersion objective, mounted on a piezotranslator which allowed a precise adjustment

of the focal plane.

The samples consisted of orange fluorescent polystyrene spheres with a diameter of 1 μm (FluoSpheres F-8820, Molecular Probes Inc., Eugene) suspended in distilled water. The excitation wavelength of the beads (540 nm) was the appropriate for two-photon fluorescence excitation from the Nd:YAG laser. The two-photon fluorescence signal (having a peak emission at 560 nm), emmited from the trapped bead, was strong enough to be detected with a standard CCD camera.

The CCD images were acquired at video frame rate (25 Hz) using a frame grabber card. A LabView program was used to calculate the total fluorescence intensity, the standard deviation and the peak intensity in real time as well as to monitor the piezo movement. The program also generated the feedback signal that was used to optimise the shape of the DMM in order to compensate for the aberrations introduced by the interface.

In this experiment a bead was trapped at the focal position of the microscope objective and the focus was changed by moving the piezotranslator. At each focal position the total fluorescence intensity is approximately proportional to the square of the intensity in the laser focus, consequently it provides a very sensitive measure of the depth of the optical trapping potential.

When the total fluorescence intensity was used as the feedback signal for the DMM, it was found that the trap was moving out of the image plane closer towards the interface instead of getting optimised for the given focal plane of the objective. By shifting the focus closer to the interface aberrations were reduced and the fluorescence signal increased. The method of addressing the DMM in such a way that only its spherical aberration is varied without changing the defocus [169, 170] requires careful characterisation and calibration of the DMM and correction is limited to this one single aberration.

An easier method was to maximise the standard deviation of the fluorescence signal

providing a combined measure for intensity and sharpness of the fluorescence emission. The optimisation was performed by placing the camera in two different positions. Initially the camera was close to the objective (position A) as in any *standard* setup. However, the same aberrations that degrade the quality of the laser focus, also affect the quality of the image in a similar way. If the camera was mounted behind the DMM (position B), the quality of the image and consequently the overall trapping performance of the tweezers was significantly improved.

6.5.1 Results

Initially, the effect of spherical aberrations on the fluorescence signal for a standard optical tweezers setup (i.e. no voltages on the DMM and camera in position A) were examined. For all subsequent figures the x-axis gives the nominal focal position (NFP) which corresponds to the trap position as it is directly read from the piezo translation. In this experiment the distance between cover glass and actual focal point was about $n_{\text{water}}/n_{\text{glass}} \approx 87\%$ of NFP (see equation 6.2).

Figure 6.18 shows the decrease of fluorescence intensity while the laser focus was moved deeper into the sample. In this way the measured two-photon fluorescence signal gave a clear evidence of the drop in the trapping potential as the trap was moved deeper into the sample. Photobleaching was found to be negligible even when the sphere was trapped for more than 10 min and the absolute fluorescence intensity showed insignificant variation for different trapped spheres within the sample. Therefore, the total fluorescence intensity provides a measure of the absolute z-position of the trap within the sample, for this aberrated system.

By looking at the bright field image of the trapped sphere Figure 6.19, it was observed that the sphere moved out of the focal plane (in the direction of the beam propagation) as the trap was moved deeper inside the sample. Both of these findings are consistent

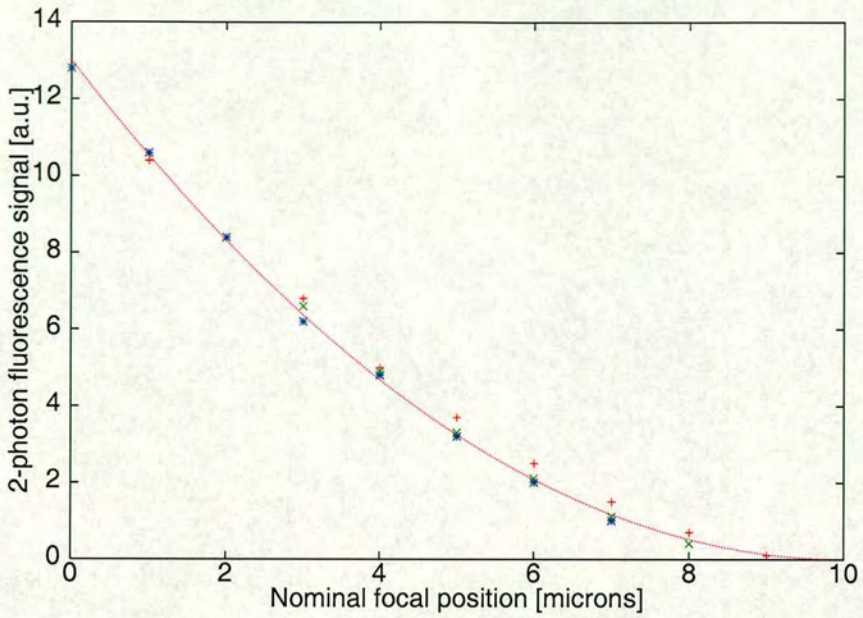

Figure 6.18: Fluorescence intensity of the trapped bead vs the position of the trap. Different signs correspond to different iterations.

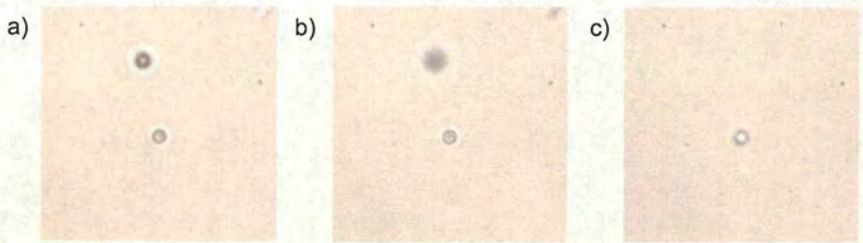

Figure 6.19: Brightfield image of a trapped sphere for different nominal focal positions: a) 1 μm, b) 4 μm, c) 8 μm. The trapped particle (in the centre of the image) moves away from the image plane in direction of beam propagation as the NFP is increased.

with recent theoretical investigations [156, 154] as well as recent experimental results [158, 159] obtained by different experimental methods.

Subsequently, the fluorescence intensity was measured using two different approaches: (i) by changing the relay lenses telescope and (ii) by applying voltages to the DMM.

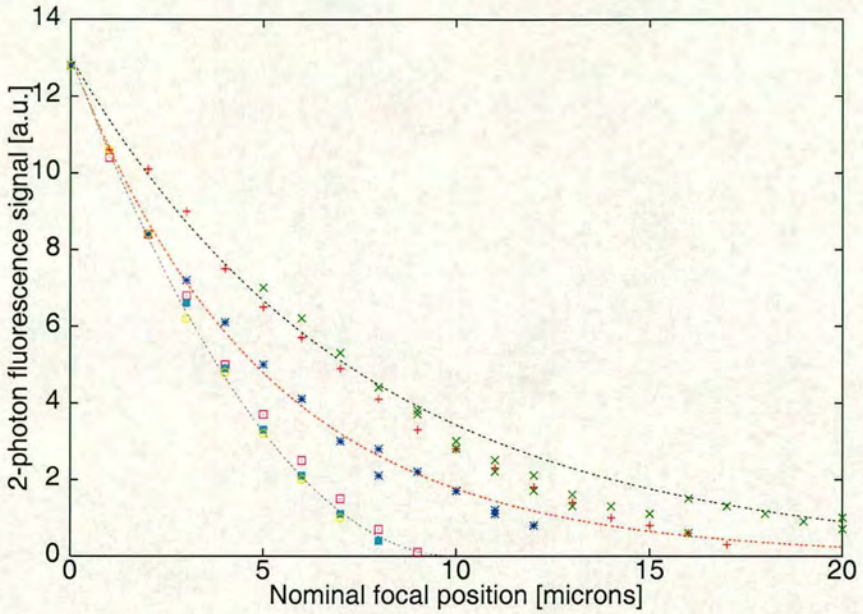

Figure 6.20: Fluorescence intensity of the trapped bead versus the position of the trap: (a) left curve, in the typical tweezers setup, (b) middle curve, when the telescope lenses were moved apart and (c) right curve when DMM is used.

In the first case a bead was trapped at an initial NFP having the relay lenses positioned at a distance f_3+f_4 and with the DMM flat. Then by moving the second lens towards the microscope objective we identified the position at which the peak fluorescence intensity was maximised. The whole procedure was repeated for different NFP until trapping was not achieved anymore. As seen in Figure 6.20 it was feasible to achieve trapping positions as far as 12 microns into the sample.

In the second case, the DMM was used in order to correct the spherical aberrations introduced by the refractive-index mismatch. The camera was still in position A and the relay lenses remained at a constant distance f_3+f_4. A trapped sphere was initially moved a certain distance into the sample using the piezo translator and then the standard deviation of the fluorescence signal was optimised by applying voltage to all 37 electrodes of the DMM. A basic optimisation algorithm was used which iteratively

changed the electrode voltages in small increments (typically 5 % of the maximum permissible voltage), in order to ensure that the focus quality did not change too abruptly within one iteration. The more sophisticated generic algorithms used to great success elsewhere (e.g. [171]) were not suited to our system since the trapped bead often escaped if the focus was changed too suddenly. The experimental results shown in Figure 6.21 give clear evidence that the fluorescence intensity drops off more slowly than in the two previous cases. For any given fluorescence intensity (and therefore trapping potential) the trap can now be moved about 1.7 times deeper into the sample, thus almost doubling the achievable trapping depth for a given laser power.

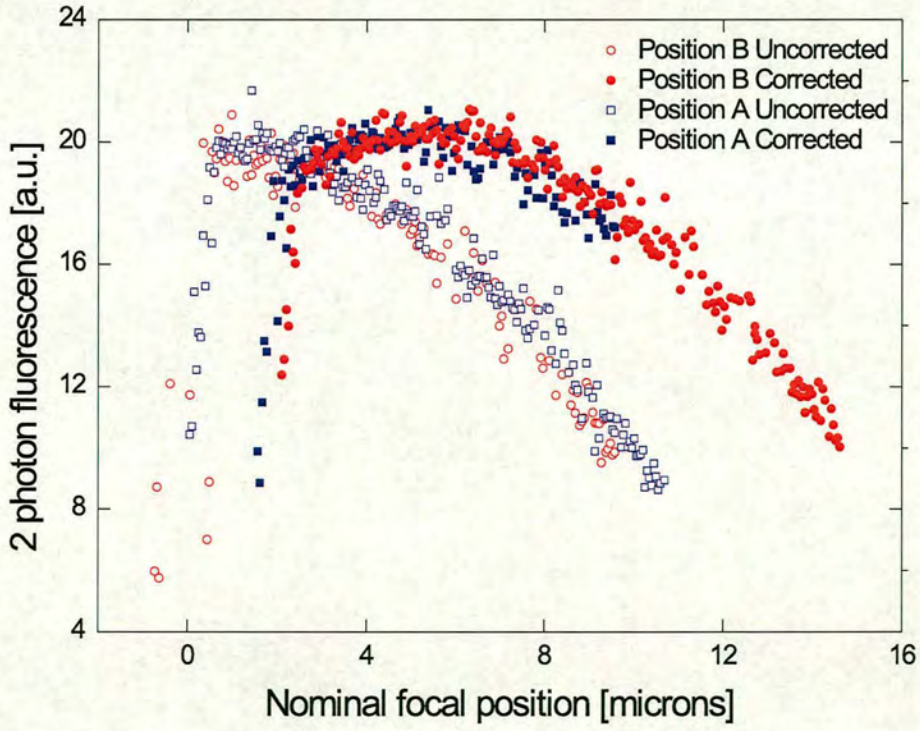

Figure 6.21: Fluorescence intensity for the two camera positions for the aberrated and corrected cases.

It has to be noted that the DMM cannot correct the aberrations completely as the signal still dropped with increasing depth. This happened because the detection of the fluorescence signal also suffered from aberrations which remained uncorrected in the current system. For this reason, the camera was moved to position B, so that the DMM also improved the image quality. Figure 6.21 shows the initial experimental results for the two different camera positions both in the aberrated and corrected case.

It is obvious that the fluorescence intensity and therefore the trap quality was remained stable. The trap quality was kept optimal up to a depth of about 6 μm before it started to deteriorate, which seems to be in good agreement with recent experimental results using a different feedback signal [160] . As expected, the setup with camera in position B made best use of the correction that can be obtained by the DMM. Thus, the DMM was used to improve both the trap and image quality, in a similar way the objective is used in tweezers to image the sample and create the trap. Still, even in this position the DMM can not compensate the aberrations fully, demonstrating how severe the aberrations are for very high NA objectives such as the one used in this experiment.

Figure 6.22 shows results obtained with a commercial water- immersion objective (Nikon PA 60$\times$ WI, NA 1.2) which does not suffer from spherical aberrations. This objective gives a constant fluorescence signal throughout the sample depth, clearly demonstrating that the trapping potential remaines constant inside the sample. However, it should be noted that the fluorescence intensities shown in Figure 6.22 only give a qualitative comparison between the two different objective lenses. A more quantitative comparison of the potential depth of the trap would require careful calibration, as the detected fluorescence signals strongly depend on the transmission properties of the two different objectives.

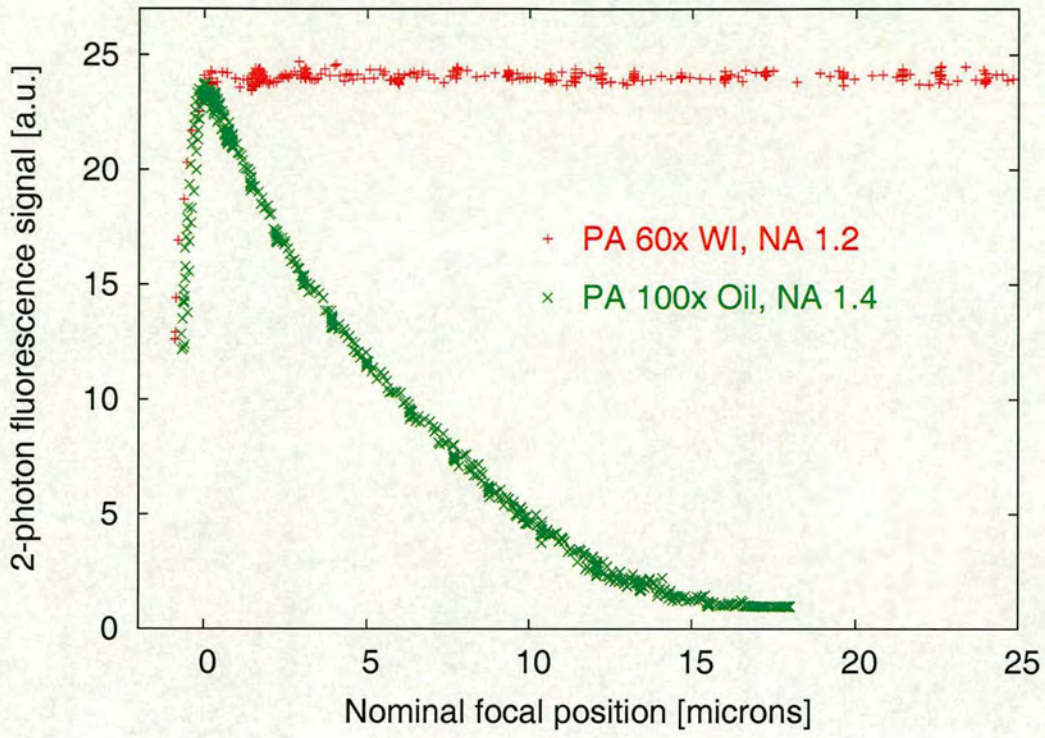

Figure 6.22: Fluorescence intensity of the trapped bead as it moved deeper into the sample, for two different objectives. For the oil-immersion objective spherical aberrations introduced by the glass-water interface cause a rapid drop in fluorescent density. The water-immersion (WI) objective shows a constant intensity since it does not suffer aberrations.

6.6 Conclusions

In this chapter a characterisation of a deformable membrane mirror was initially performed. Inverted tweezers with a high numerical aperture oil-immersion objective were used to trap polystyrene spheres suspended in water. The mirror was used initially to defocus the trapping laser beam and thus move the particle deeper into the sample for a distance of 2 μm.

Two-photon induced fluorescence was used to measure the trapping potential of such a representative tweezers setup. Monitoring this fluorescence immediately showed

the severe deterioration of the trap quality introduced by the mismatch of refractive-indices. It has been shown that a DMM enables to partially correct such aberrations, but it does not yield in the full correction throughout the sample compared to a commercial water-immersion objective. This experiment clearly demonstrated that spherical aberration has a severe effect on trap quality and it is best to try to avoid it by using the correct objective for each sample. That is, to use an objective with an immersion medium which is as close to the refractive index of the sample as possible. Only if this is not achievable DMM can offer an improvement.

For trapping out of the image plane aberrations are expected to have comparable effects on the trap quality, so correction will be important. This could be achieved either by DMM or holographic optical tweezers.

Chapter 7

Holographic Optical Tweezers

7.1 Introduction

In this chapter a ferroelectric liquid crystal spatial light modulator was implemented in an optical tweezers set up in order to form an array of gradient traps. The fast switching speed of the ferroelectric devices (compared to conventional nematic systems) was proved to enable very rapid reconfiguration of trap geometries, controlled, high speed particle movement and tweezers array multiplexing.

The most powerful and flexible approach for creating complex trapping configurations involves the use of dynamic Diffractive Optical Elements (DOE). A DOE is a component that modifies the amplitude and phase of wavefronts resulting in diffraction. Therefore, by inserting a DOE in the optical path of a laser beam one can achieve beam steering, shaping, splitting etc. Here the DOE is realised by encoding holographic patterns onto a Spatial Light Modulator (SLM)[172, 173, 174]. The method is based on computer-generated phase-only holographic patterns for optical fanout which date back to Dammann [175] and have been extended to two-dimensional formulations by Dames [176]. Holographic elements for optical tweezers and beam shaping were first implemented by Heckenberg [177, 178] to form Laguerre Gaussian beams, and

by Grier *et al.* for multiple tweezers, initially with fixed holograms [179], and subsequently using dynamic holograms [180].

7.2 Background

7.2.1 Ferroelectric Liquid Crystal Microdisplays for Laser Tweezers Applications

Liquid Crystal (LC) is the term used to describe fluids which demonstrate a degree of order in the arrangement of their molecules. The liquid crystal molecules are rod-like with the two axis having different diffractive indices i.e. they exhibit birefringence behaviour. The most common LC used is the Nematic Liquid Crystal (NLC) where there is no positional ordering but the molecules have a preferential orientation in a way that their long axes are parallel on average. As a result, by switching the device electrically the NLC can act as a retardation plate: an element which changes the polarization of an incident beam.

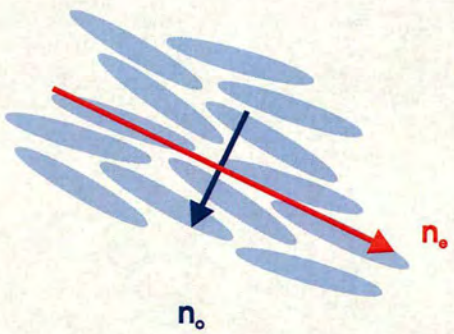

Figure 7.1: Orientation of the molecules in a Nematic Liquid Crystal, n_o and n_e are the refractive indices for the ordinary and the extraordinary rays.

A Ferroelectric Liquid Crystal (FLC) is a liquid crystal with a non-zero, permanent electric polarization called spontaneous polarization. This polarization exists without

any external field applied. In a FLC each configuration is bistable; application of a positive electric field gives one state where the negative field with the same magnitude switch to the other state. The angle at which the molecules have to switch through is called the *switching angle*, θ, and is shown in Figure 7.2.

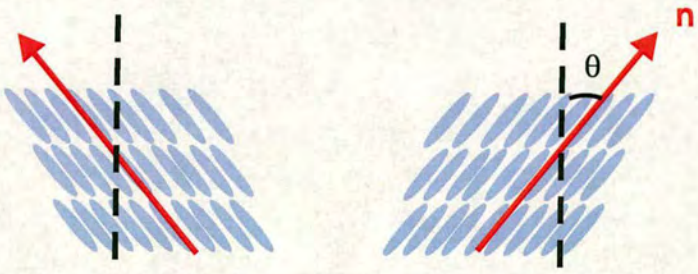

Figure 7.2: The switching of a FLC when opposite electric field is applied.

Providing that the energy given to the molecules is enough the FLC can switch between the two different states and change the direction of the optical axis by θ. This rotation of the optical axis means that the FLC can act as a amplitude or phase modulator. In this application we are concerned only with the phase retardation introduced by the FLC. As can be seen in Figure 7.3, when polarized light encounters the FLC with its polarization axis at the bisector of the switch angle the light becomes elliptically polarized; clockwise or anticlockwise depending on the state of the FLC. Hence, when it then propagates through the analyzer it becomes linearly polarized again with a relative phase difference of π [181].

Given that the phase difference between the two waves is defined as

$$\Gamma = \frac{2\pi t}{\lambda}(n_e - n_o) \,, \tag{7.1}$$

and the transmission T as

$$T = V^2 \sin^2(\Gamma/2) \sin^2(\theta) \,, \tag{7.2}$$

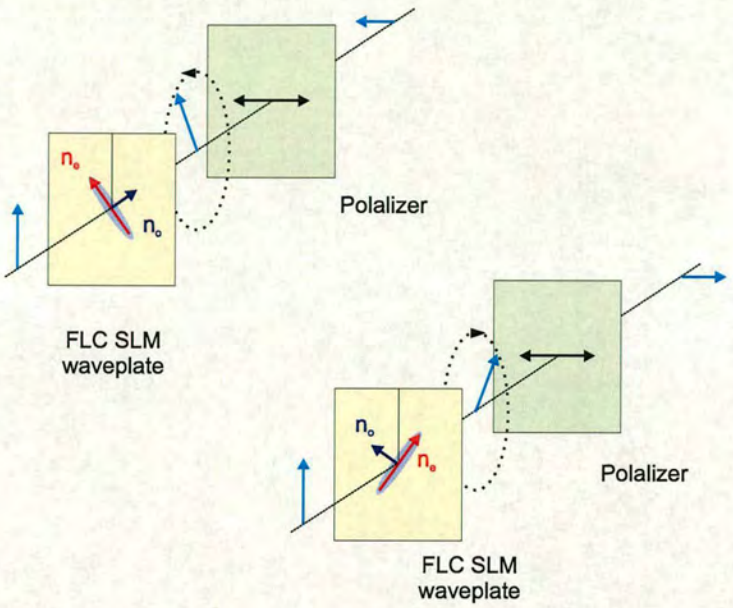

Figure 7.3: Phase modulation introduced by the FLC acting as a waveplate.

where t is the thickness of the FLC and V is the voltage of the electric field applied to the FLC, one concludes that the maximum transmission occurs when $\Gamma = \pi$ and $\theta = \pi/2$. Although this is the optimal switching angle no such device is commercially available; devices with smaller angles are now fabricated giving still pure binary phase term but also a term that adds to the undiffracted (zero) order, which can be eliminated by inserting a second polarizer (analyzer). Obviously when $\theta = \pi/2$ there is no analyzer needed since the light emerging from the FLC is going to be linearly polarized.

The differences between FLC and NLC are:

- the ability of the FLC to modulate phase and amplitude independently,
- the extremely fast switching speeds (<100 μ m/s) of the FLC compared to tens of milliseconds exhibited by the NLC.
- the multiple phase levels of the nematic while the FLC has a binary phase differ-

ence (either zero or π).

- the higher grating efficiency of the FLC.

Both the NLC and FLC can be used as diffractive optical elements; components used to modify the light wavefronts by segmenting and redirecting the segments through interference and phase control. Hence, the FLC can be used for beam splitting, steering and shaping enabling different tweezers arrays configurations.

7.2.2 Holograms

In order to acquire the desired trap configuration in the focal plane of the microscope objective one needs to reshape the incident laser beam. When a collimated laser beam goes through a lens or a hologram light is diffracted so its wavefront is modified both in terms of amplitude and phase. Since optical trapping relies on the intensity of the laser beam but not on its phase it is essential that the hologram introduces as little change to the amplitude and changes only the phase; it is a *phase hologram.* As it will be shown later the diffraction pattern formed in the objective's front focal plane is actually the Fourier transform of the holographic pattern displayed on the SLM. Since the SLM provides two phase shifts 0 and π, it follows that the phase transformation of the hologram can be $e^0 = 1$ or $e^{i\pi} = -1$, that is $\pm$ 1.

7.2.3 Fourier Optics

Figure 7.4 shows the optical system when a phase-hologram is illuminated by a collimated laser beam. The plane wave experiences a phase shift while passing through the hologram and the lens and the diffraction pattern formed in the focal plane of the lens is the Fourier tranform of the hologram. In an optical tweezers setup the lens is the microscope's objective.

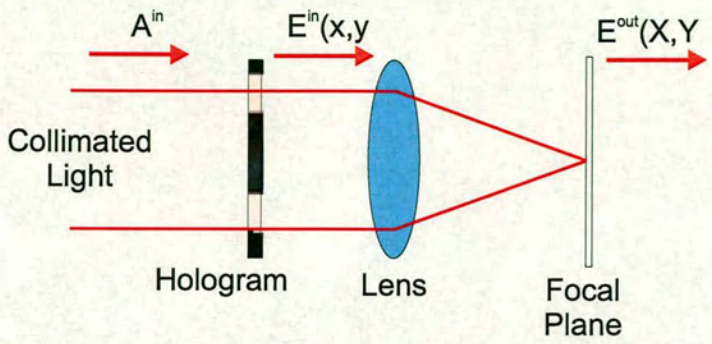

Figure 7.4: Light diffraction introduced by a phase hologram: Collimated laser beam is phase modulated by the hologram giving $E^{in}(x,y)$, then phase modulated again by the lens, to give a final diffraction pattern $E^{out}(X,Y)$ on the sample plane.

If we assume that the plane wave has a uniform amplitude A^{in} then after passing through the hologram the wave front can be described as [180]:

$$E^{in}(x,y) = A^{in}(x,y)exp[i\Phi^{in}(x,y)]\,, \tag{7.3}$$

where both the amplitude A^{in} and the phase $\Phi^{in}(x,y)$ are real-valued functions.

The wavefront of the electric field at the front focal plane of the lens is given in a similar way by:

$$E^{out}(X,Y) = A^{out}(X,Y)exp[i\Phi^{out}(X,Y)]\,. \tag{7.4}$$

These two fields are related to each other by the following equations:

$$E^{out}(X,Y) = \frac{k}{2\pi f}e^{i\theta(X,Y)}\iint dxdy E^{in}(x,y)e^{-ik(xX+yY)/f} \equiv \mathcal{F}\{E^{in}(x,y)\}\,, \tag{7.5}$$

$$E^{in}(x,y) = \frac{k}{2\pi f}\iint dXdY e^{-i\theta(X,Y)}E^{out}(X,Y)e^{-ik(xX+yY)/f} \equiv \mathcal{F}^{-1}\{E^{out}(X,Y)\}\ , \tag{7.6}$$

where $k = 2\pi/\lambda$ is the wave number of the incident light λ, f is the focal length of the microscope objective and $\theta(X,Y)$ is the additional phase introduced by the objective.

The main point of interest here is the intensity distribution $I^{out}(X,Y)$ at the imaging plane since it determines the trapping efficiency of the tweezers array:

$$I^{out}(X,Y) = |E^{out}(X,Y)|^2 = |A^{out}(X,Y)|^2\ . \tag{7.7}$$

As can be seen from the above equation the initial phase constant as well as the one due to the lens does not contribute to the final intensity.

Another interesting point is the symmetry of the diffraction pattern that arises from the fact that the Fourier transform of a real-valued function exhibits the following property:

$$\mathcal{F}(-X,-Y) = [\mathcal{F}(X,Y)]^*\ , \tag{7.8}$$

hence

$$|\mathcal{F}(-X,-Y)|^2 = |\mathcal{F}(X,Y)|^2\ . \tag{7.9}$$

The above equation means that the array pattern produced by a fanout hologram, that is an amplitude division diffraction structure, is going to have symmetry around the central point (Figures 7.5 and 7.6).

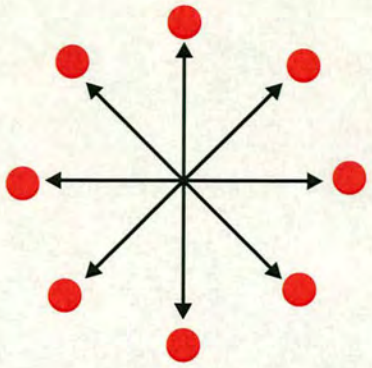

Figure 7.5: Symmetric positions of an array produced by a binary phase hologram.

7.3 Experiments

7.3.1 The SLM

The diffractive element used was the CRL Opto SXGA1-R2-H1 microdisplay [182]. This is a 1280 $\times$ 1024 reflective pixel array on a 13.62 μm pitch (centre to centre distance between adjacent pixels) switching a ferroelectric liquid crystal modulator layer. The commercial display version of this device is designed for visible light display applications with a 33° switching angle for green light at λ = 580 nm. The diffraction efficiency at each of the first order was 8 % and the liquid crystal DC balanced was achieved by inversing the image on the SLM, this being implemented in the device interface. For use as a binary phase modulator the device is placed between crossed polarizers with the the incident polarization aligned to half the cone switching angle giving an absolute phase shift of π between pixels in the two switched states [181] (Figure 7.7).

By Babinet's principle, for diffractive applications the positive and negative DC balanced frames are identical. Due to the binary phase operation of ferroelectric devices, the arrangement of tweezer traps always form a centro-symmetric pattern.

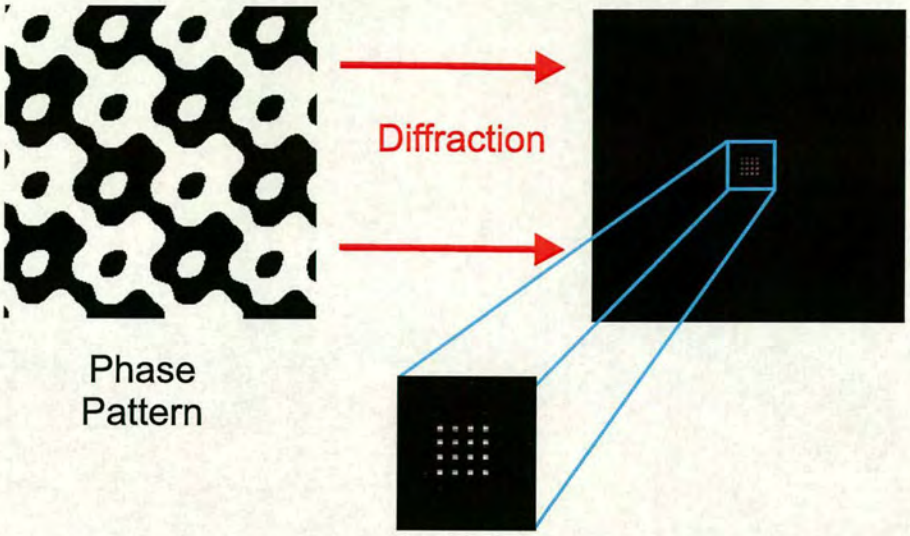

Figure 7.6: The fanout hologram.

A ferroelectric device displays only binary images, for display applications, colour images are built up by colour sequential temporal multiplexing synchronised with the light sources. The device is driven from a PC through a Digital Video Interface (DVI) with 24 bit colour images at 60 Hz (Figure 7.8).

For our purposes this means 24 different bit-planes are available in each 60 Hz time slot giving a binary image refresh rate of 1440 Hz. To use effectively such high refresh rates the diffraction patterns must be sent to the device at comparable rates. We have used two techniques to take advantage of the ferroelectric liquid crystal speed in optical tweezer applications.

1. *Non-Multiplexed Hologram.* The same binary pattern is in all 24 bit planes:

   (a) The patterns are a series of pre-calculated images stored in PC memory and flashed out to the SLM through the video link. The refresh rate is PC dependent but rates of > 10 images/s are generally achieved on a standard PC.

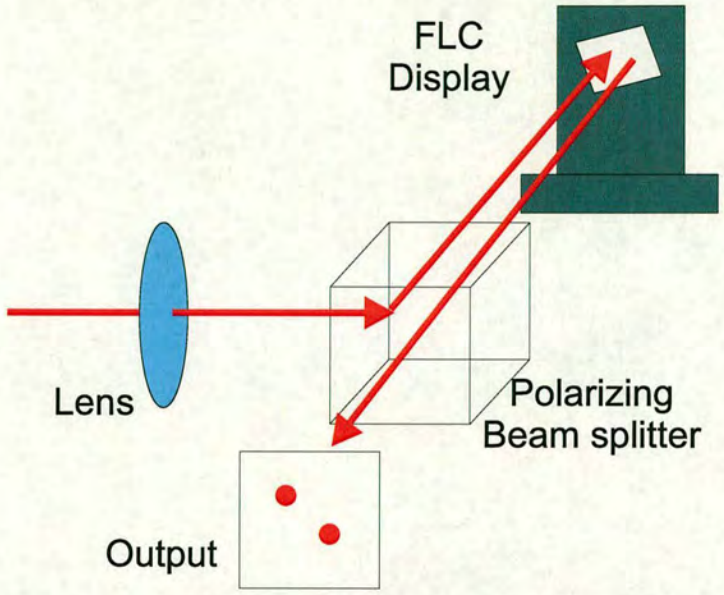

Figure 7.7: Typical configuration for binary dynamic phase operation.

(b) For some diffractive patterns which can be described as vector structures (gratings, diffractive lenses, Dammann gratings) the patterns can be drawn as vector patterns and manipulated (rotated, shifted, scaled causing the trap position to move accordingly) using the hardware accelerated video routines of the video card. With this technique rates of > 30 images/s have been obtained making real time control of trap position possible

2. *Multiplexed Holograms:* Different diffractive patterns can be loaded into the different bit-planes which are then displayed in order by the microdisplay interface. This allows 24 different holograms to be displayed sequentially within one 60 Hz video frame. Due to the high update speed the optical laser power is shared equally between the 24 holograms. Again, the whole pattern can be updated as for the *non-multiplexed hologram* mode, allowing a highly flexible dynamically programmable diffractive device.

The system control software runs under Linux/KDE on a standard PC with a Matrox

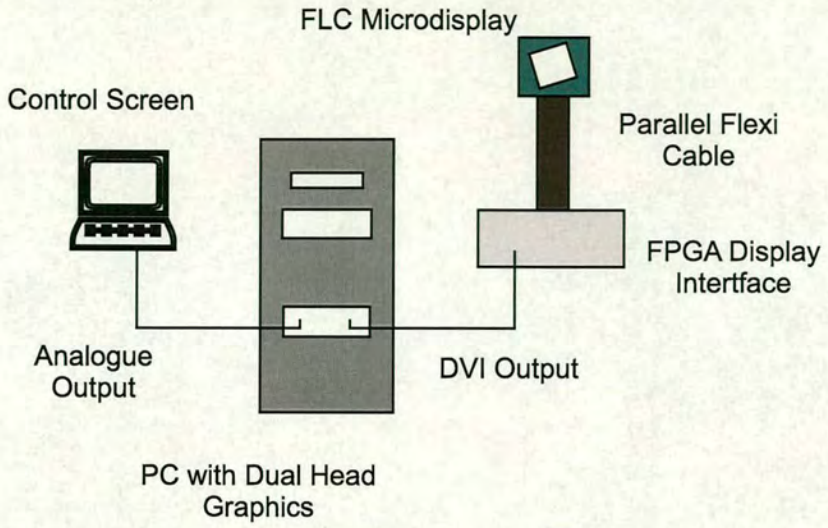

Figure 7.8: Computer interface.

G550 dual-head video card enabling the diffracting pattern data to be sent to the SLM video port and controlled from a user interface on the monitor port. The software uses *OpenGL* routines to access the video hardware acceleration.

7.3.2 Optical Setup

The optical setup used for the holographic optical tweezers was again based on a home-built open microscope with an inverted geometry. Figure 7.9 gives a schematic diagramme of this setup. A collimated beam from a red Kr^+-ion laser is initially expanded by means of a microcope objective, a pinhole for spatial filtering and an achromat doublet with focal length $f = 160$ mm. With that configuration the beam was expanded by ten times its initial size and it enables the illumination of a circular area of the microdisplay approximately 1000 pixels (11 mm) in diameter. The polarizing beamsplitter acts as the analyzer giving pure binary phase modulation.

A pair of achromat lenses with focal lengths $f_1 = 250$ mm and $f_2 = 120$ mm formed

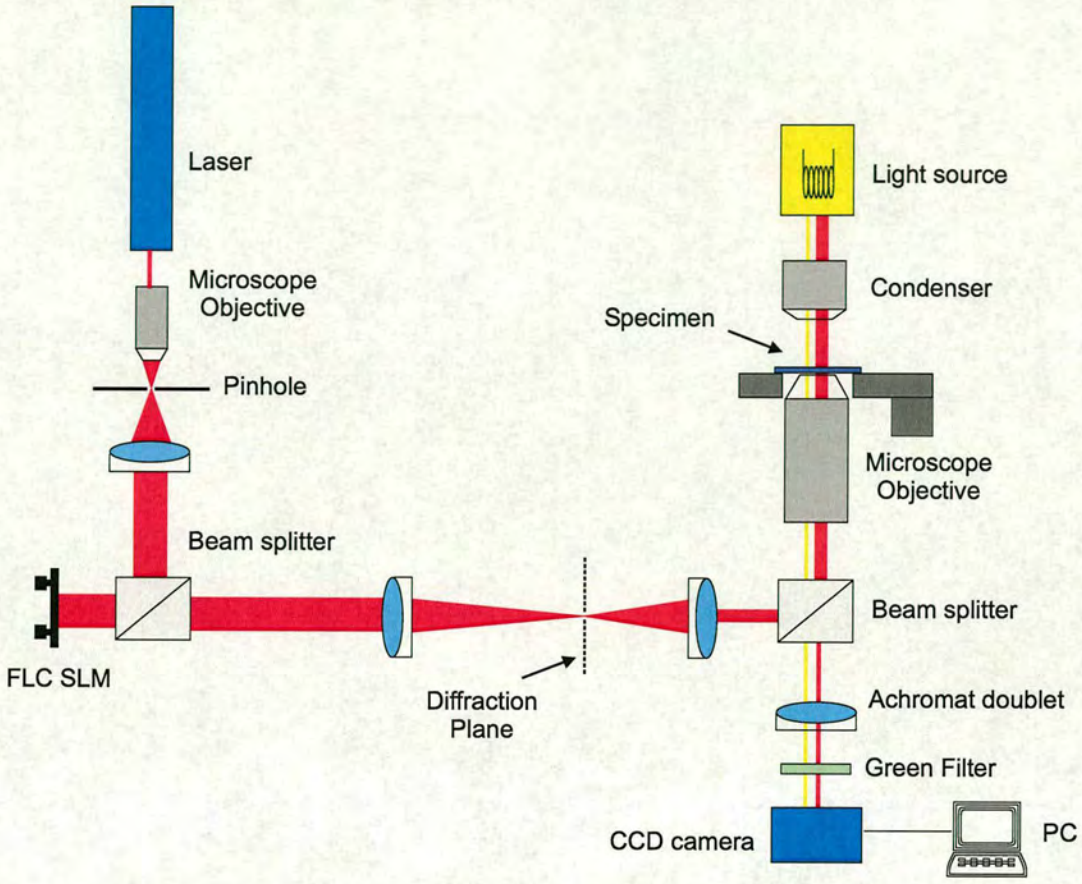

Figure 7.9: Schematic diagramme of the holographic optical tweezers setup.

a 4f imaging system which resulted in a projected image at the back focal plane of the microscope's objective. The size of the projected image was demagnified by 0.48 times in order to much the size of the back aperture of the objective. The second polarizing beamsplitter placed in the optical path of the microscope was oriented in a way to transmit the maximum possible power of the tweezer illumination, being 95 %. The microscope objective is a Nikon 100×, 1.4 NA, oil objective with a back exit pupil of 6.5 mm with bright field imaging to a video camera giving a field of view of 40×60 μm.

With this optical layout, a binary grating on the input microdisplay of 12 pixels pitch

gives a first order diffraction spots at $\pm$ 20.8 μm using He-Ne illumination; the full field of view of the objective. The sample used throughout this section was 1 μm polystyrene spheres suspended in distilled water and it was placed between two microscope cover-slips being separated with a double adhesive tape.

7.4 Results and Discussion

7.4.1 Non-multiplexed Hologram Results

Figure 7.10 shows a 4-by-4 tweezers array on a 5 μm pitch. The holographic pattern was calculated using the iterative techniques proposed by Dames [176] in which a 128×128 pixel pattern was sent to the microdisplay. Initial trapping of the spheres was achieved using a Kr^+ laser power of 700 mW. By gradually lowering the laser power it was found that all beads remained stably trapped with power as low as 300 mW; giving an estimated input requirement of approximately 43 mW per trap.

Based on these observations from the static experiments, and taking into account that the incident power damage limit of the device is 4 W, it was estimated that the maximum number of usable traps that could be created with the given commercial device is 90; which is comparable with results obtained from nematic devices.

In order to achieve movable traps, binary gratings described as *OpenGL* vector objects were sent to the device . This enabled real-time scaling and rotation of the pattern using the built-in graphics acceleration hardware. Strong traps were formed with approximately 50 mW input power per trap from the Krypton laser. Motion was obtained by scaling or rotating the gratings to move the trap. Results are shown in Figure 7.11.

The maximum speed obtained for stable traps with the current graphics hardware was 35 μm/s while rotating two traps in a 10.5 μm diameter circle by rotation of the grating in 12° steps using 700 mW of laser power which corresponds to approximately 32

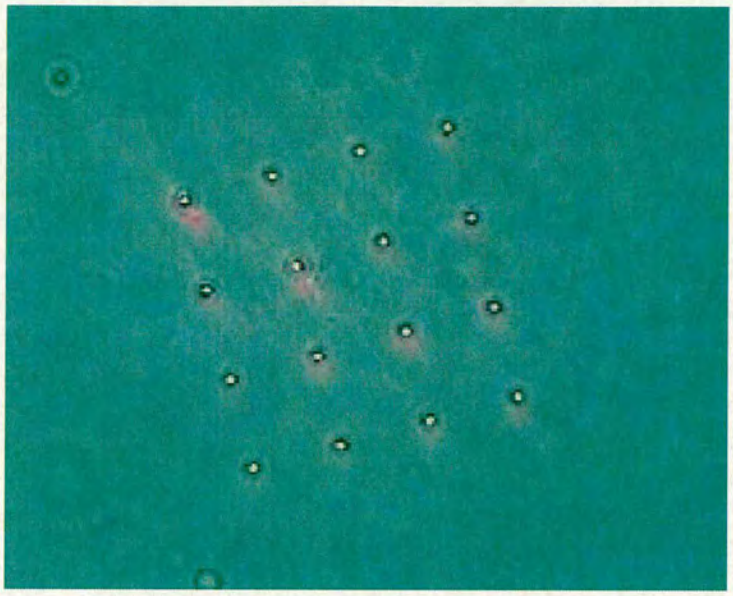

Figure 7.10: Still image of the 4×4 trapping array. Movie can be found at http://www.cosmic.ed.ac.uk/movies/tweezers/holographic/4x4array.avi .

scaled frames per second with approximately 1.1 μm distance between successive trap positions. Higher speeds, achieved by increasing the angle step and thus separation between successive traps, resulted in beads escaping the traps. This loss was probably due to the Stokes drag limit which is $\approx$ 1 pN for the speeds used and it is comparable to the trapping force for the laser power used. This drawback could be overcome by using higher laser power.

The video hardware is operating at half the operation speed of the microdisplay which operates at 60 Hz, so giving the system a potential trap movement speed in excess of 66 μm/s with the current step size. Using a nematic device the maximum demonstrated trap movement speed is 2.5 μm/s [183] and the maximum proposed is 10 μm/s [184] for 1 μm polystyrene beads.

Figure 7.11: Still image of the moving dual trap. Movie can be found at http://www.cosmic.ed.ac.uk/movies/tweezers/holographic/fast-speed.avi .

7.4.2 Multiplexed Holographic Trap Geometries

The most powerful feature of holographic optical traps based on ferroelectric devices is the possibility of multiplexing trap landscapes to enhance flexibility and functionality of the arrays. Here the fast-switching property of the ferroelectric device is deployed not only to move particles rapidly but to time-share between geometries. Here we illustrate the operation by partitioning the output of the 24 bitplane device to create a multiplexed configuration comprising independent static and dynamic arrays.

Specifically, a linear 5×1 static array of traps was formed by using 16 of the 24 bitplanes (denoted as the "red" and "green" channels) and two movable traps by the remaining 8 bitplanes ("blue" channel). This results in the composite hologram illustrated in Figure 7.12 which shows a "yellow" vertical grating to generate the 5×1 array, overlaid with the "blue" grating at 45 ° which generates the two movable traps. The optical trapping results are shown in Figure 7.13.

This resulted in a 1:2 time multiplexed split of the diffracted output. The fast-switching of the device is crucial for robust operation because the timescale over which the mul-

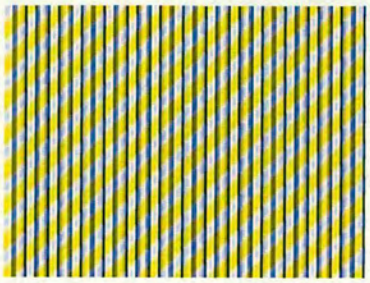

Figure 7.12: Composite hologram for 5 × 1 static hologram in "red" and "green" channels and two trap hologram in "blue" channel.

tiplexing leaves a particle unilluminated must be short compared to the particle's diffusive relaxation time which is ≈ 0.25 s for 1 μm polystyrene beads in water.

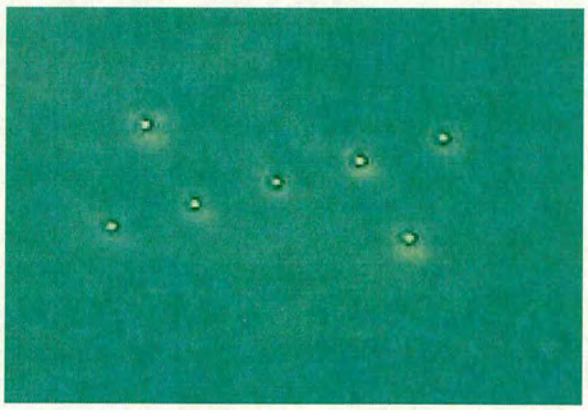

Figure 7.13: Still image showing five fixed and two movable traps formed by two-to-one multiplex. Movie can be found at http://www.cosmic.ed.ac.uk/movies/tweezers/holographic/multiplex.avi .

Due to the complex structure of the multiplexed hologram the full 24 bit images is currently calculated by using the control computer without the advantage of *OpenGL* acceleration. The required holograms were generated in real-time from a pre-calculated 5 × 1 fan-out hologram formed by the Dames [176] technique overlaid by a dynamically calculated grating with pitch and orientation controlled from an X-windows control panel. This resulted in an update rate of 3 images per second with the current 1.4 GHz PC. It is feasible with faster computer / graphics hardware and optimised

coding image to achieve rates of 10 images per second. This will be faster if the bit-level image is formed using *OpenGL* acceleration. The ultimate limit is 60 images per second determined by the microdisplay frame display rate.

Using the previous power budget of approximately 40 mW input per trap and the 4 W device damage threshold, a 4-trap dynamic hologram can be formed from each of the 24 bit-planes allowing complex dynamic patterns of up to 96 traps. A possible application of this mode is in filling the fixed traps since the movable traps can be used to 'collect' beads and move them close to the fixed trap. The movable trap can then be blanked, so allowing the bead to fall into the fixed trap array. In particular with 4 W laser illumination, 23 of the bit planes can be used for the fixed array containing up to 90 traps, and the remaining one bit-plane used to form two strong movable traps. This mode is essential for filling large fixed arrays which otherwise is a very time consuming and delicate operation.

7.5 Conclusions

In this chapter, the potential advantages of a ferroelectric liquid crystal light modulator relative to a conventional nematic device for optical trap array applications were presented. The holographic optical tweezers setup had increased trap reconfiguration speed compared to previous demontrations and furthermore it was the first time a multiplexed holographic trap geometry consisting of combinations of static and dynamic arrays was demonstrated.

Chapter 8

Conclusions and Future Work

Optical tweezers setups were constructed using home built and commercial microscopes. Optical trapping was demonstrated for the first time in the University of Edinburgh.

Optical tweezers were combined with single molecule fluorescence imaging and a flow cell to study the DNA deformation and condensation under uniform flow. It was observed that the DNA undergoes a gradual transition from a regime with strong hydrodynamic interactions at low velocities to a regime with no hydrodynamic interactions at higher velocities. Upon the DNA entrance into a spermidine-rich zone, we observed an initial rapid small contraction followed by a long latency period, which depends on the flow velocity, ionic strength and DNA length, until an abrupt and rapid collapse. The observed behaviour is due to a combination of several effects. The main phenomena are: competition in DNA binding between spermidine and the other cations (dye (YOYO-1) and Na^+) and stretching-induced spermidine-binding inhibition. To our knowledge, this is the first experimental study of the kinetics of the initiation of DNA condensation under flow.

Furthermore, the trapping technique itself was studied and instrumentational improvements with further development of the technique were investigated. A deformable

membrane mirror was used to partially correct spherical aberrations and improve the stability and strength of the optical trap. Moreover, a ferroelectric liquid crystal display was used to create an array of 4 $\times$ 4 optical traps. High translation speeds of 1 μm polystyrene beads and multiplexed holographic trapping of static and dynamic arrays were demonstrated.

Future plans for continuing the work presented in this thesis would include the combination of the biophysical experiments with the holographic tweezers technique. In order to achieve this, fluorescence imaging should be implemented in the current holographic setup. The first steps of the additions have already been made. Figure 8.1 shows the initial progress of this work. The two trap configuration was applied and DNA sample was used. Two beads were trapped and in one of them a single DNA molecule can be seen, although is not fully stretched. The image needs further improvement which involves the stabilization of the optical system and the addition of extra optical components. Also modification of the microscope is essential in order to permit proper accomodation of the flow cell and syringe pump system.

The advantage of the combination of the single molecule fluorescence imaging with the holographic optical tweezers would be the increased number of experiments that can be performed simultaneously, and the observation of interactions between DNA or other molecules. One application could be the repeat of the DNA studies like deformation and condensation, but now with an improved statistical analysis and simultaneous observation of several individual molecules while they deform or collapse. Another possible application would be the ligation of DNA; two individual molecules with complementary base pairs ends would be trapped and by using the two traps movement would come close together so they can be joined in one single molecule.

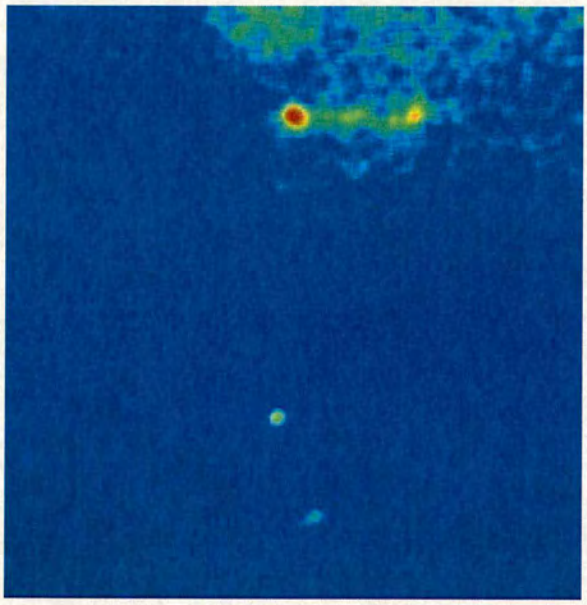

Figure 8.1: Fluorescence image of λ-DNA in the holographic tweezers setup. A second fluorescence bead is also trapped.

Bibliography

[1] A. Ashkin. *Phys. Rev. Lett.*, 24:156–159, 1970.

[2] A. Ashkin and J.M. Dziedzic. *Appl. Phys. Lett.*, 19:283–285, 1971.

[3] A. Ashkin, J. M. Dziedzic, J. E. Bjorkholm, and S. Chu. *Opt. Lett.*, 11:288–290, 1986.

[4] A. Ashkin and J.M. Dziedzic. *Science*, 235:1517–1520, 1987.

[5] A. Ashkin, J.M. Dziedzic, and T. Yamane. *Nature*, 330:769–771, 1987.

[6] A. Ashkin and J.M. Dziedzic. *Ber. Busenges. Phys. Chem.*, 93:254–260, 1989.

[7] S.M. Block, L.S.B. Goldstein, and B.J. Schnapp. *Nature*, 348:348–352, 1990.

[8] S.C. Kuo, K. Ramanathan, and B. Sorg. *Biophys. J.*, 68:S74, 1995.

[9] S.C. Kuo and M.P. Sheetz. *Science*, 260:232–234, 1993.

[10] A.D. Mehta and J.A. Spudich. *Biophys. J.*, 74:A225–A225, 1998.

[11] J.E. Molloy, C. Veigel, and A. Knight. *J. Gen. Physiol.*, 114:18, 1999.

[12] M.D. Wang, H. Yin, R. Landick, J. Gelles, and S.M. Block. *Biophys. J.*, 72:1335–1346, 97.

[13] U. Bockelmann, P. Thomen, B. Essevaz-roulet, V. Vaisnoff, and F. Heslot. *Biophys. J.*, 82:1537–1553, 2002.

[14] M.L. Bennink, O.D. Scharer, R. Kanaar, K. Sakata-Sogawa, J.M. Schins, J.S. Kanger, B.G. de Grooth, and J. Greve. *Cytometry*, 36:200–208, 1999.

[15] C.F. Schmidt, F. Gittes, M.W. Allersma, W. Mohler, and B. Schnurr. *Abstr. Par. Amer. Chem. Soc.*, 216:334, 1998.

[16] A. Knight, J.F. Eccleston, and J.E. Molloy. *Biophys. J.*, 76:A145–A145, 1999.

[17] C.T. Troy. *Phot. Spectra*, 28:30, 1994.

[18] J.W. Dai and M.P. Sheetz. *Biophys. J.*, 68:988–996, 1995.

[19] C.K. Sun, Y.C. Huang, P.C. Cheng, H.C. Liu, and B.L. Lin. *J. Opt. Soc. Am. B-Opt. Physics*, 18:1483–1489, 2001.

[20] H.D. Ouyang, M.T. Valentine, and L.E. Dewalt. *Abstr. Par. Amer. Chem. Soc.*, 212:215, 1996.

[21] A. Resnick. *J. Colloid interface Sci.*, 262:55–59, 2003.

[22] R. Aveyard, B.P. Binks, J.H. Clint, P.D.I. Fletcher, B. Neumann, and V.N. Paunov. *Langmuir*, 18:9587–9593, 2002.

[23] M. Zahn and S. Seeger. *Cell. Mol. Biol.*, 44:747–761, 1998.

[24] M.W. Berns, W.H. Wright, B.J. Trombergand G.A. Profeta, J.J.Andrews, and R.J. Walter. *Proc. Nat. Acad. Sci. USA*, 86:4539–4543, 1989.

[25] S.M. Block, D.F. Blair, and H.C. Berg. *Nature*, 338:514–518, 1989.

[26] A. Hoffmann, G.M.Z. Horste, G. Pilarczyk, S. Monajembashi, V. Uhl, and K.O. Greulich. *Appl. Phys. B*, 71:747–753, 2000.

[27] A.E. Chiou, W. Wang, G.J. Sonek, J. Hong, and M.W. Berns. *Opt. Commun.*, 133:7–10, 1997.

[28] C.G. Xie and Y.Q. Li. *J. Appl. Phys.*, 93:2982–2986, 2003.

[29] M.A. van Dijk, L.C. Kapitein, J. van Mameren, C.F. Schmidt, and E.J.G. Peterman. *J. Phys. Chem. B*, 108:6479–6484, 2004.

[30] H. Liang, W. H. Wright, C. L. Rieder, E. D. Salmon, G. Profeta, J. Andrews, Y. G. Liu, G. J. Sonek, and M. Berns. *Exptl. Cell Res.*, 213:308–312, 1994.

[31] M.E.J. Friese, T.A. Nieminen, N.R. Heckenberg, and H. Rubinsztein-Dunlop. *Nature*, 394:348–350, 1998.

[32] K. Svoboda and S.M. Block. *Opt. Lett.*, 19:930–932, 1994.

[33] H. Furukawa and I. Yamaguchi. *Opt. Lett.*, 23:216–218, 1998.

[34] E. Higurashi, O. Ohguchi, and H. Ukita. *Opt. Lett.*, 20:1931–1933, 1995.

[35] W.H. Wright, G.J. Sonek, and M.W. Berns. *Appl. Phys. Lett.*, 63:715–717, 1993.

[36] W.H. Wright, G.J. Sonek, and M.W. Berns. *Appl. Opt.*, 33:1735–1748, 1994.

[37] A.T. O'Neill and M.J. Padgett. *Opt. Commun.*, 193:45–50, 2001.

[38] Hecht. *Optics.* Addison-Wesley, 1998.

[39] S. Bradbury and B. Bracegirdle. *Introduction to Light Microscopy.* βios Scientific Publishers.

[40] S. Inoué. *Video Microscopy.* Plenum Press, 1989.

[41] O.S. Heavens; R.W. Ditchburn. *Insight into Optics.* Wiley.

[42] *Molecular Expressions, http://micro.magnet.fsu.edu/primer/index.html.*

[43] *Nikon MicroscopyU; http://www.microscopyu.com.*

[44] W. J. Smith. *Modern Optical Engineering: The Design of Optical Systems (Optical and Electro-Optical Engineering Series).* McGraw-Hill.

[45] *Nikon, TE 2000; Instructions.*

[46] J.E. Molloy and M.J. Padgett. *Contemporary Phys.*, 43:241, 2002.

[47] S.M. Block. *Noninvasive Techniques in Cell Biology; Chapter 15: Optical Tweezers: A New Tool for Biophysics.* Wiley-Liss.

[48] A. Ashkin. *Biophys. J.*, 61:569–582, 1992.

[49] K. Svoboda and S.M. Block. *Annu. Rev. Biophys. Biomol. Struct.*, 23:247–285, 1994.

[50] A. Ishijima and T. Yanagida. *Trends Biochem Sci*, 26:438–444, 2001.

[51] S. Weiss. *Science*, 283:1676–1683, 1999.

[52] C. Bustamante. *Annu. Rev. Biophys. Biophys. Chem.*, 20:415–446, 1991.

[53] B. Herman. *Fluorescence Microscopy.* βios Scientific.

[54] C.R. Calladine and H. R. Drew. *Understanding DNA: The Molecule and How It Works.* Academic Press.

[55] P.R. Bianco, L.R. Brewer, M. Corzett, R. Balhorn, Y. Yehk, S.C. Kowalczykowski, and R.J. Baskin. *Nature*, 409:374–378, 2001.

[56] R. J. Beynon and J. S. Easterby. *Buffer Solutions: The Basics.* Oxford University Press.

[57] M. J. Lang, P.M. Fordyce, and S.M. Block. *J. Biol.*, 2, 2003.

[58] J. L. Lumley. *Annu. Rev. Fluid Mech.*, 1:367, 1969.

[59] P. S. Virk. *AIchE J.*, 21:625, 1975.

[60] A. Gyr and H.-W. Bewersdorff. *Drag Reduction of Turbulent Flows by Additives*. Kluwer, Academic Publishers, Dordrecht, 1995.

[61] R. B. Bird, R. C. Armstrong, and O. Hassager. *Dynamics of Polymer Liquids*. Vols. I, II, 2nd edition, John Wiley & Sons, New York, 1987.

[62] D. V. Boger and K. Walters. *Rheological Phenomena in Focus*. No 4 in Rheology Series, Elsevier, Amsterdam, 1993.

[63] M. Doi and S. F. Edwards. *The Theory of Polymer Dynamics*. Clarendon Press, Oxford, 1986.

[64] T. Q. Nguyen and H.-H. Kausch. *Flexible Polymer Chain Dynamics in Elongational Flow*. Springer, Berlin, 1999.

[65] H. C. Öttinger. *Stochastic Processes in Polymeric Fluids*. Springer, Heidelberg, 1996.

[66] K. S. Schmitz. *An introduction to Dynamic Light Scattering by Macromolecules*. Academic Press, New York, 1990.

[67] J. S. Higgins and H. C. Benoît. *Polymers and Neutron Scattering*. Clarendon Press, Oxford, 1986.

[68] H. R. Reese and B. H. Zimm. *J. Chem. Phys.*, 92:2650, 1990.

[69] A. Keller and J. A. Odell. *Colloid Polym. Sci.*, 263:181, 1985.

[70] R. Rzehak, W. Kromen, T. Kawakatsu, and W. Zimmermann. *Eur. Phys. J. E*, 2:3, 2000.

[71] T. W. Houseal, C. Bustamante, R. F. Stump, and M. F. Maestre. *Biophys. J.*, 56:507, 1989.

[72] S. Chu. *Science*, 253:861, 1991.

[73] S. B. Smith, L. Finzi, and C. Bustamante. *Science*, 258:1122, 1992.

[74] T. T. Perkins, S. R. Quake, D. E. Smith, and S. Chu. *Science*, 264:822, 1994.

[75] T. T. Perkins, D. E. Smith, R. G. Larson, and S. Chu. *Science*, 268:83, 1995.

[76] T. T. Perkins, D. E. Smith, and S. Chu. *Science*, 276:2016, 1997.

[77] S. R. Quake, H. Babcock, and S. Chu. *Nature*, 388:151, 1997.

[78] D. E. Smith and S. Chu. *Science*, 281:1335, 1998.

[79] D. E. Smith, H. P. Babcock, and S. Chu. *Science*, 283:1724, 1999.

[80] F. Brochard-Wyart. *Europhys. Lett.*, 23:105, 1993.

[81] F. Brochard-Wyart, H. Hervet, and P. Pincus. *Europhys. Lett.*, 26:511, 1994.

[82] F. Brochard-Wyart. *Europhys. Lett.*, 30:387, 1995.

[83] P. Pincus. *Macromolecules*, 9:386, 1976.

[84] P. Pincus. *Macromolecules*, 10:210, 1977.

[85] J. Happel and H. Brenner. *Low Reynolds Number Hydrodynamics with Special Applications to Particulate Media.* Prentice Hall, Engelwood-Cliffs NJ, 1965.

[86] A. Y. Grosberg and A. R. Khokhlov. *Statistical Physics of Macromolecules.* AIP Press, New York, 1994.

[87] C. Bustamante, J. F. Marko, E. D. Siggia, and S. Smith. *Science*, 265:1599, 1994.

[88] A. Vologodskii. *Macromolecules*, 27:5623, 1994.

[89] P. J. Flory. *Principles of Polymer Chemistry.* Cornell University Press, New York, NY, 1953.

[90] J. F. Marko and E. D. Siggia. *Macromolecules*, 28:8759, 1995.

[91] R. G. Larson, T. T. Perkins, D. E. Smith, and S. Chu. *Phys. Rev. E*, 55:1794, 1997.

[92] B. H. Zimm. *Macromolecules*, 31:6089, 1998.

[93] D. Stigter and C. Bustamante. *Biophys. J.*, 75:1197, 1998.

[94] R. Rzehak, D. Kienle, T. Kawakatsu, and W. Zimmermann. *Europhys. Lett.*, 46:821, 1999.

[95] D. Kienle and W. Zimmermann. *Macromolecules*, 34:9173, 2001.

[96] P. G. de Gennes. *Scaling Concepts in Polymer Physics.* Cornell University Press, Ithaca and London, 2003.

[97] M. Rubinstein and R. H. Colby. *Polymer Physics.* Oxford University Press, New York, 2003.

[98] K. Yoshikawa and Y. Matsuzawa. *Physica D*, 84:220, 1995.

[99] K. Yoshikawa and Y. Matsuzawa. *J. Am. Chem. Soc*, 118:929, 1996.

[100] V. A. Bloomfield. *Curr. Opinion Struct. Biol.*, 6:334, 1996.

[101] V. A. Bloomfield. *Biopolymers*, 44:269, 1998.

[102] M. Takahashi, K. Yoshikawa, V. V. Vasilevskaya, and A. R. Khokhlov. *J. Phys. Chem. B*, 101:9396, 1997.

[103] K. Yoshikawa, S. Kidoaki, M. Takahashi, V. V. Vasilevskaya, and A. R. Khokhlov. *Ber. Bunsenges Phys. Chem.*, 100:876, 1996.

[104] U. K. Laemmli. *Proc. Natl. Acad. Sci USA*, 72:4288, 1975.

[105] M. Garcia-Ramírez and J. Subirana. *Biopolymers*, 34:285, 1994.

[106] R. W. Wilson and V. A. Bloomfield. *Biochemistry*, 18:2192, 1979.

[107] L. S. Lerman. *Proc. Natl. Acad. Sci USA*, 68:1886, 1971.

[108] E. Raspaud, M. Olvera de la Cruz, J. L. Sikorav, and F. Livolant. *Biophys. J.*, 74:381, 1998.

[109] N. Makita and K. Yoshikawa. *Biophys. Chem.*, 99:43, 2002.

[110] J. Widom and R. L. Baldwin. *Biopolymers*, 22:1595, 1983.

[111] C. B. Post and B. H. Zimm. *Biopolymers*, 21:2123, 1982.

[112] K. Yoshikawa. *Adv. Drug. Deliv. Rev.*, 52:235, 2001.

[113] L. R. Brewer, M. Corzett, and R. Balhorn. *Science*, 286:120, 1999.

[114] B. Ladoux, J. P. Quivy, P. Doyle, O. du Roure, G. Almouzni, and J. L. Viovy. *Proc. Natl. Acad. Sci USA*, 97:14251, 2000.

[115] R. Golan, L. Pietrasanta, W. Hsieh, and H. G. Hansma. *Biochemistry*, 38:14069, 1999.

[116] N. V. Hud and K. H. Downing. *Proc. Natl. Acad. Sci USA*, 98:14925, 2001.

[117] V. Vijayanathan, T. Thomas, A. Shirahata, and T. J. Thomas. *Biochemistry*, 40:13644, 2001.

[118] L. D. Murphy and S. B. Zimmerman. *Biophy. Chem.*, 57:71, 1995.

[119] M. Murayama and K. Yoshikawa. *J. Phys. Chem. B*, 103:10517, 1999.

[120] K. Yoshikawa and Y. Matsuzawa. *J. Am. Chem. Soc*, 118:929, 1996.

[121] T. Sakaue and K. Yoshikawa. *J. Chem. Phys.*, 117:6323–6330, 2002.

[122] B. Ostrovsky and Y. Bar-Yam. *Biophysical Journal*, 68:1694, 1995.

[123] F. Ganazzoli, R. La Ferla, and G. Allegra. *Macromolecules*, 28:5285, 1995.

[124] B. Schnurr, F. C. MacKintosh, and D. R. M. Williams. *Europh. Lett.*, 51:279, 2000.

[125] N. Kikuchi, A. Gent, and J. M. Yeomans. *Eur. phys. J. E*, 9:63, 2002.

[126] D. Porschke. *Biochemistry*, 23:4891, 1984.

[127] T. Odijk. *Macromolecules*, 28:7016, 1995.

[128] I. M. Lifshitz, A. Y. Grosberg, and A. R. Khokhlov. *Rev. Mod. Phys.*, 50:683, 1978.

[129] C. B. Post and B. H. Zimm. *Biopolymers*, 18:1487, 1979.

[130] G. S. Manning. *Quart. Rev. Biophys.*, 11:179, 1978.

[131] F. Oosawa. *Biopolymers*, 6:1663, 1968.

[132] F. Oosawa. *Phys. Rev. A*, 44:5272, 1991.

[133] H. R. Drew and R. E. Dickerson. *J. Mol. Biol.*, 151:535, 1981.

[134] B. G. Feuerstein, N. Pattabiraman, and L. J. Marton. *Proc. Natl. Acad. Sci. USA*, 83:5948, 1986.

[135] B. G. Feuerstein, N. Pattabiraman, and L. J. Marton. *Nucleic Acids Res.*, 18:1271, 1990.

[136] R. Marquet, C. Houssier, and E. Fredericq. *Biochim. Biophys. Acta*, 825:365, 1985.

[137] R. Marquet, A. Wyart, and C. Houssier. *Biochim. Biophys. Acta*, 909:165, 1987.

[138] R. Marquet and C. Houssier. *J. Biomol. Struct. Dynam.*, 6:235, 1988.

[139] C. G. Baumann, S. B. Smith, V. A. Bloomfield, and C. Bustamante. *Proc. Natl. Acad. Sci. USA*, 94:6185, 1997.

[140] I. Rouzina and V. A. Bloomfield. *Biophys. J.*, 74:3152, 1998.

[141] I. Tobias, B. D. Coleman, and W. K. Olsen. *J. Chem. Phys.*, 101:10990, 1994.

[142] B. D. Coleman and W. K. Olsen. *J. Chem. Phys.*, 118:7127, 2003.

[143] C. G. Baumann, V. A. Bloomfield, S. B. Smith, C. Bustamante, M. D. Wang, and S. M. Block. *Biophys. J.*, 78:1965–1978, 2000.

[144] A. Montesi, M. Pasquali, and F. C. MacKintosh. *Phys. Rev. E*, 69, 2004. article 021916.

[145] N. Yoshinaga, T. Akitaya, and K. Yoshikawa. *Biochem. Biophys. Res. Comm.*, 286:264–267, 2001.

[146] Y. Murayama and M. Sano. Exchange of counterions in DNA condensation. Preprint, http://daisy.phys.s.u-tokyo.ac.jp/mura_fluo_preprint0415.pdf.

[147] J. Rudnick and R. Bruinsma. *Biophys. J.*, 76:1725–1733, 1999.

[148] J. F. Marko and E. D. Siggia. *Biophys. J.*, 73:2173–2178, 1997.

[149] D. Matulis, I. Rouzina, and V. A. Bloomfield. *J. Mol. Biol.*, 296:1053–1063, 2000.

[150] Y. Murayama and M. Sano. *J. Phys. Soc. Jpn.*, 70:345–348, 2001.

[151] H. Wada, Y. Murayama, and M. Sano. *Phys. Rev. E*, 66. 061912.

[152] A. Halperin and E. B. Zhulina. *Europh. Lett.*, 15:417, 1991.

[153] A. Buguin and F. Brochard-Wyart. *Macromolecules*, 29:4937–4943, 1996.

[154] E. Fallman and O. Axner. *Appl. Opt.*, 42:3915, 2003.

[155] G.V. Vdovin. *Adaptive Mirror Micromachined in Silicon, Thesis.* Technische Universiteit Delft, 1996.

[156] A. Rohrbach and E.H.K. Stelzer. *Appl. Opt.*, 41:2494, 2002.

[157] P.C. Ke and M. Gu. *J. Mod. Opt.*, 45:2159, 1998.

[158] K.-B. Im, H.-I. Kim, I.-J. Joo, C.-H. Oh, S.-H. Song, P.-S. Kim, and B.-C. Park. *Opt. Commun.*, 226:25, 2003.

[159] A.V. Kachynski, A.N. Kuzmin, H.E. Pudavar, D.S. Kaputa, A.N. Cartwright, and P.N. Prasad.

[160] T. Ota, T. Sugiura, S. Kawata, M.J. Booth, M.A.A. Neil, R. Juskaitis, and T. Wilson. *Jpn. J. Applied Phys. Part 2-Lett.*, 42, 2003.

[161] G. Sinclair, P. Jordan, J. Leach, M.J. Padgett, and J. Cooper. *J. Mod. Opt.*, 51:409, 2004.

[162] Y. Liu, G.J. Sonek, M.W. Berns, K. Konig, and B.J. Tromberg. *Opt. Lett.*, 20:2246, 1995.

[163] E.-L. Florin, J.K.H. Horber, and E.H.K. Stelzer. *Appl. Phys. Lett*, 69:446, 1996.

[164] A.N. Kuzmin, A.V.Kachynski, T.Y. Ohulchanskyy, I. Roy, P.N. Prasad, and S. Bruckenstein. *Appl. Phys. Lett.*, 84:2454–2456, 2004.

[165] P.E.Hanninen, E. Soini, and S.W. Hell. *J. Microsc.*, 176:222, 1994.

[166] D. Malacara. *Optical Shop Testing*. Wiley, 1992.

[167] A.W.S. Ross, S.C. Graham, A.M. Gundlach, J.T.M. Stevenson, W.J. Hossack, D.G. Vass, G.K. Bodammer, E. Smith, and K. Ward. *Proc. SPIE Int. Soc. Opt. Eng.*, 4075:41, 2000.

[168] E. Theofanidou, W.J. Hossack, and J. Arlt. *Photon 02*, 2002.

[169] L. Zhu, P.-C. Sun, D.-U. Bartsch, W. Freeman, and Y. Fainman. *Appl. Opt.*, 38:6019, 1999.

[170] T. Ota, S. Kawata, T. Sugiura, M.J. Booth, M.A.A. Neil, R. Juskaitis, and T. Wilson. *Opt. Lett.*, 28:465, 2003.

[171] O. Albert, L. Sherman, G. Mourou, T.B. Norris, and G. Vdovin. *Appl. Opt.*, 25:52, 2000.

[172] K. Dholakia, G. Spalding, and M. MacDonald. *Physics World*, pages 15–10, 2002.

[173] W.M. Lee, X.C. Yuan, and D.Y. Tang. *Opt. Express*, 11:199, 2003.

[174] P.G. Rodrigo, R.L. Eriksen, V.R. Daria, and J. Glueckstad. *Opt. Express*, 11:208, 2003.

[175] H. Dammann and K. Cortler. *Opt. Commun.*, 3:312, 1971.

[176] M.P. Dames, R.J. Dowling, P. McKee, and D. Wood. *Appl. Opt.*, 30:2685, 1991.

[177] N.R. Heckenburg, R. McDuff, C.P. Smith, H. Rubinsztein-Dunlop, and M.J. Wegener. *Opt. Quantum Electron.*, 24:S951, 1992.

[178] C.D' Helon, E.W. Dearden, H. Rubinsztein-Dunlop, and N.R. Heckenburg. *J. Mod. Opt*, 41:595, 1994.

[179] E.R. Dufresne and D.G. Grier. *Rev. Sci. Inst.*, 69:1974, 1998.

[180] E.R. Dufresne, G.C. Spalding, M.T. Dearing, S.A. Sheets, and D.G. Grier. *Rev. Sci. Inst.*, 72:1810–1816, 2001.

[181] K.M. Johnson, M.A. Handschy, and L.A. Pagano-Stauffer. *Opt. Eng.*, 16:385, 1987.

[182] *CRL Opto Ltd, Http://www.crlopto.com.*

[183] R.L. Eriksen, V.R. Daria, P.J. Rodrigo, and J. Gluckstad. *Microelectron. Eng.*, 67-68:872–878, 2003.

[184] J.E. Curtis, B.A. Kes, and D.G. Grier. *Opt. Commun.*, 207:169, 2002.